# QUANTIFYING THE EFFECT OF WIND-DRIFT ON RADAR-DERIVED SURFACE RAINFALL ESTIMATIONS

---

A Thesis Presented to the Faculty of the Graduate School
University of Missouri-Columbia

---

In Partial Fulfillment for the Degree
Master of Science

---

by

STEVEN A. LACK

Dr. Neil I. Fox, Thesis Supervisor

MAY 2004

COMMITTEE IN CHARGE OF CANDIDACY

Assistant Professor Neil I. Fox
Chairperson and Advisor

Assistant Professor Patrick S. Market

Associate Professor Christopher K. Wikle

Adjunct Professor Emeritus Ronald E. Rinehart

# Acknowledgements

I will begin by thanking my advisor, Dr. Neil Fox, for allowing me the opportunity to come to the University of Missouri-Columbia and study a subject that has interested me since my undergraduate days at The Pennsylvania State University. I am thankful for the freedom he granted me as I continuously worked on my research. I would also like to thank the rest of the faculty in the Atmospheric Science Program, including Dr. Anthony Lupo, Dr. Patrick Market, and Dr. Adnan Akyüz, for providing a great environment to thrive academically and interesting opportunities outside the realm of my current research.

I am greatly appreciative to my parents for allowing me to pursuit the field of my choice and for supporting me as a poor graduate student. I would also like to thank my only sister, Nicole, for listening when I needed to vent. Special thanks also go to the rest of my family and friends, especially my fellow grad students, for all the encouragement and support I could ever hope for.

Last, but by no means least, I would like to thank Lindsay for her understanding and patience. She was instrumental in keeping me motivated until the end and always provided necessary distractions. I feel like I can handle any and all future challenges with her in my life.

# Table of Contents

# List of Figures

# List of Tables

# Chapter 1 Introduction

The national 30-year average for flash flood deaths in the United States is 127 as cited by the National Weather Service's Turn Around Don't Drown (TADD) initiative. This is nearly double the fatalities due to lightning (73) and tornadoes (65) (NWS, 2004). The primary motive for forecasting significant severe weather, including flooding, is to protect life, property, and finances. From the 1993 Mississippi River Basin flood the property damages were estimated around $20 billion (USGS, 2000). To put this in an international perspective, if London experienced a 50 year flood, 9500 properties would be at risk at a cost of nearly £17 million (Haggett, 1988). The properties and cost would be much higher today than these figures quoted more than 15 years ago. Furthermore, 5% of the population of Earth resides along the flood basin of the Yangtze River in China (Handmer, 1987), and 85% of the Japanese population live in areas prone to severe flooding (Oya and Haruyama, 1987). Although some of these statistics need to be updated to present day, they illustrate how the world is prone to damage caused by flooding of any extent.

In 1984, Reed outlined the benefits of flood warnings, which have been cited in many publications since. These benefits are categorized in three main ways:

a) evacuation of
   -people and livestock,
   -crops (by premature harvesting),

-sensitive and/or easily moved items (for example, cars, electrical equipment and furnishings);

b) amelioration though
   -temporary flood proofing (for example, sand bags and blankets),
   -opportune maintenance (clearing obstructions, culverts, etc.),
   -early alerting of emergence services,
   -orderly disruption of communications (road diversions);

c) control by
   -adjusting reservoir discharges to permit flood attenuation,
   -emptying storm tanks and balancing ponds prior to the arrival of floods.

There are several considerations when issuing hydrological forecasts, including: temporal and spatial dimensions of the area of concern and the available data sources to incorporate into the product. Qualitative estimations of precipitation will increase the lead time in flood forecasting, but with today's needs and technology more accurate quantitative estimates of precipitation leading to greater accuracy in streamflow are desired and necessary. With more accurate observations input into increasingly sophisticated hydrological models, lead time for issuing flood statements can result in the timely benefits outlined by Reed (1984).

In order to appropriately display hydrological parameters in a given model, observations must have a high degree of accuracy. Precipitation storm totals should have observational errors no larger than 10-20% (Collier, 1985). This accuracy may be difficult to achieve using radar data alone; however, with the advances in hydrological models and assimilation techniques this may no longer be a deterrent (Collier, 1996). While rain gauge networks may estimate the total depth of precipitation with some accuracy and temporal consistency, there could be major errors with streamflow estimations if the spatial pattern of precipitation is not properly represented (Collier, 1996).

When radar data were first incorporated into hydrological models, there was a wide range of responses from better to very slight or no improvement over rain gauge networks. Negative responses come from the inherent error in radar-derived rainfall estimations. Inaccuracies in radar data used to estimate rainfall totals within a hydrological model lead to substantially larger errors when looking at the parameters generated. The outlook for radar in hydrological applications is bright. With the advent of newer radar technologies, higher spatial and temporal coverage and accuracy in precipitation estimates result. There is a need for near-real time correction or adjustment of these data. Most common corrections come in the form of advances in technology to measure the power returned by the radar in a given volume aloft. However, spatial accuracy is essential in hydrological applications of weather radar, and it is this problem that needs to be addressed in more detail than has been since the development of radar for weather applications. Knowledge of the errors and their distribution in rainfall observations can improve the use of data in hydrological models. For example, one can perform a realistic stochastic ensemble forecast.

A common assumption when using radar retrieved precipitation observations in hydrological applications is that the precipitation observed aloft impacts the surface directly below the volume sampled by the radar. It is well known that rain may be advected laterally over considerable distances, implying that rainfall entered into distributed hydrological models will be inaccurate no matter how accurately it is measured aloft. In extreme cases, rain may be observed above one catchment and actually fall in another. As moves are made toward more accurate precipitation retrievals (using dual-polarization, for example) and higher resolution (for applications such as urban hydrology) this problem has received little attention. With the use of radar data assimilation into

numerical weather prediction (NWP) models, near-real time rainfall estimation corrections at the surface for hydrological applications are possible.

## 1.1 Objective

Improving the knowledge of errors of rainfall estimations and possible ways to correct these errors is necessary to improve the assimilation of radar into mesoscale NWP models and hydrometeorological prediction models. Both require an accurate spatial representation of rainfall. The objective of this research is to investigate the possible error due to the drift of precipitation by the wind. Two main schemes will be used. The first scheme is a bulk-advection scheme, in which the estimates of precipitation are based on an average droplet size for a given radar volume. The second scheme is a drop-sorting scheme, in which the estimates of precipitation are based upon 25 drop-size bins for a given radar volume.

With each scheme multiple assumptions can be applied throughout successive runs. One such option is incorporating the effect of topography in the wind-drift scheme. Another option includes hypothetically changing the constant altitude plan position indicator (CAPPI) height and the horizontal resolution of the native gridded data. Beam elevations can also be simulated within the program code. Vertical velocity derived from the retrieved horizontal components of the wind can be included or excluded for different runs. Each scheme with different combinations of assumptions will be tested and compared to examine the errors associated with the lateral movement of precipitation as it falls from aloft to the surface. This should result in an understanding of the

possible errors that would result if wind-drift was ignored on several spatial scales.

## 1.2 Statement of Thesis

When incorporating rainfall data into hydrological models there are many sources from which to take data, from rain gauge networks to spaceborne observations. Assimilating radar data (where available) into a hydrological model is a method with the opportunity for the highest temporal and spatial resolution. Previous work (*i.e.* Collier, 1999) has shown that spatial accuracy is of high importance in accurately portraying streamflow and other hydrological parameters. The research herein is an effort to examine the possible error inherent in radar-derived surface rainfall estimations at the surface due to the lateral movement of precipitation by the wind. It will be shown that the differences are significant when comparing raw uncorrected, or slightly corrected, reflectivity against the different wind-drift adjustment schemes while using different resolutions and varying assumptions within the structure of the schemes themselves. The differences should be greatest in magnitude for convective precipitation, but still significant for stratiform precipitation. The comparison of rainfall totals will not be correlated with rain gauge observations as this is just an exploration of the possible error introduced when incorporating the effect of wind-drift.

# Chapter 2 Background

The following subsections will address some of the common problems relating to the radar meteorology and possible solutions. It is necessary to cover some of the errors associated with using radar for estimates of precipitation as these errors will inherently affect the wind-drift adjustment schemes. A brief discussion of some future directions in estimating rainfall by advanced radars will also be presented. Some of the older research identifying the problem of the lateral advection of precipitation by the wind will be highlighted.

## 2.1 Errors in Radar Reflectivity Measurements

There are numerous sources of error involved when using radar for meteorological applications. Most involve the return from a target in a given radar volume, to which a correction is then applied aloft, but not carried to the surface directly. A summary of the possible errors in radar reflectivity aloft and some of the corrections will be discussed below.

A common problem in radar meteorology is correcting for beam attenuation, especially for radars operating at shorter wavelengths, including C-band radars, and millimeter wavelength cloud radars. Attenuation is simply the reduction in power caused when electromagnetic radiation passes though a

medium of any density. Attenuation can be caused by various atmospheric constituents, including: rain, snow, clouds, water vapor and oxygen (Rinehart, 1997). The overall result of attenuation causes the power returned by the radar to be reduced by some non-uniform amount. Attenuation caused by the atmosphere is normally quite small and generally ignored for most radar applications, but in applications where higher accuracy is desired atmospheric gas attenuation can be corrected by increasing reflectivities as a function of beam height and range from radar (Rinehart, 1997).

Cloud and precipitation attenuation is not as easily corrected for as attenuation due to oxygen because water content is highly variable within the troposphere. Correcting for attenuation during precipitation is a complex function of the drop-size distribution within the sampled volume. Attenuation from clouds is usually low, depending upon the type of cloud. For most precipitation radars, the attenuation due to clouds consisting mainly of ice is negligible. Snow generally has negligible attenuation effects due to the small dielectric constant for ice, which implies a weak interaction between microwave radiation and ice, and the fact that generally only low clouds produce snow (Rinehart, 1997). For radars with wavelengths less than 10 cm, especially those approaching X-band, attenuation due to warm clouds, cumulonimbus for example, can be quite intense. As raindrops are much larger than cloud droplets, the attenuation due to rain is much stronger than clouds alone. The effect of rain, especially heavy rain (>50 dBZ), can have a significant impact even on the larger wavelength radars such as the National Weather Service's (NWS) operational radar, the WSR-88D. The attenuation in heavy rain can cause significant underestimation of the intensity of rain in thunderstorms beyond the first line of storms.

Attenuation in downpours can also be due to radome wetting. As the dome covering the radar becomes coated with water, the power received is reduced leading to an underestimation of precipitation even from the nearest storm cells. An example of radome wetting occurred in the 26 September 2000 case as the line of storms moved directly over the Kurnell radar (Sleigh, 2002).

Correcting for attenuation is difficult in cases where the effect is not small enough to be neglected. In situations with clouds and rain, correcting for attenuation can be futile. Attenuation affects the maximum range at which the radar can detect a signal. Therefore, in cases of extreme attenuation the actual trailing edge of the precipitation may not appear at its true location and returns will appear weak where they might be quite strong. One way to accurately adjust for this is to use multiple radars observing the same phenomenon from different sites. Composite images may be useful in areas of significant radar coverage in reducing the effect of attenuation.

Another source of error, in severe cases, is contamination due to hail. Hail spikes result from non-Rayleigh scattering of large, wet hail by first, forward scattering of the strongly reflecting hail aloft to the surface, second, backscattering by the ground to the hail core, and third, backscattering to the radar (Zrnic, 1987). Hail spikes are useful in determining regions that are producing severe hail when monitoring for severe weather. However, when using reflectivity to estimate rainfall rate, hail contamination serves as a similar problem to that of attenuation. Given a strong return by radar (> 50 dBZ), it can no longer be assumed that the precipitation is non-frozen. In such cases, rainfall rates can be vastly overestimated in cases where hail is present without substantial observations or dual-polarization output.

The bright band is a problem that many have successfully applied corrections for in past situations. The bright band is a result of enhancement of

reflectivity resulting from frozen precipitation falling though a melting layer, thus yielding a higher reflectivity in this region aloft (Austin and Bemis, 1950). There are several factors that cause this bright band effect, including: an increase in the dielectric constant due to melting precipitation, larger particle sizes due to increased aggregation in the melting layer, increased backscatter due to the wetting of frozen precipitation (Austin and Bemis, 1950), nonsphericity of hydrometeors due to melting, and changes in density due to differences in water distributions in mixed precipitation (Fabry and Zawadzki, 1995). During occasions when the bright band is present in reflectivity fields aloft, overestimation of precipitation can be as high as a factor of 10 (Smith, 1986). The NWS has a brightband identification algorithm (BBID) applied to WSR-88D imagery, which simply identifies regions where brightband contamination may be present, but it does not correct for errors (Gourley and Calvert, 2003). By identifying regions of brightband contamination correction schemes can be applied yielding more accurate rainfall estimations as well as identifying rain-snow lines.

Some of the issues with radar come from miscellaneous effects such as beam blockage due to obstructions, clutter, anomalous propagation, and incomplete beam filling and overshooting. The first issue, beam blockage, is unavoidable in most situations, especially in areas of mountainous terrain. Nearby radars in the network are really the only hope of adjusting for this problem; if one radar is blocked hopefully another one is nearby to cover the missed area. Clutter, or clear air return, is another common problem; however, it is usually easily corrected for, or removed. False precipitation echoes lead to overestimations of rainfall in some cases (Rosenfeld *et al*., 1992). Similar patterns of "noise" normally appear on a day-to-day basis under a given radar umbrella. This can simply be filtered out as it remains fairly systematic. Clutter can be

quite useful; it is a good signal that the given radar is functioning properly (Rinehart, 1997). Anomalous propagation is a problem that results from the ducting of the radar beam due to a nocturnal inversion or shallow moist layer (sometimes after a line of intense convection) (Austin, 1987). This results in large returns from non-meteorological targets that are normally below the non-ducted lowest beam elevation, which in turn causes an overestimation of surface precipitation. Beam overshooting and filling are problems caused due to the radar beam's increase in elevation and volume at greater ranges. Overshooting causes underestimations in precipitation by missing shallow low level clouds, and is most commonly a wintertime phenomenon. Beam filling causes reflectivity to be spread into areas where there may not actually be precipitation. For instance, if a storm top just makes it into the edge of the highest beam elevation then the storm top is overestimated. This works the same way with the horizontal extent of storms, as it does in the vertical.

## 2.2 Estimating Rainfall Rates from Radar

Since the first use of radar into meteorology, estimating rainfall rates has been an ongoing research topic. Empirical relationships relating reflectivity ($Z$) to rainfall rates ($R$) (Z-R relationships) were the first to appear in literature, followed with today's more complex relationships resulting from the use of dual-polarized radars and advanced methods to measure drop-size distributions.

The building block to calculating rainfall rates using radar reflectivity is based on the most commonly used drop-size distribution (DSD) given by Marshall and Palmer (1948). Raindrop-sizes were collected in experiments using dyed filter paper to give a distribution of drops with size. The general relation

found though experimentation is given by (2.2.1), where $D$ is the drop diameter, $N_D$ is the number of drops of diameter between D and $D+dD$ in a unit volume of space, and $N_0$ is the value of $N_D$ at $D=0$.

$$N_D = N_0 e^{-\Lambda D} \tag{2.2.1}$$

It was found that for any rainfall rate $N_0 = 0.08\ cm^{-4}$ and $? = 41\ R^{-0.21}\ cm^{-1}$, where R is the rainfall rate in mm $h^{-1}$. Marshall and Palmer also related the mass of rain water ($M$) to both $Z$ and $R$ as well. It is noted the empirical equations above have flaws in that the drop electrical charge, disintegration, and coalescence could have some effects on rainfall rate.

The main difference between modern evaluations of drop-size distributions and the Marshall-Palmer methodology is the use of technology. The use of video disdrometers give a much better measure of DSD than the old style of catch and measure using blotter paper, as they allow much greater sampling. Determining Z-R relationships is dependent upon reflectivity, which is dependent on the DSD. DSDs depend on the rain formation process and vary geographically, making it important to accurately measure distributions over many points in a country as broad at the United States. The varying DSDs give the possibility for numerous Z-R relationships. The WSR-88D Operational Support Facility (OSF) has outlined five Z-R relationships to be used in different locations based on the type of rainfall event (Table 2.2.1). Each of the listed Z-R relationships is assumed due to the DSD of a certain rainfall event. However, it is important to note that DSDs vary with every storm, and using these relationships assumes the DSDs used based on the relationship given are in accord with real DSDs while ignoring radar error effects (*i.e.* attenuation). A recent case study dealing with flash floods in Texas further makes the claim that

| RELATIONSHIP | Optimum for: | Also recommended for: |
|---|---|---|
| **Marshall-Palmer ($Z=200R^{1.6}$)** | General stratiform precipitation | |
| **East-Cool Stratiform ($Z=130R^{2.0}$)** | Winter stratiform precipitation - east of continental divide | Orographic rain – East |
| **West-Cool Stratiform ($Z=75R^{2.0}$)** | Winter stratiform precipitation - west of continental divide | Orographic rain – West |
| **WSR-88D Convective ($Z=300R^{1.4}$)** | Summer deep convection | Other non-tropical convection |
| **Rosenfeld Tropical ($Z=250R^{1.2}$)** | Tropical convective systems | |

**Table 2.2.1:** The five Z-R relationships used to estimate rainfall rates in the U.S., from the NWFO WSR-88D Operations Memorandum, 1999.

the Z-R relationship for tropical systems should be applied in areas experiencing heavy rainfall. The conclusion was that the tropical Z-R relationship was more accurate than using the Z-R relationship for deep convection (Vieux and Bedient, 1998).

The trend for researching estimates of rainfall rate is advancing with the use of polarimetric radars. One of the advantages to using polarimetric radars, as opposed to the standard NEXRAD network, is to reduce the effect the theoretical DSD plays in estimating rainfall rate. This is accomplished by accounting for how the drop shape changes with increasing size using vertical and horizontal polarization of radiation. This allows for an explicit observation of the DSD. The major advantage includes fine tuning rainfall rates by generating multivariable relationships using the different measurements given by polarimetric radars. In this case, no individual variable becomes the sole factor in an equation to estimate rainfall. More recent research includes the return of the use of X-band (~3 cm) and now some $K_a$-band (~0.80 cm) radars.

To further understand how the use of polarimetric radars can give a better estimate of rainfall rates, the parameters of polarimetric radars have to be defined, specifically those used in estimating rainfall rates. Early studies of estimating rainfall were done by examining the specific differential propagation phase shift ($K_{DP}$). $K_{DP}$ is the range derivative of the propagation differential phase shift ($f_{DP}$), which is a component of the total differential phase shift ($y$). $y$ has two components: the backscatter differential phase shift ($d$), which is the phase shift resulting from just the backscatter properties of the scatterer, and $f_{DP}$, which is the shift due to precipitation in the two beams. $d$ is normally filtered out so the focus is on precipitation and the resulting $f_{DP}$ (Hubbert *et al.* 1993). If there is a perfectly isotropic scatterer, there will be no shift because the horizontal and vertical components are identical, however, in precipitation, oblate raindrops have a greater horizontal dimension than vertical as they fall, and result in a slightly positive shift (Hubbert *et al.* 1993). $K_{DP}$ allows for the discrimination between isotropic (hailstones) and anisotropic (raindrops), for hailstones $K_{DP}$ is close to 0 ° $km^{-1}$ and for rain $K_{DP}$ is greater than 0.5 ° $km^{-1}$. $K_{DP}$ is almost linearly proportional to the precipitation liquid water content and can therefore be used to estimate rainfall rates. The differential reflectivity ($Z_{DR}$) and the horizontal polarization reflectivity ($Z_{eh}$) can be used in addition to $K_{DP}$ to yield more accurate rainfall rate estimations.

The main reason for using a shorter wavelength is to get accurate rainfall estimations for light stratiform precipitation ($R < 15$ mm $h^{-1}$), which makes up a significant fraction of total rain accumulation, even in the tropics (Matrosov *et al.* 1999). Using $K_{DP}$ as a function of rainfall rate is less sensitive than using reflectivity, and at shorter wavelength bands actually yields a measurable phase shift in light rain, as opposed to operational S-band radars measuring phase shifts (Matrosov *et al.* 1999). Two major problems exist when dealing with

estimations of rainfall rate using phase shifts. First, the $K_{DP}$-R relationships are sensitive to the assumed drop aspect ratio model used, and therefore, change depending on what model is used. However, differential phase shift methods are less sensitive than reflectivity to variations of DSD, making relationships between differential phase and rainfall rates more accurate than solely using Z-R relationships (Matrosov *et al.* 1999). The other problem comes in the term for the backscatter phase shift $d$. In $K_a$ band radars, $d$ becomes the dominant term and makes estimates of rainfall rate in the S-band far less accurate than X-band radars (Matrosov *et al.* 1999).

$K_{DP}$-R relationships depend more on the shape of drops rather than the DSD. More complex formulations of estimates of rainfall use a multivariable approach using $K_{DP}$, $Z_{DR}$, and $Z_{eh}$. (Matrosov *et al.*, 2002). Since the terminal velocities and shapes of water drops are dependent on the density of air, it might be useful to tune $Z_{DR}$-R relations to account for density of air (stations at different elevations) and use that result to correct for relations using differential phase shift measurement (Matrosov *et al.* 1999). The resulting equation accounts for the drop shape and size dependence and the changes in velocities based on the density of air. It also corrects for the attenuation of power (using differential phase shift) in more intense rainfall rates due to the use of reflectivity measurements from the X-band radar, which has large attenuation as rainfall intensity increases (Matrosov *et al.* 2002).

Since reflectivity measurements are involved in the new three-term method for estimating rainfall, experimental DSDs were used from a study off the Virginia coast to come up with the shape-size estimate. It is assumed that the new rainfall estimation relation using three terms can be applied to many geographical locations where typical rainstorms are in the reflectivity range of 30-50 dBZ (Matrosov *et al.* 2002). These corrections allow X-band polarimetric

radars to estimate rainfall in very light rainfall to intense rainfall; whereas, the previous study was used as estimations for light to moderate stratiform events only. The resulting three-term rainfall estimation equation is approximated by: $R \approx c(h)\ 1.06\ Z_{eh}^{0.3}\ K_{DP}^{0.50}\ Z_{dr}^{-0.84}$ (where $c(h)$ is the altitude correction coefficient based on density, $Z_{eh}$ ($mm^6\ m^{-3}$), $K_{DP}$ (° $km^{-1}$), and $Z_{dr}$ is in linear units as opposed to $Z_{DR}$ which is in decibels) (Matrosov *et al.* 2002). This approximation for X-band radars was derived from the one suggested by Gorgucci *et al.* (2000) for C-band radars. Using the three polarimetric terms acts as a way to tune each term and also gives the better result for rainfall estimates than any one parameter used alone.

It is important to point out that the relationships discussed used research instruments and none of these methods are used in operational meteorology yet. Polarimetric radars are more complicated than horizontal S-band Doppler radars used in the NEXRAD network and other (media and national network) C-band radars. The best possible estimates using the technology discussed still have errors in the 20-40% range, which is still not as good as what is needed for hydrological applications, according to Collier (1985). Polarimetric radars are an improvement compared to NEXRAD estimates of rainfall. Moving to the use of multivariable equations to estimate rainfall rate is the future. Using different variables decreases the effect each term has on the rainfall rate, therefore, it seems that the biases of the components (*i.e.* DSD) that go into each variable will be decreased.

Even with the advanced technology, using empirical relationships to relate reflectivity to rainfall rates can be misleading. It is well known that drop-size distributions vary throughout a given storm, making it impossible to justify the use of one relationship for the duration of an event. For example, a squall line would be assumed to have a convective relationship; however, the trailing

edge of the storm would have stratiform characteristics. It is therefore necessary to be knowledgeable of the situation at hand to determine where the radar is in fact overestimating and/or underestimating precipitation aloft. Estimating rainfall rates aloft is one source of error, this error becomes larger when taking measurements aloft and applying them to the surface below for other hydrometeorological applications without additional corrections, which is the focus of this thesis.

## 2.3 Spatial Errors for Surface Rainfall Estimations

Most of the radar errors along with their various methods of correction occur aloft and ignore how the rainfall observed aloft reaches the surface, although precipitation estimates from radar are generally extrapolated from aloft vertically downward to the ground beneath, using a Z-R or similar relationship. Although dual-polarization and other advanced techniques are used to achieve higher accuracy in estimating rainfall rates from reflectivity, these methods do not correct for the spatial inaccuracy at the surface as is required for hydrological application. Therefore, it is necessary to examine the errors that result as the precipitation falls from a given radar volume aloft to the surface.

Wind-drift has been recognized as an issue since early in the days of attempts to use radar reflectivity in estimating rainfall totals at the surface, but this has been largely ignored in today's applications of weather radar. Wind-drift has been identified as a problem, but it is never addressed as something that leads to large errors in estimating surface rainfall fields or as an error that could be corrected. In hydrological applications of weather radar, incorporating surface rainfall fields accurately, not only the intensity but also spatial accuracy,

is of key importance. Ignoring the effects of wind-drift on falling precipitation could cause errors in predicted streamflow, and other variables important to hydrological studies.

The first reference to the problem of wind-drift is found in Gunn and Marshall (1955). They identify the parabolic trajectory of raindrops in a constant wind shear environment, and allude to the possibility that the distances along the ground could be quite large from the original location of the droplet. A study examining drop-size history in a shower by Atlas and Plank (1953) reveals that if two droplets of different size reach the same point on the ground they must have come from different points in space. This is an early reference to drop-sorting, where the smallest drops are located at the edge of the storm cell while the larger drops tend to appear at the center of the echo. A more modern reference to the problem of wind-drift as it applies to urban hydrology is found in Collier (1999); however, like earlier studies in wind-drift, no real quantification of the possible error is accomplished. Wind-drift is secondary to advanced methods in estimating variables inside the radar volume scan aloft. Even with dual-polarization and other techniques for accurately assessing drop shapes and drop-size distribution in the target radar volume aloft, this will not enhance the spatial accuracy or surface rainfall fields without examining wind-drift.

## 2.4 Summary of Errors

A summary of errors, their estimated magnitude, and how well each is understood, borrowed from Fabry (2004), is displayed (Table 2.4.1). Systematic errors with radar equipment are listed first; most of these are not a major issue. Most of the errors listed within the table are understood fairly well and some

even have a good deal of knowledge associated after a correction has been applied. This table serves as a good summary of the problems outlined in the previous sections. The focus of the research within this thesis deals with precipitation drift, which is listed in the poor category for both the knowledge of the magnitude estimation and the error after correction. In particular, this research deals with the drift of rain, as snow has a lesser effect on hydrological variables for a given watershed. With some subwatersheds on the order of 10 $km^2$, even a 5-20% error due to precipitation drift could be significant when attempting to model streamflow, especially in urban basins.

| Nature of Error | Magnitude Estimate | Magnitude After Correction | Comments | Knowledge of magnitude estimate | Knowledge of error after correction |
|---|---|---|---|---|---|
| Variability in transmitter power | ? (small until failure?) | Small if correction is regularly updated | Estimated by power measurement | Good to poor (system specific) | If it exits, knowledge is not well disseminated |
| Poorly known characteristics of components (antenna, filters) | ~15% | Small? | Corrected by solar calibration and external methods (clutter strength, gauges) | Poor per se, but extremely slow time evolution helps | Not a major issue? |
| Receiver miscalibration, non-linearity | 15-20% (time varying bias) | Small if correction is often updated | Correction by solar calibration, clutter strength methods, gauge adjustments | Approximate | Not a major issue? |
| Wet radome attenuation | Can be large (>50% at C-band) | ? | Extremely difficult correction by clutter strength because azimuthal dependence | Poor | Poor |
| Beam blockage | Site specific biases | Small in flat terrain if done well | Good site survey needed; problematic in mountains | Very good to poor (site specific) | Good to poor, OK in flat terrain |
| Path attenuation (gas) | 20% bias {5% bias} | Small if done well | Well understood but generally not properly corrected for (~25% of error is left on average) | Very good | Correction dependent |
| Path attenuation (precipitation) | Possibly huge bias | Possibly huge | Extremely difficult correction (many variations) | Fair (S-band) to very poor (X); site specific | Good to very poor; major error source |
| Ground target contamination | Variable, site specific | Tolerably small if done well | Corrected by Doppler and/or texture methods | Good | Fair to poor |
| Echo fluctuations | <1% noise {5% noise} | <1% {2%} | Reduced by taking storm advection into account | Very good | Good |
| Converting Z aloft to R aloft | 30% noise {50%} | 5%? {10%?} | Correction requires gauge/DSD info | Fair, site and event specific | Poor |
| Vertical profile correction | 0-140% {0-50%} bias | 25% {10%?} | Strong dependence on 0°C level; many elevations required | Good to fair | Fair to poor; major error source |
| Precipitation drift | <5% noise in rain {5-50%} | <2% {5-20%} | Largest for snow and tiny basins; event specific | Fair to poor | Poor |
| Simplistic calculation of accumulation | 1-4% noise {25-100%}, event specific | <1% {5-25%} | Reduced by taking storm advection and evolution into account | Fair | Fair |

**Table 2.4.1:** The complete enumeration of radar errors (abridged). Error estimates are for hly accumulations over a 100 km$^2$ area at 120 km, with errors for 5-min accumulations over 1 km$^2$ at 30 km in curly brackets (taken from Fabry, 2004).

# Chapter 3 Methodology

## 3.1 Data Sets

The data for the research presented was taken from the Sydney 2000 World Weather Research Programme's (WWRP) Forecast Demonstration Project (FDP) (Keenan *et al.*, 2003). The project was held during the 2000 Olympic Games and focused on urban nowcasting and short-term boundary layer prediction (Keenan *et al.*, 2003). The goal was to test and evaluate different nowcasting systems, 0-6 h forecasts, from the United States, United Kingdom, Canada, and Australia. Because of the importance of the event, the Australian Bureau of Meteorology's (BOM) observing network was enhanced significantly. Three radars and 15 additional automated stations were in place within the venue area (Keenan *et al.*, 2003).

The data for this research project involve both wind velocity information and reflectivity. The velocity and reflectivity information were obtained from observations using the CPOL radar that was at Badgerys Creek from July 2000, approximately 40 km west of Sydney (Fig. 3.1.1) (Keenan *et al.*, 2003). The native grid of reflectivity is a CAPPI height set at 1.5 km above radar height. The horizontal radial velocity data from the CPOL were input into an adjoint model similar to that described by Sun and Crook (1994) to produce two-dimensional wind fields for display on a Cartesian grid. The vertical velocity data were

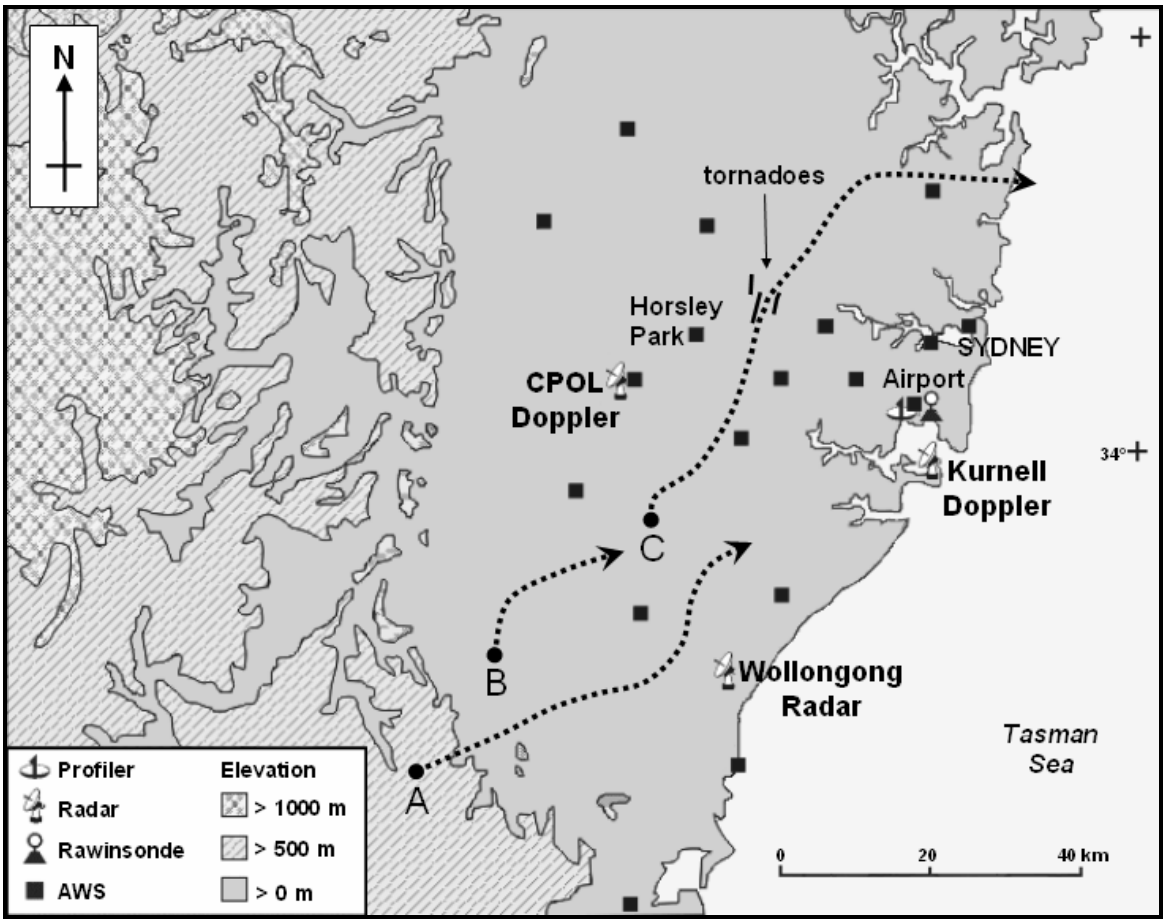


**Figure 3.1.1:** Map of Sydney and region showing locations of instrumentation as well as tornado damage tracks and the paths of Storms A, B, and C on 3 November 2000. The locations of the 18 automatic weather stations (AWSs) that were part of the FDP mesonet are shown.

derived from the adjoint model wind field by integrating the continuity equation (Sleigh, 2002). All the velocity data are also from the 1.5 km CAPPI height level for consistency. Additional information used includes a high resolution topographical map of the area of interest smoothed to the native resolution of the reflectivity and velocity fields.

The cases used in this research include a stratiform case and two convective cases. The stratiform case was a widespread light rain case from 18 November 2000. The convective cases include a severe case from 3 November

2000, in which three tornadoes were reported, and a case which produced a bow echo from 26 September 2000. For the November cases, a 180-min time frame was selected in 10-min increments yielding 17 time steps. For the September case, a 160-min time frame was selected using the same time increment yielding 15 time steps. The cases will be discussed in more detail in the results section (Chapter 4).

## 3.2 Wind Retrieval

The Doppler winds were retrieved by the CPOL and input into an adjoint model to yield a Cartesian grid of u- (east-west) and v- (north-south) component velocities. From the u- and v-components, the w component was derived from integrating the continuity equation and making comparisons with the given CPOL reflectivity (Sleigh, 2002). The following subsections will give some background on adjoint models and the derivation of vertical velocity.

### 3.2.1 Adjoint Model Background

The horizontal wind fields were derived in gridded format by assimilating Doppler radar data from CPOL into an adjoint model similar to that described by Sun and Crook (1994). This section will briefly describe how an adjoint model functions and the output that was generated for the research presented.

Adjoint equations describe the evolution of the sensitivity to initial, boundary, and parameter conditions backward in time (Courtier *et al.*, 1983). The adjoint functions for a model are the solution to a system of equations derived from the differential form of the model's system of equations. Adjoint

models attempt to minimize a cost function to identify regions where the model is most sensitive to perturbations by looking at the evolution of the perturbations themselves. This is achieved by calculating the sensitivity of the simulated state and comparing it to all previous synoptic states. Modeled data is fitted to actual observations, given by both surface and upper air observations, to yield a more accurate modeled field in a near-real time simulation. The background field for the Sydney 2000 project had the option of coming from the Australian Limited Area Prediction System (LAPS), the previous Variational Doppler Radar Analysis System (VDRAS) run, a forecast initialized from the previous VDRAS run, or performing an analysis using the mesoscale datasets available during Sydney 2000 (Crook and Sun, 2004). The latter was the most common method of choice.

The specific case of an adjoint model used in the research presented here involves wind and thermodynamic retrieval from a single Doppler radar described by Sun and Crook (1994). The purpose of the experiment was to find convergence lines near the surface to forecast thunderstorm initiation, which requires high resolution temperature and wind field information. Pressure and temperature deviations can be derived from the wind field given by both surface observations and Doppler radial wind fields. The adjoint model assimilates the radar data to yield a more complex wind field in the storm and near-storm environment, where surface and upper air observations may be sparse or unavailable. This results in a higher degree of spatial and temporal accuracy than standard surface observations fit to a gridded model alone. The surface and upper air observations are used to generate adjoint model wind fields at multiple levels from near the surface to the upper troposphere in some cases. This high spatial and temporal accuracy is needed to apply the wind-drift schemes; the

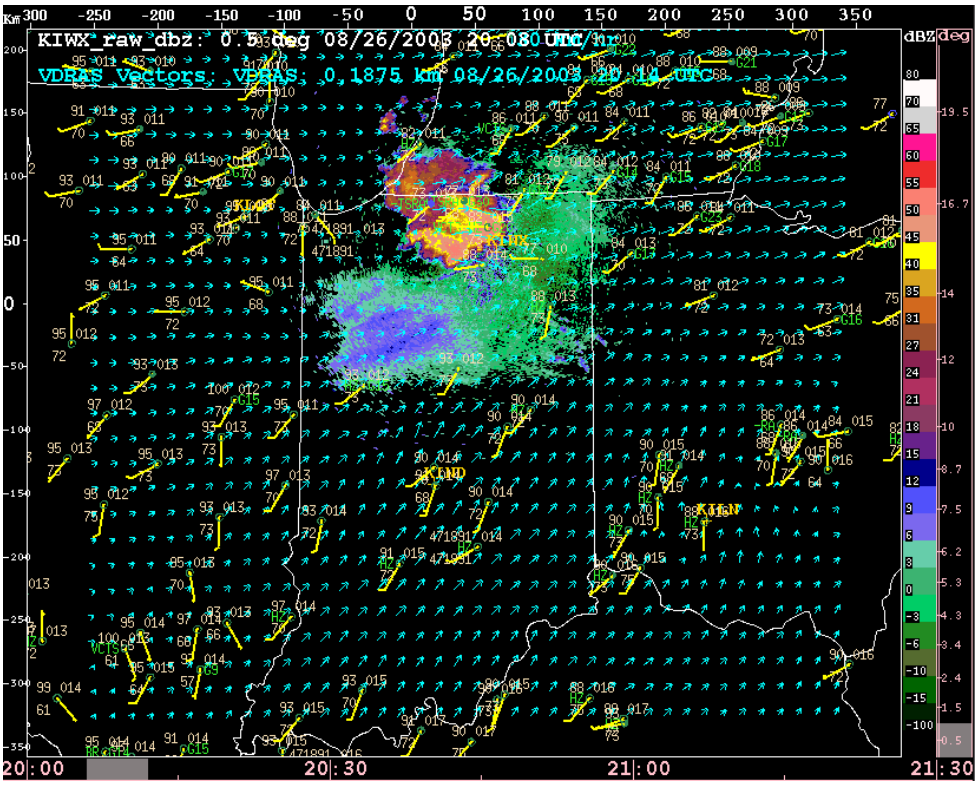


**Figure 3.2.1:** An example of the adjoint model wind field. The surface observations are the yellow wind barbs, and the adjoint wind field is represented by the grid of blue vectors. The image is overlaid with reflectivity from the KIWX radar.

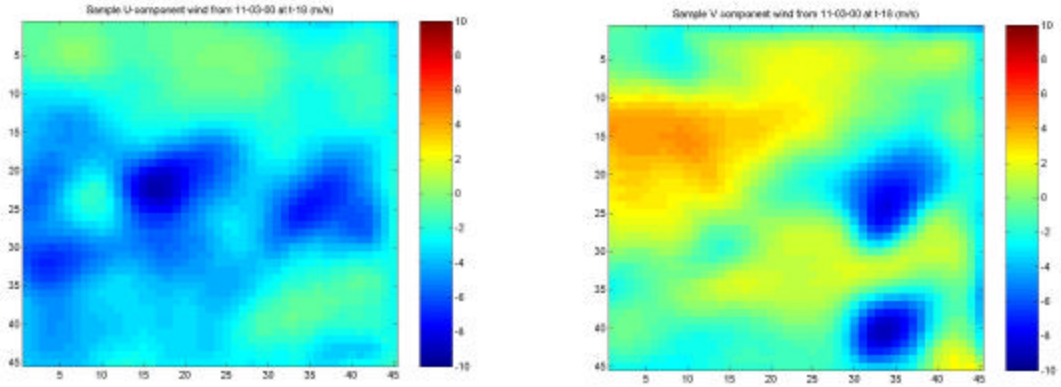

**Figure 3.2.2:** An example of the u field velocity (left) from and the v field velocity (right) 3 November 2000 at the last time step. The scale used is ±10 m $s^{-1}$.

schemes will be discussed further in later sections. An example of the output of the adjoint model is shown (Fig. 3.2.1). In this example, the surface wind observations are the yellow wind barbs and the adjoint model wind field is represented by the blue vectors. The reflectivity is also overlaid in the image to show the sensitivity of the adjoint model to the storm environment. The resultant adjoint wind field in the experiments used in this research is broken down into u- and v- component velocities (Fig. 3.2.2).

### 3.2.2 Vertical Velocity Derivation

The vertical velocities are important to this research as falling precipitation does not get advected only in the horizontal, but also in the vertical to an extent. Precipitation can either fall faster (slower) if there is downdraft (updraft) present in the given grid. The vertical fall velocity field is derived from the grids of horizontal velocities by integrating the continuity equation and then comparing the field of vertical velocity with the given field of reflectivity based on multiple CAPPI height levels (Sleigh, 2002). The continuity equation (3.2.1) states that mass must be conserved in a fluid.

$$\frac{\partial u}{\partial x}+\frac{\partial v}{\partial y}+\frac{\partial w}{\partial z}=-\frac{1}{r}\frac{dr}{dt} \tag{3.2.1}$$

If it is assumed that the atmosphere is an incompressible fluid, a good approximation over a horizontal plane, the right hand side of the equation is eliminated and a numerical approximation (3.2.2) given by Sleigh (2002) is left.

$$\frac{u_{x+1,y,z}-u_{x-1,y,z}}{2dx}+\frac{v_{x,y+1,z}-v_{x,y-1,z}}{2dy}+\frac{w_{x,y,z}-w_0}{\Delta z}=0 \tag{3.2.2}$$

This leaves only $w_{x,y,z}$ as the unknown, as $w_0$ is set to 0 (surface). Rearranging yields the equation (3.2.3) to solve for the vertical velocity.

$$w_{x,y,z} = \Delta z\left(\frac{\left(u_{x-1,y,z} - u_{x+1,y,z}\right)}{2dx} + \frac{\left(v_{x,y-1,z} - v_{x,y+1,z}\right)}{2dy}\right) \tag{3.2.3}$$

This equation assumes that density is constant, although in instances of convection barotropy does not hold. Sleigh points out this experiment has shown some promise in studying vertical velocity fields in convection (Lhermitte, 1970, for example). An example of the derived field of vertical velocity used in this research is shown (Fig. 3.2.3).

## 3.3 Program Structure Basics

The following sections will describe the two wind-drift schemes used and the assumptions and formulations built in the structure of the code. The first scheme is a simplified "bulk-advection" scheme (Appendix A) while the other is a more complex, and more physically realistic, "drop-sorting" scheme (Appendix B). The discussion of the two schemes will follow a brief discussion on MATLAB and the basic architecture of the code both schemes use.

MATLAB was designed to be a "Matrix Laboratory" originally; however, with the newer versions of MATLAB now available it has become a popular method for engineers and other scientific disciplines for programming in multiple dimensions (Etter and Kuncicky, 1999). Since MATLAB commands are written in a way that is similar to engineering and mathematical expressions it has become the programming package of choice since it is much faster at obtaining solutions than high-level languages such as C or FORTRAN (Etter and Kuncicky, 1999). MATLAB has been used in many applications in remote

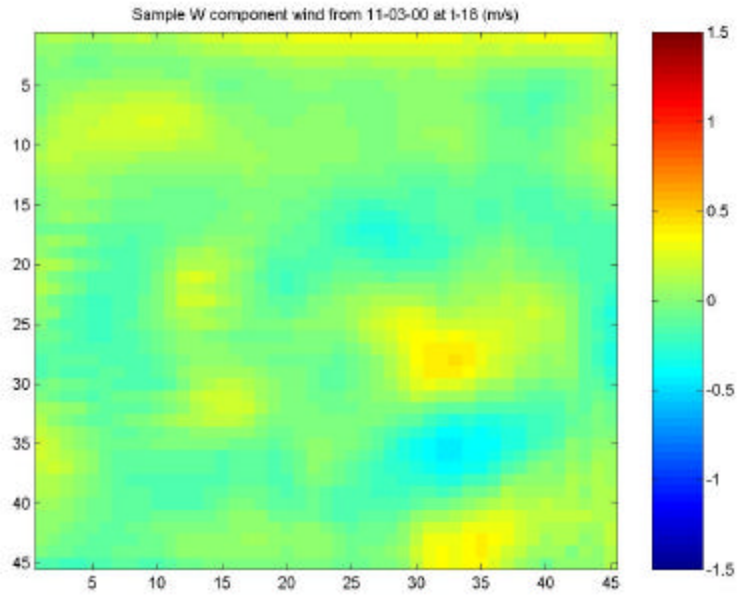


**Figure 3.3.1:** An example of the vertical velocity field used at the last time step from November 3rd, 2000. The scale used is ±1.5 m $s^{-1}$.

sensing, including radar and satellite, during its lifetime. Since the data being input into the schemes described below used gridded data, MATLAB is the ideal software of choice.

The real problem with adjusting for the theoretical advection of precipitation is to calculate the contribution from individual gridded data squares (pixels) to other nearby squares. This is accomplished by using a Cartesian grid of reflectivity and overlaying the u- and v-component of the wind, given by the adjoint model output, and applying some simplified expressions relating these variables. From the given data, calculations of droplet fall speed can be made within an individual grid square leading to the wind-drift in the x and y directions of the droplets. This results in a given pixel's contribution to another grid location. Finally, each square in a new grid is summed based on the contributions from the other nearby squares in the system yielding a new

distribution of reflectivity, or rainfall rate, at the surface. The correction scheme changes slightly when using the bulk-advection scheme or the drop-sorting scheme.

The individual grid square or size bin contribution to other grid squares is determined by simply multiplying the wind speed in the u and v directions by the fall time. Wind speed is determined by making an assumption on the shape of the wind profile from the surface to the elevation of the radar beam or CAPPI; in the following examples a constant shear profile is assumed such that drops follow a parabolic trajectory given by (3.3.1), where $x$ is the wind-drift in a given direction by the wind speed $a$ at height $z$ with a droplet fall speed of $V_d$ (Gunn and Marshall, 1955).

$$x = az^2 / 2V_d \tag{3.3.1}$$

Given the dimension of a single pixel, a critical range of influence can be determined by finding the magnitude of the combined u and v wind components. If the critical range is greater than the dimension of the individual square, the contribution to the original grid box is zero. This means that all of the precipitation from that square is being advected to a different location and, most likely, contributes to more than one other grid square within the given area.

Once the critical range is found for each grid square, it must be determined which original grid squares aloft contribute to each individual surface grid square. In most cases, multiple grid boxes will contribute to a single pixel, unless the wind is calm in a given column, making the critical range zero resulting in no wind-drift effect. Given the distance each area of precipitation travels in the x and y directions, the fraction of overlap onto other grid squares is calculated using simple geometry. These overlapping areas are represented as fractions of the original square's rain rate moved to a new grid square. All the

fractions over one grid square are summed yielding a new rain rate, or reflectivity. Once each grid square or size bin in the given grid is accounted for, the new field can be compared with the original field of rain rate, and the errors associated with wind-drift can be calculated for each case.

Some of the basic architecture within both schemes includes the process of reflectivity filtering to yield meaningful results and the relationships used to convert reflectivity to rainfall rate. The lowest reflectivity allowed to exist is 10 dBZ. This means some of the returns may be from non-precipitating clouds, but thinner clouds are generally thrown out of the field. The highest allowed reflectivity is 53 dBZ; values above 53 dBZ are set to 53 dBZ in an attempt to dismiss hail contamination (Vieux and Bedient, 1998), although this may still overestimate precipitation rates in areas of hail.

The data used only contain reflectivity and winds at a given altitude, therefore, standard Z-R relationships were used to convert reflectivity to rainfall rate. The 3 November 2000 and 26 September 2000 cases used the WSR-88D convective relationship for deep summer convection given by (3.3.2) within the wind-drift schemes applied, where $Z$ is the reflectivity given in $mm^6\ m^{-3}$ and $R$ is the rainfall rate in $mm\ h^{-1}$.

$$Z = 300R^{1.4} \tag{3.3.2}$$

The 18 November 2000 case for both schemes uses the Marshall-Palmer relationship for general stratiform precipitation given by (3.3.3) (Marshall and Palmer, 1948), where the variables are the same as in (3.3.2).

$$Z = 200R^{1.6} \tag{3.3.3}$$

These Z-R relationships were taken from those outlined by the NWS (NWFO WSR-88D Operations Memorandum, 1999).

The inclusion of topography was also incorporated within each of the wind-drift schemes in select runs. High-resolution topographic maps of New South Wales were matched to the native resolution of the given grids of reflectivity and wind velocities. The addition of topography allows for the reduction of error over mountainous terrain to the west (Fig. 3.3.1) due to the fact that the rain drops have a reduced distance to fall making the effect of wind-drift less. The inclusion of topography is accomplished by simply subtracting the average height of the terrain in the grid from the height of the CAPPI height to yield a new fall height, thus a new fall time, and a smaller drift component.

## 3.4 Schemes

### 3.4.1 Bulk-advection Scheme

In either adjustment scheme, the first step in the process to generate a new field of surface rainfall rate by taking into account wind-drift is to calculate a fall time for the drops within one pixel. In the bulk-advection case, this is accomplished by assuming that all droplets within one pixel have one average droplet diameter. This assumption makes it possible to can apply any Z-R relationship to convert reflectivity to a rainfall rate assumed to be uniform throughout the entire pixel. An equation (3.4.1) relating rainfall rate ($R$) in mm $h^{-1}$ to fall speed ($V_f$) in m $s^{-1}$, derived from Lacy (1977), can be incorporated.

$$V_f = 4.5R^{(1/9)} \tag{3.4.1}$$

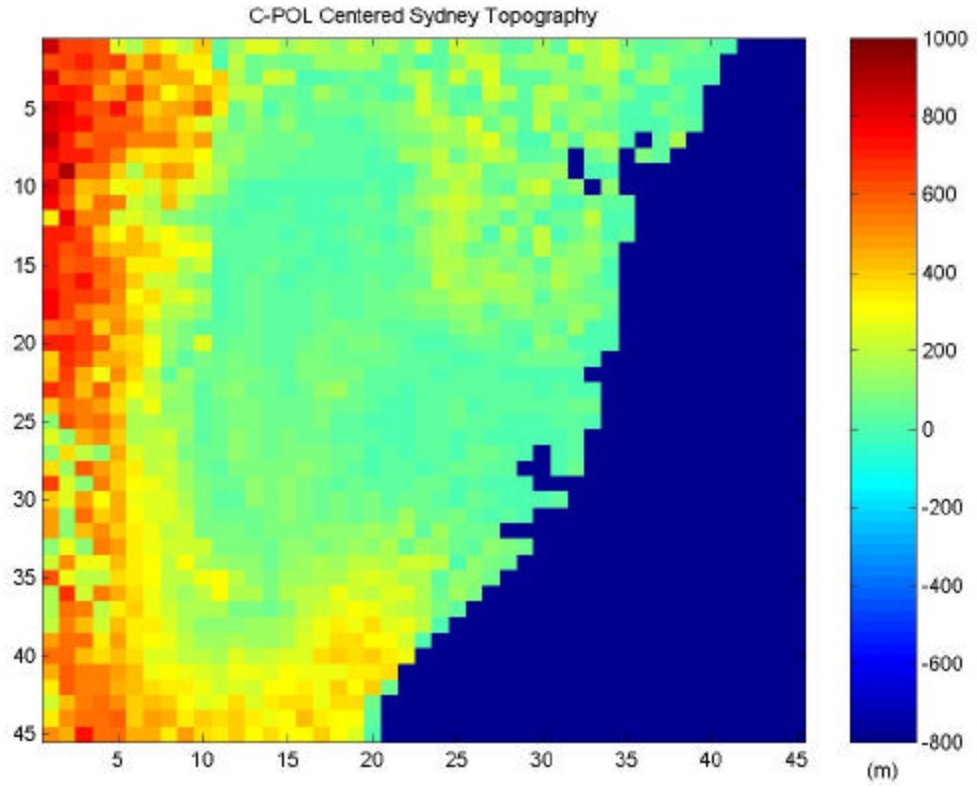


**Figure 3.4.1:** CPOL centered topography matched to a resolution of the native horizontal dimension of the data used in this research (2.5 km x 2.5 km). The negative values over the water are simply used to easily distinguish land from sea, within the scheme water is assumed to be sea level (0 m).

Once fall speed is calculated the time it takes for the entire grid square represented by the average droplet to fall a certain distance can be found. This is found by simply dividing the height of the CAPPI height by the fall speed modified by simply adding the w component of the wind to simulate the effects of updrafts or downdrafts (Austin, 1987). A simplified example of the bulk-advection scheme can be seen in Table 3.4.1. The output is the result of a 40 dBZ return (10000 $mm^6$ $m^{-3}$) being located in the upper left hand corner of the grid and all other grids having no return. The northwesterly wind advects the precipitation to the other grid squares. The upper grid is for the convective Z-R relationship and the lower

| **Convective Bulk-advection** | | | | |
|---|---|---|---|---|
| 590.15 | 1839.15 | 0 | 0 | 0 |
| 1839.15 | 5731.57 | 0 | 0 | 0 |
| 0 | 0 | 0 | 0 | 0 |
| 0 | 0 | 0 | 0 | 0 |
| 0 | 0 | 0 | 0 | 0 |
| **Stratiform Bulk-advection** | | | | |
| 565.93 | 1812.99 | 0 | 0 | 0 |
| 1812.99 | 5808.07 | 0 | 0 | 0 |
| 0 | 0 | 0 | 0 | 0 |
| 0 | 0 | 0 | 0 | 0 |
| 0 | 0 | 0 | 0 | 0 |

**Table 3.4.1:** Theoretical results from the bulk-advection scheme for both the convective and stratiform cases expressed in ($mm^6\ m^{-3}$). The upper left hand corner starts with a reflectivity of 40 dBZ (10000 $mm^6\ m^{-3}$) and is advected by a u component wind of 6 m $s^{-1}$ and a v component of -6 m $s^{-1}$.

for stratiform; notice the stratiform precipitation gets spread further due to the slower fall speed.

## 3.4.2 Drop-sorting Scheme

In the drop-sorting case the estimation of fall speed arises from a distribution of droplets divided into 25 drop-size bins. For the convective case the drop-size bins range from 0 mm to 7.5 mm at an interval of 0.3 mm. Therefore, the first drop-size bin is 0 – 0.299 mm and the calculated average drop diameter is 0.1495 mm. For the stratiform case, the drop-size bins range from 0

mm to 5.0 mm at an interval of 0.2 mm. Therefore, the first drop-size bin is 0 – 0.199 mm and the calculated average drop diameter within this bin is 0.0995 mm. The arithmetic average for mean drop diameter was used to simply decrease the computational time of the program. A more accurate method of finding the mean drop diameter is a weighted mean approach, a function of the number of drops per bin for each size. The integrated form of the weighted mean approach, assuming the Marshall-Palmer exponential distribution, is found below (equation 3.4.2), where *?* is given by equation (3.4.5).

$$\overline{D} = \frac{\left(\frac{e^{-\Lambda D_u}}{-\Lambda^2}(-\Lambda D_U - 1)\right) - \left(\frac{e^{-\Lambda D_L}}{-\Lambda^2}(-\Lambda D_L - 1)\right)}{\left(\frac{e^{-\Lambda D_u}}{-\Lambda}\right) - \left(\frac{e^{-\Lambda D_L}}{-\Lambda}\right)} \tag{3.4.2}$$

The underlying idea of using the weighted mean is to correct for the possible overestimation that is occurs when using a mean drop-size diameter that is too large (as is done within the scheme). As shown by the error statistics of the case studies underestimation is the norm. The underestimation is a result of losing some returns out of the domain. The small drop-size bins create an insignificant difference between the arithmetic mean approach and the weighted mean approach (Table 3.4.2). If larger drop-size bins were used it could have a significant impact on both the magnitude of the wind-drift and the overall power distribution after the schemes are applied.

Bins in table 3.4.2 were selected because they had the greatest power differences in the range of the 25 bins. Even when raising the diameter to the sixth power to calculate the power contribution to each bin the difference is rather insignificant. Since the stratiform case has generally weaker power returns and uses a narrower bin size of 0.2 mm the difference between the two mean calculations is even smaller. The weighted mean should be used in future

| Bin Upper | Bin Lower | Arithmetic Mean | Weighted Mean | Z(bin A) | Z(bin W) | % Difference |
|---|---|---|---|---|---|---|
| 2.999 | 2.70 | 2.85 | 2.83 | 1128.65 | 1086.74 | 3.86 |
| 2.699 | 2.40 | 2.55 | 2.53 | 1198.84 | 1149.17 | 4.32 |
| 2.399 | 2.10 | 2.25 | 2.23 | 1171.20 | 1116.33 | 4.92 |
| 2.099 | 1.80 | 1.95 | 1.93 | 1027.40 | 972.03 | 5.70 |
| 1.799 | 1.50 | 1.65 | 1.63 | 780.54 | 731.03 | 6.77 |

**Table 3.4.2:** The difference between using the arithmetic mean native to the original programming or the weighted mean from the convective drop-size bins. The bins selected were the most significant change in power.

developments of the wind-drift schemes, however, as it is physically more meaningful than a simplified arithmetic mean.

The fall speed of the droplets is found by applying the relationships given by Rogers and Yau (1989) based on the average drop radius in each bin (3.4.3a and 3.4.3b).

$$V_f = k_2 r, 40mm < r < 600mm \, (k_2 = 8*10^3 s^{-1}) \tag{3.4.3a}$$

$$V_f = k_3 r^{0.5}, r > 600mm \, (k_3 = 2.2*10^3 (r_{a0} / r_a)^{0.5} \, cm^{0.5} s^{-1}) \tag{3.4.3b}$$

Depending on the CAPPI, the fall speed of the droplets within a given bin is dependent on the density of the air $(r_a)$ at that altitude. In the case of drop-sorting, the time it takes to fall to the surface can be calculated for each bin. This allows for more dispersion of the intensity given by one grid square to other nearby grid squares based upon the number of droplets in each bin.

The number of droplets in any given bin is found by integrating a modified Marshall-Palmer distribution function for the stratiform, using (3.4.2),

and convective case, using (3.4.3). The coefficients of (2.2.1) are given by (3.4.4) and (3.4.5).

$$\Lambda = 4.1R^{-0.2095} \text{ (conv)}; \ \Lambda = 4.1R^{-0.205} \text{ (strat)} \tag{3.4.4}$$

$$N_0 = 99.869e^{0.0617Z} \text{ (conv)}; \ N_0 = 44.405e^{0.0869Z} \text{ (strat)} \tag{3.4.5}$$

The resulting modified Marshall-Palmer relationship allows for the discrete nature of the DSD for a given convective or stratiform case. When dividing a grid of reflectivity into 25 drop-size bins there can be no, or almost no, loss or gain of power. Equations (3.4.4) and (3.4.5) fit the data so that the original grid of reflectivity is approximately the same when the drop-size bins are allowed to be advected by the wind given in that grid square. Equations (3.4.4) and (3.4.5) are the results of adding a trendline to the data and using the equation given by the curve of the trendline.

The number of drops per bin are then calculated by integrating the Marshall-Palmer given by (2.2.1), as is given by (3.4.6), where $D_U$ and $D_L$ are the upper and lower diameters, respectively, for the given drop-size bin.

$$N_d = (-N_0 \Lambda e^{-\Lambda D_U}) - (-N_0 \Lambda e^{-\Lambda D_L}) \tag{3.4.6}$$

The power from each drop-size bin is then calculated by using the number of drops per bin multiplied by the mean diameter of the bin to the sixth power given by (3.4.7).

$$Z = N_d \overline{D}^6 \tag{3.4.7}$$

To ensure approximately no reflectivity is lost or gained; the reflectivity from all 25 bins is summed and compared to the original reflectivity of the given grid square. It was found that the equations used accomplish nearly no loss or gain (<2%) of reflectivity from the dividing the reflectivity of one grid square into 25 size bins.

The time it takes for each bin of drops to impact the surface is calculated by the same method as the bulk-advection case from the previous section. The drop-sorting scheme is more physically realistic (Atlas and Plank, 1953) than the bulk-advection scheme, in that; it takes into account drop-size distributions instead of assuming a mean droplet for each grid square. A simplified example of the drop-sorting scheme is shown in Table 3.4.3. The output is the result of a 40 dBZ return (10000 $mm^6$ $m^{-3}$) being located in the upper left hand corner of the grid and all other grids having no return. The northwesterly wind advects the precipitation to the other grid squares. The above grid is for the convective Z-R relationship and the bottom for stratiform; notice the stratiform precipitation is spread further due to the slower fall speed. It is also important to note that the reflectivity spreads to more cells than in the bulk-advection scheme shown in Table 3.4.1.

## 3.5 Summary

The two schemes used for this research are a simplified bulk-advection scheme and a more complex drop-sorting scheme. The basic concepts are the same; they use the same Z-R relationships, depending upon the event examined. They also use the same methods for calculating the horizontal drift of each grid. Both schemes implicitly handle convergence and divergence because precipitation is affected by real wind shifts given by the adjoint model and Doppler wind fields. Each scheme also handles topography in a similar manner.

The differences are a result of how the fall speed is calculated and how the precipitation from one grid square is allowed to advect to other grid squares. In

| **Convective Drop-sorting** | | | | |
|---|---|---|---|---|
| 1134.14 | 1964.72 | 0 | 0 | 0 |
| 1964.72 | 4808.49 | 29.37 | 0 | 0 |
| 0 | 29.37 | 17.43 | 1.35 | 0 |
| 0 | 0 | 1.35 | 1.51 | 0 |
| 0 | 0 | 0 | 0 | 0 |
| **Stratiform Drop-sorting** | | | | |
| 1042.90 | 1943.44 | 0 | 0 | 0 |
| 1943.44 | 5090.84 | 31.22 | 0 | 0 |
| 0 | 31.22 | 23.29 | 1.45 | 0 |
| 0 | 0 | 1.45 | 0.56 | 0.08 |
| 0 | 0 | 0 | 0.08 | 0.36 |

**Table 3.5.1:** Theoretical results from the drop-sorting scheme for both the convective and stratiform cases. The upper left hand corner starts with a reflectivity of 40 dBZ (10000 $mm^6$ $m^{-3}$) and is advected by a u component wind of 6 m $s^{-1}$ and a v component of -6 m $s^{-1}$.

the bulk-advection scheme, the fall speed is based on a rainfall rate approximated by a Z-R relationship. This fall speed is constant for all drops within the square, so it is assumed that the droplets in the grid must have the same size. This implies that the dimensions of the initial grid must remain unchanged as it is advected to a new location (Fig. 3.5.1). For the drop-sorting scheme, a distribution of drop-sizes is accounted for by dividing each pixel of reflectivity into 25 drop-size bins using adjusted Marshall-Palmer relationships. This allows for drops of different sizes to have different fall speeds resulting in different magnitudes of wind-drift. The result is a more physically realistic scheme than the bulk-advection scheme, as it is known that drop-sorting exists (*i.e.* Atlas and Plank, 1953). The reflectivity for a given grid cell disperses more than the bulk-advection scheme, especially for cases of stratiform precipitation

types. The dimension of the original pixel of reflectivity does not have to hold constant as is the case for the bulk-advection scheme as there are now 25 size bins to be advected instead of an approximate mean size for one original grid (Fig. 3.5.2). The drop-sorting scheme with its higher level of complexity results in a longer computational time. With today's computing power this should not be an issue as most of these experiments were run effectively on a PC with a 2.4 GHz processor.

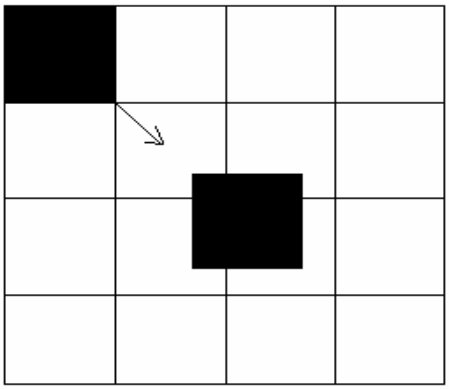

**Figure 3.5.1:** A simplified illustration of the bulk-advection scheme showing that the dimensions of the advected grid square remains constant since an approximate mean diameter of drops is assumed.

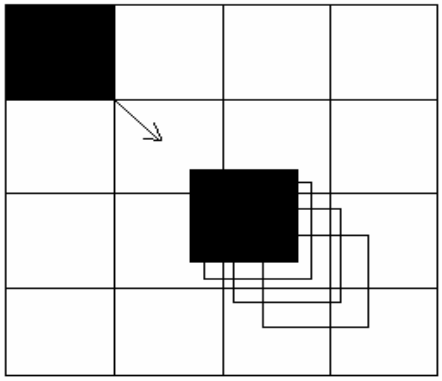

**Figure 3.5.2:** A simplified illustration of the drop-sorting scheme showing that the spread of reflectivity does not remain the same as the original grid dimensions due to the division into 25 drop-size bins with different fall speeds. Only 4 size bins are shown in this example, but in reality there should be 25 different squares of the same dimensions.

# Chapter 4 Results

The results for each of the case studies will be displayed in the following subsections in a similar way. The severe convective case from 3 November 2000 and the stratiform case from 18 November 2000 contain results from both the bulk-advection and drop-sorting schemes at different CAPPIs and horizontal resolutions. The 26 September 2000 case is only an evaluation of the bulk-advection case due to time constraints. In all cases, the first of the results are from the schemes run without the inclusion of topography and in the second topography is included.

The results will be displayed for the native resolution and several hypothetical resolutions to the scale of urban hydrological applications. The field of urban planning and nowcasting is becoming a new focus in meteorology. Complex flow patterns in the atmosphere can vary to a high extent within the urban realm; however, this also includes surface runoff and other hydrological parameters, not just flow patterns aloft and an examination of the possible error in measurements on this scale is necessary. The experiments will show comparisons, both graphically and numerically, between the original rainfall derived from radar and the rainfall after the wind-drift adjustments have been made. A summary of selected statistics will also be displayed for each individual case.

The final subsection will contain an experiment incorporating beam elevations in place of constant elevation grids. The scheme used in this experiment is the drop-sorting scheme on the 3 November 2000 case. A similar comparison of possible error will be shown for these results.

The images were created by the MATLAB program and the numeric data were saved and manipulated in Microsoft Excel. The images and tables displayed come from these sources.

## 4.1 3 November 2000 Case

The 3 November case used in this study was unique in that it was a severe event including three tornadoes, damaging wind gusts, 7-cm hail, and flash flooding (Sills *et al.*, 2004). The synoptic environment was characterized by a slowly eastward propagating trough that reached New South Wales (NSW) by late day. The upper-level jet during this time was well away from the Sydney area. Most of the region was under clear to partly cloudy skies; however, the synoptic forcing throughout the region was relatively weak (Sills *et al.*, 2004). There was a sea breeze front moving inland at the time and this aided the development of deep convection. CAPE (convective available potential energy) values were 995 J $kg^{-1}$ with the wet-bulb zero around 2750 m, providing the chance for large hail to occur near Sydney (Sills *et al.*, 2004).

Three distinct severe storm cells developed during the afternoon of 3 November (Fig. 4.1.1). Some of the severe weather reported with these storms included three F0 tornadoes (one briefly reached F1 strength), golf-ball-sized hail, and a report of 24 mm of rain in 8 min (Fig. 3.1.1). Reflectivities from the CPOL radar at times were well over 60 dBZ.

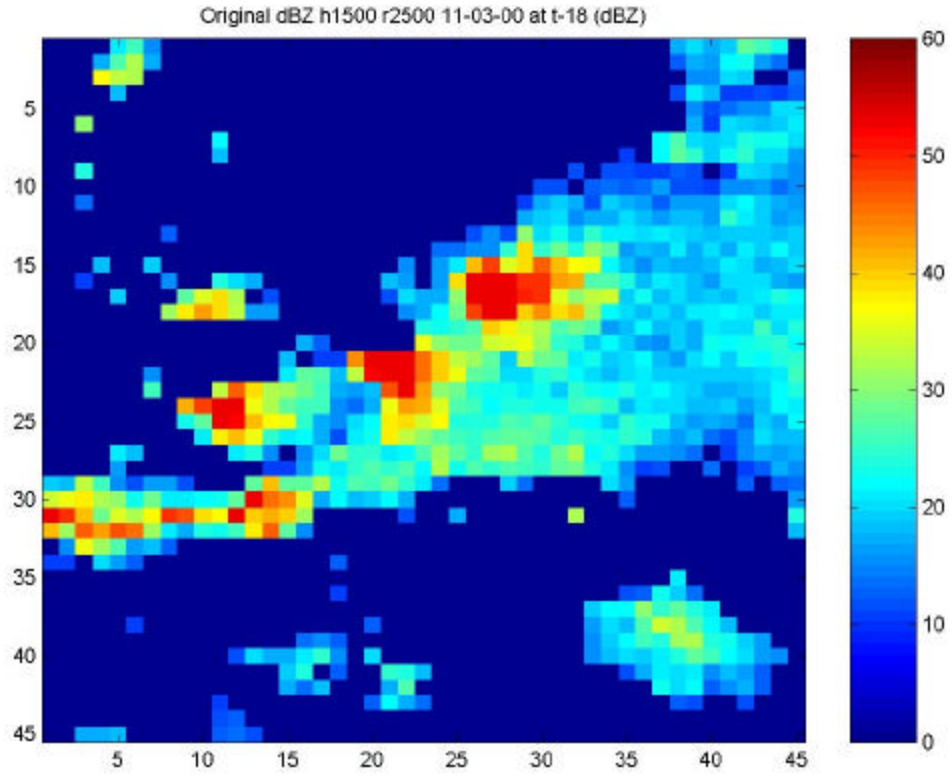


**Figure 4.1.1**: Reflectivity (in dBZ) at the final time step used for the convective case on 3 November 2000. The grid resolution is 2.5 km and the CAPPI height is 1.5 km. The three distinct severe storm cells are easily identified.

### 4.1.1 Schemes at 1.5-km height and 2.5-km resolution

The first set of results comes from the severe convective case on 3 November 2000 at the native resolution of 2.5 km and CAPPI height of 1.5 km. The images show the comparison of the original rainfall amounts from the raw reflectivity to the bulk-advection scheme and drop-sorting scheme rainfall amounts after the final time step in the 3-h period (Fig. 4.1.2). The convective Z-R relationship is used for this case given by equation 3.3.2. As previously noted, values higher than 53 dBZ are set to 53 dBZ to remove possible hail contamination. Even after the filtering of high reflectivity values, there are

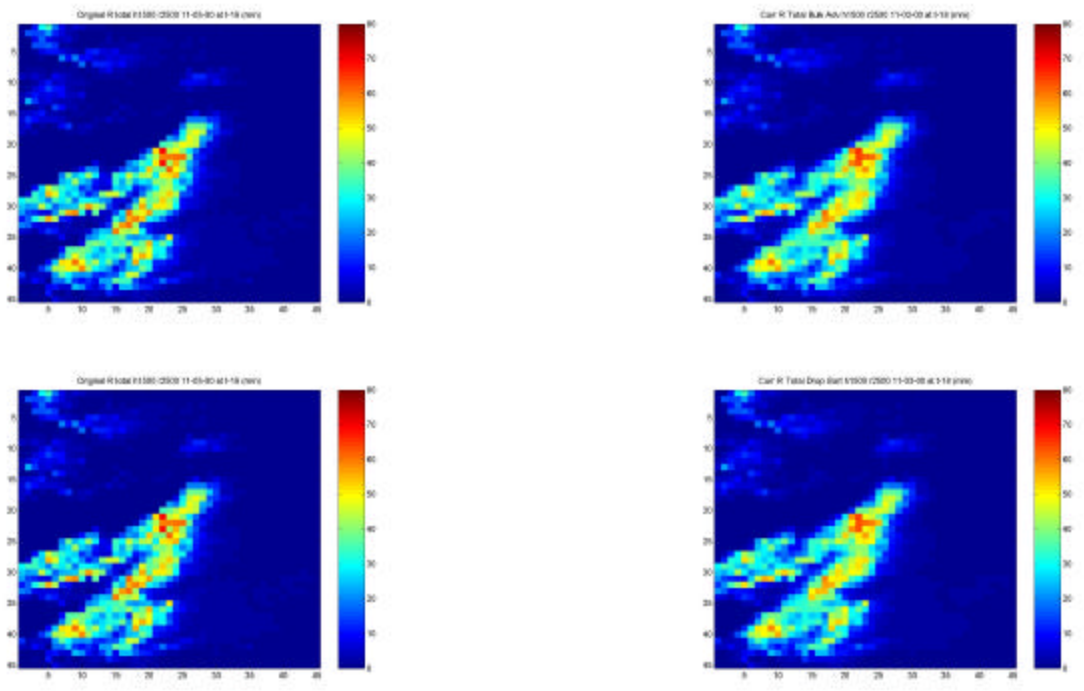

**Figure 4.1.2:** Original rainfall total after 3 h for the 3 November 2000 case (upper and lower left) with the bulk-advection scheme (upper right) and the drop-sorting scheme (lower right) rainfall totals after 3 h at the native CAPPI height of 1.5 km and the native horizontal resolution of 2.5 km. The scale used is 0-80 mm.

some isolated areas toward the center of the image where rainfall amounts approach 70 mm after the 3 h period for the "raw" reflectivity and schemes accounting for wind-drift. For the bulk-advection adjusted image (upper right in Fig. 4.1.2) the isolated heavy precipitation areas from the raw image show slight dispersion and reduction in rainfall rate. The drop-sorting scheme shows similar results throughout the image, although there appears to be more dispersion and reduction in the heavier rainfall rates from the original image. Some of the differences in rainfall accumulation over the time period toward the center of the domain, where precipitation amounts are heaviest, can be seen numerically (Table 4.1.1). Overall, there is a similar dispersion of reflectivity and reduction in power in both schemes because the area of rainfall covers a larger area and the precipitation appears less intense than the "raw" radar reflectivity data.

| Original Rainfall Total | | | | | BA Rainfall Total | | | | | DS Rainfall Total | | | |
|---|---|---|---|---|---|---|---|---|---|---|---|---|---|
| 0.03 | 0.29 | 7.28 | 27.85 | | 0.88 | 4.29 | 12.77 | 31.96 | | 0.83 | 4.07 | 12.40 | 31.41 |
| 0.94 | 21.43 | 18.44 | 31.48 | | 7.52 | 21.30 | 22.67 | 35.68 | | 7.12 | 21.01 | 22.10 | 35.05 |
| 34.68 | 36.72 | 41.92 | 48.93 | | 39.49 | 38.30 | 44.09 | 47.77 | | 38.64 | 37.59 | 43.40 | 47.19 |
| 69.37 | 44.46 | 48.39 | 40.26 | | 65.33 | 48.25 | 46.62 | 37.75 | | 64.43 | 47.51 | 46.14 | 37.67 |
| 59.59 | 59.58 | 60.01 | 61.12 | | 64.42 | 61.37 | 60.45 | 54.72 | | 63.29 | 60.42 | 59.65 | 54.46 |
| 67.72 | 41.49 | 56.19 | 40.04 | | 63.45 | 48.91 | 52.21 | 35.62 | | 62.66 | 47.86 | 51.68 | 35.83 |
| 39.80 | 62.05 | 49.14 | 43.17 | | 52.21 | 57.57 | 47.14 | 36.59 | | 51.22 | 56.97 | 46.64 | 36.66 |

**Table 4.1.1:** Comparison of total rainfall after 3 h (in mm) for the 3 November 2000 case from a selected area that covers the grid from cell (22,18) to (25,24) for the bulk-advection (BA) scheme and drop-sorting (DS) scheme at the native CAPPI height of 1.5 km and horizontal resolution of 2.5 km.

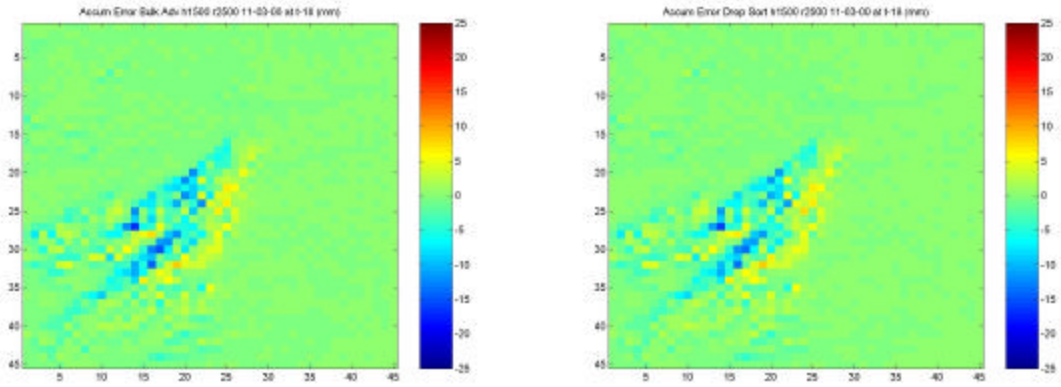

**Figure 4.1.3: E**stimated accumulation error after 3 h (in mm) for the 3 November 2000 case for the bulk-advection scheme (left) and the drop-sorting scheme (right) at the native CAPPI height of 1.5 km and the native horizontal resolution of 2.5 km.

The estimated accumulation error was calculated by simply taking the accumulated rainfall from the original reflectivity after each time step and subtracting the scheme's adjusted rainfall accumulation. Error refers to the difference between the wind-drift adjustment and the original rainfall amounts derived from the "raw" reflectivity. Underestimation appears as negative values and cool colors, whereas overestimation appears as positive values and warmer colors. The green regions are areas of negligible differences in accumulation. For

this case, there is a coupling of underestimation with overestimation along the axis of the northeasterly storm track for both schemes (Fig. 4.1.3). Some of the more intense underestimations are on the order of -20 mm over the 3-h accumulation period. These errors cover a spatial range of about 15 km in one direction across the axis of the storm track as revealed by Fig. 4.1.3. From the selected areas in Table 4.1.1, there is a large difference between the original rainfall amounts and the rainfall amounts given by the two schemes in the lower-left corner.

### 4.1.2 Schemes at 1.5-km height and 0.5-km resolution

The next set of results for the severe convective case involves the horizontal resolution increased to 0.5 km, while the CAPPI height is still set to 1.5 km (native). These results simulate a scale close to that necessary for use in urban hydrology. As before, the first images deal with the comparison of rainfall totals from the "raw" reflectivity to the adjusted rainfall totals from the bulk-advection and drop-sorting schemes.

The rainfall total comparison between the original rainfall total after 3 h using bulk-advection and drop-sorting scheme at the increased horizontal resolution is shown both graphically (Fig. 4.1.4) and numerically (Table 4.1.3). In the adjusted image, there is an enhanced dispersion effect that takes place when applying the wind-drift on a fine scale. The dispersion effect is greater on the resolution of 0.5 km than on the native resolution shown in the previous section. The areas of highest rainfall returns near the center of the image are spread more continuously in the adjusted image without losing much of the rainfall amounts. There is a reduction of rainfall amounts to the west of the image where the wind

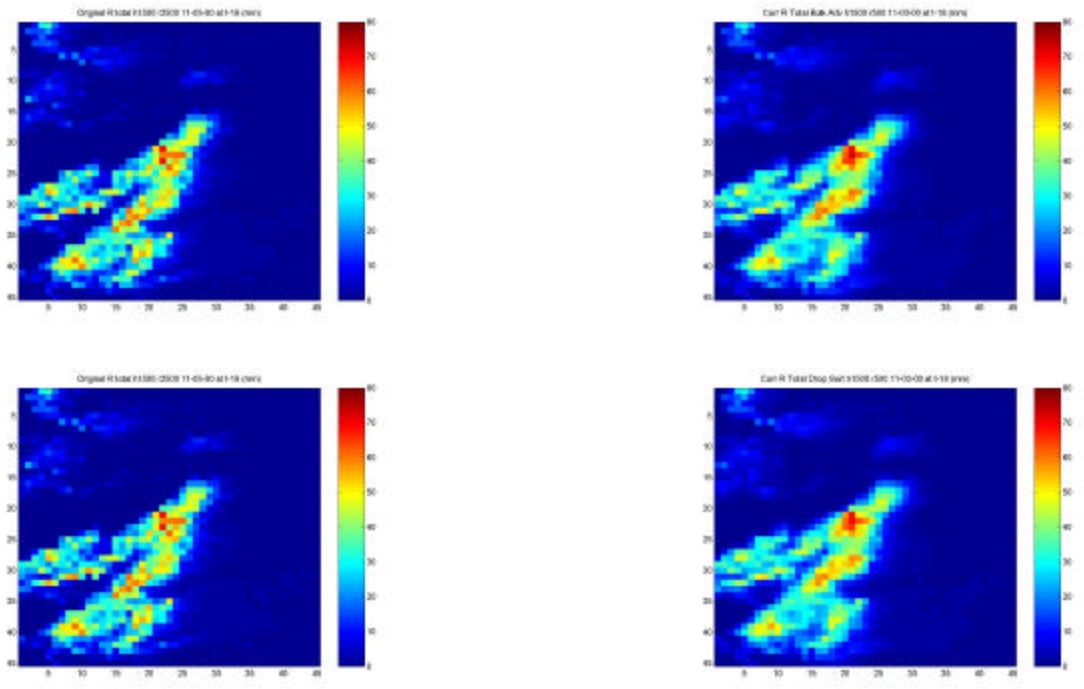

**Figure 4.1.4:** Original rainfall total after 3 h for the 3 November 2000 case (upper and lower left) with the bulk-advection scheme (upper right) and drop-sorting scheme (lower right) rainfall totals after 3 h at the native CAPPI height of 1.5 km and the horizontal resolution increased to 0.5 km. The scale used is 0-80 mm.

acts to disperse the rainfall totals more efficiently, especially in the drop-sorting scheme. The oranges and reds found in the original rainfall total image on the western side become a larger, less intense region after the bulk-advection scheme is applied using a horizontal resolution of 0.5 km.

The estimated accumulation error resulting from the difference of the original rainfall total over 3 h and the bulk-advection scheme at a horizontal resolution of 0.5 km is shown Fig. 4.1.5. The estimated accumulation error image reveals the significance of increasing the horizontal resolution. Allowing wind-drift to affect precipitation at this scale shows that almost none of the precipitation from the grid squares directly above falls in the same grid square at

| Original Rainfall Total | | | | | BA Rainfall Total | | | | | DS Rainfall Total | | | |
|---|---|---|---|---|---|---|---|---|---|---|---|---|---|
| 0.03 | 0.29 | 7.28 | 27.85 | | 7.14 | 12.37 | 25.42 | 39.64 | | 6.91 | 11.65 | 24.84 | 38.50 |
| 0.94 | 21.43 | 18.44 | 31.48 | | 20.10 | 21.51 | 30.32 | 50.41 | | 19.09 | 21.16 | 30.63 | 47.35 |
| 34.68 | 36.72 | 41.92 | 48.93 | | 37.62 | 40.46 | 43.68 | 43.87 | | 38.40 | 40.12 | 43.86 | 43.72 |
| 69.37 | 44.46 | 48.39 | 40.26 | | 49.01 | 45.90 | 37.28 | 27.13 | | 49.64 | 45.89 | 37.93 | 28.08 |
| 59.59 | 59.58 | 60.01 | 61.12 | | 63.80 | 59.12 | 50.02 | 29.20 | | 62.64 | 58.59 | 51.49 | 31.36 |
| 67.72 | 41.49 | 56.19 | 40.04 | | 52.90 | 46.60 | 32.17 | 20.51 | | 51.93 | 47.43 | 33.84 | 21.51 |
| 39.80 | 62.05 | 49.14 | 43.17 | | 50.64 | 43.26 | 30.11 | 17.45 | | 51.76 | 43.67 | 32.13 | 17.94 |

**Table 4.1.2:** Comparison of total rainfall after 3 h (in mm) for the 3 November 2000 case from a selected area that covers the grid from cell (22,18) to (25,24) for the bulk-advection (BA) scheme and drop-sorting (DS) scheme at the native CAPPI height of 1.5 km and increased horizontal resolution of 0.5 km.

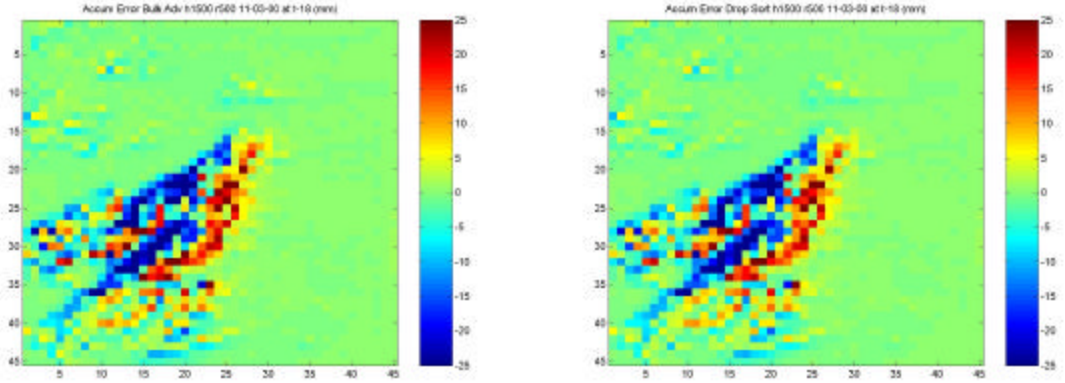

**Figure 4.1.5:** Estimated accumulation error after 3 h (in mm) for the 3 November 2000 case for the bulk-advection scheme (left) and the drop-sorting scheme (right) at the native CAPPI height of 1.5 km and the horizontal resolution increased to 0.5 km.

the surface. Although the rainfall scale on the image is ± 25 mm, the magnitudes of the errors approach 50 mm in some grid squares over the selected 3-h period.

### 4.1.3 Schemes at 0.75-km height and 0.5-km resolution

The next set of images is a result of an increased horizontal resolution of 0.5 km while reducing the CAPPI height to 0.75 km. The effect of lowering the

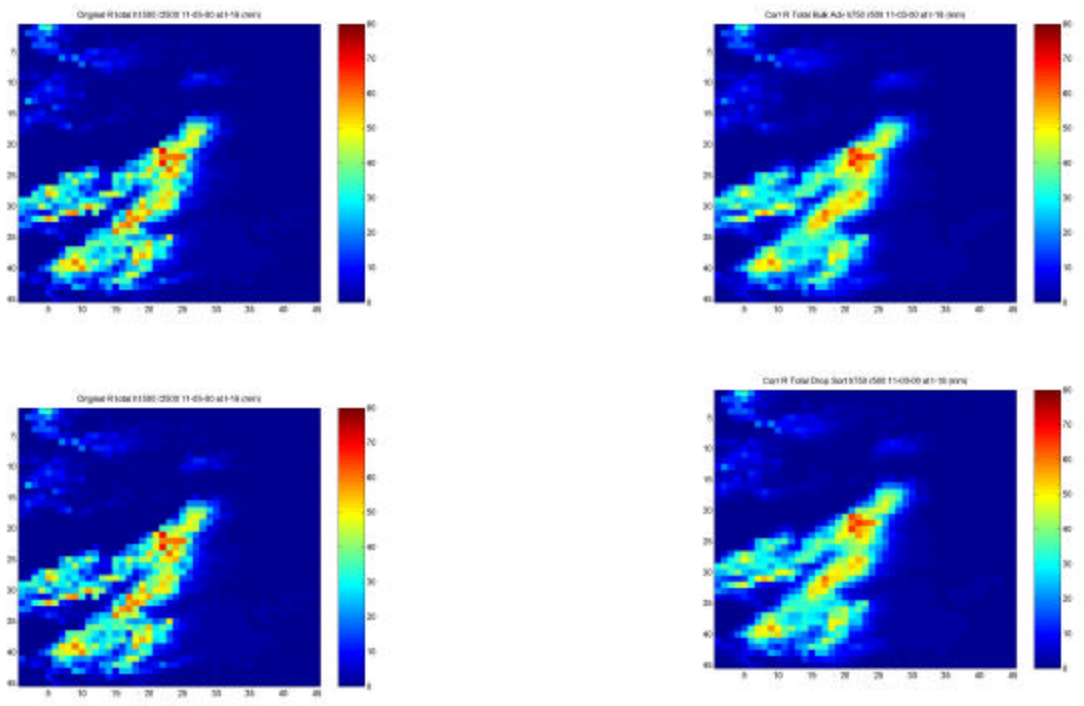

**Figure 4.1.6:** Original rainfall total after 3 h for the 3 November 2000 case (upper and lower left) with the bulk-advection scheme (upper right) and drop-sorting scheme (lower right) rainfall totals after 3 h at the CAPPI height set to 0.75 km and the horizontal resolution increased to 0.5 km. The scale used is 0-80 mm.

CAPPI height reduces the distance that wind-drift will affect falling precipitation and is more realistic in near-radar estimations of precipitation. Keeping the increased resolution of 0.5 km increases the error due to wind-drift, however. The first images are the rainfall comparisons for the different schemes (Fig. 4.1.6) and the subsequent images are the estimated accumulation error comparison of the two schemes (Fig. 4.1.7). The selected numerical values in rainfall totals for each scheme along with the rainfall totals derived from the original reflectivity field are also shown (Table 4.1.3).

The comparison of the bulk-advection and drop-sorting scheme to the original rainfall total in this case is similar to the comparison of the case of only

| Original Rainfall Total | | | | | BA Rainfall Total | | | | | DS Rainfall Total | | | |
|---|---|---|---|---|---|---|---|---|---|---|---|---|---|
| 0.03 | 0.29 | 7.28 | 27.85 | | 2.80 | 7.89 | 18.56 | 35.86 | | 2.62 | 7.48 | 17.84 | 35.11 |
| 0.94 | 21.43 | 18.44 | 31.48 | | 13.63 | 20.86 | 26.85 | 41.34 | | 12.89 | 20.60 | 26.06 | 40.32 |
| 34.68 | 36.72 | 41.92 | 48.93 | | 41.39 | 39.50 | 45.21 | 46.15 | | 40.57 | 38.76 | 44.50 | 45.69 |
| 69.37 | 44.46 | 48.39 | 40.26 | | 58.46 | 49.39 | 43.79 | 33.33 | | 58.21 | 48.68 | 43.61 | 33.64 |
| 59.59 | 59.58 | 60.01 | 61.12 | | 66.42 | 62.33 | 60.08 | 44.36 | | 65.26 | 61.26 | 59.45 | 45.04 |
| 67.72 | 41.49 | 56.19 | 40.04 | | 56.50 | 54.26 | 43.92 | 28.23 | | 56.56 | 52.89 | 44.36 | 29.15 |
| 39.80 | 62.05 | 49.14 | 43.17 | | 59.21 | 50.86 | 42.83 | 26.30 | | 58.08 | 51.00 | 42.74 | 27.30 |

**Table 4.1.3:** Comparison of total rainfall after 3 h (in mm) for the 3 November 2000 case from a selected area that covers the grid from cell (22,18) to (25,24) for the bulk-advection (BA) scheme and drop-sorting (DS) scheme at the reduced CAPPI height of 0.75 km and increased horizontal resolution of 0.5 km.

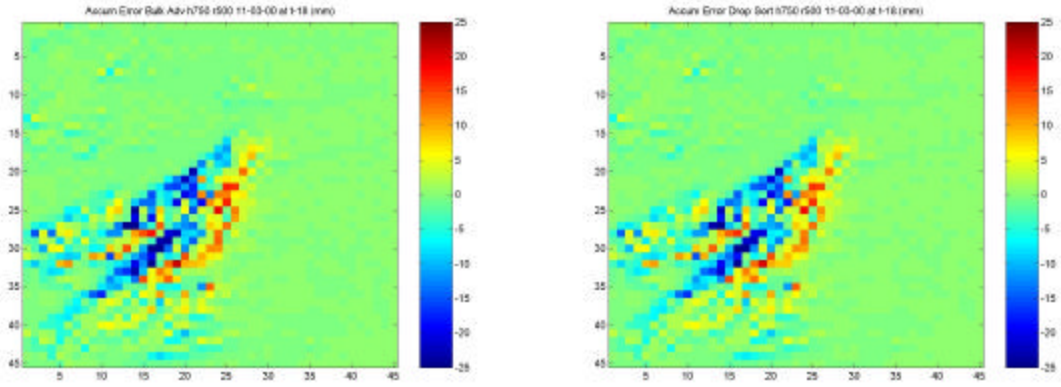

**Figure 4.1.7:** Estimated accumulation error after 3 h (in mm) for the 3 November 2000 case for the bulk-advection scheme (left) and the drop-sorting scheme (right) at the CAPPI height set to 0.75 km and the horizontal resolution increased to 0.5 km.

increasing the horizontal resolution, but not decreasing the CAPPI, in that, the rainfall totals seem to be similarly dispersed in the adjusted cases (Fig. 4.1.4). Although the image is similarly dispersed to the case with the 0.5 km horizontal resolution, the overall intensity of the isolated heavier areas appears to be decreased in the case where we also decrease the CAPPI. This is especially noticed in the south-central portions of the storm track; rainfall totals are much

more isolated and intense in the "raw" case as opposed to the adjusted case in either scheme.

The estimated accumulation error images (Fig. 4.1.7) show a similar pattern of over- and underestimation in rainfall totals after 3 h for both schemes. The values are also similar to the images with the increased horizontal resolution but native CAPPI height since the same color scale is used. However, the maximum magnitude of the error estimations for the images is approximately 30 mm over the 3-h period. This is caused by the CAPPI height being lower, thus decreasing the magnitude of wind-drift.

### 4.1.4 Schemes with Topography and 2.5-km resolution

The following cases are runs from the bulk-advection and drop-sorting schemes with the inclusion of topography for the severe convective case on 3 November 2000. The fall time of the droplet is found by multiplying the droplet fall speed by the difference in the native CAPPI height of 1500 m and the height of the terrain shown by Fig. 3.3.1. The results are displayed similarly to the previous cases without topography. The horizontal resolutions displayed are the native 2.5-km resolution and the increased resolution of 0.5 km. The CAPPI height remains unchanged at 1.5 km as the terrain in the west approaches or exceeds 800 m.

The first set of images (Fig. 4.1.8) shows similar results to the native resolution and CAPPI height runs for both schemes without the inclusion of topography (Fig 4.1.2). There are some small differences in the images, but they are unnoticeable without close examination. The areas that are most affected by the inclusion of topography are those to the west of the image. There is less of a

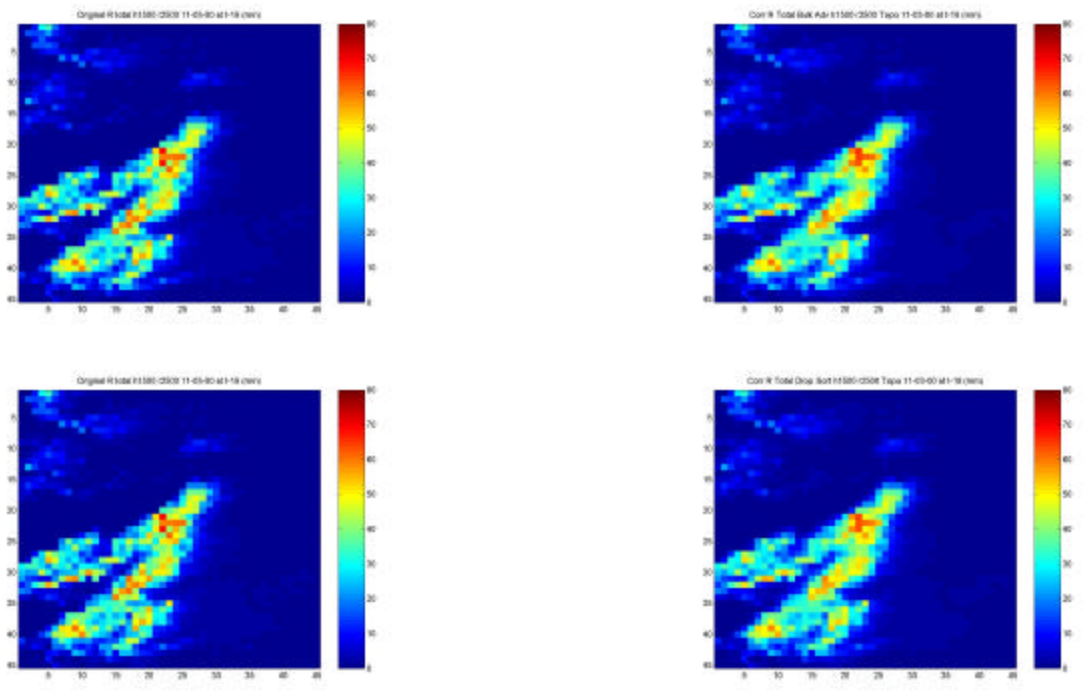

**Figure 4.1.8:** The original rainfall total after 3 h for the 3 November 2000 case (upper and lower left) with the bulk-advection scheme (upper right) and drop-sorting scheme (lower right) rainfall total after 3 h at the native CAPPI height of 1.5 km and the native horizontal resolution of 2.5 km with topography included. The scale used is 0-80 mm.

wind-drift effect where the terrain is high, resulting in less dispersion of the rainfall amounts over the 3-h period.

The estimated accumulation error images (Fig. 41.9) from the run with topography included, at the native horizontal resolution and CAPPI, show similar results for both the bulk-advection and drop-sorting schemes. It is also similar to the case where topography is not included except in the extreme western portion of the image where there are slight differences (Fig. 4.1.3). The differences in the errors are better displayed in a table format (Table 4.1.4). The table to the left shows the errors without topography included, while it is included in the table to the right. The sampled error for the table comes from the western portions of the domain where there are considerable changes in

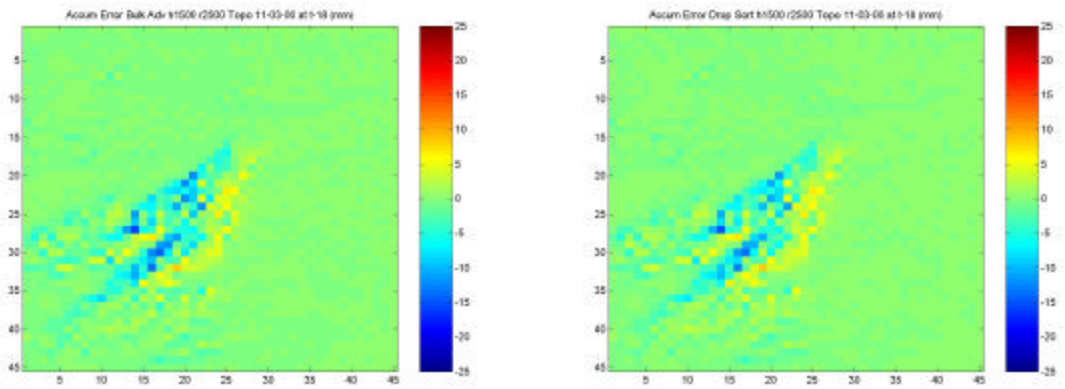

**Figure 4.1.9:** Estimated accumulation error (in mm) after 3 h for the 3 November 2000 case for the bulk-advection scheme (left) and drop-sorting scheme (right) at the native CAPPI height of 1.5 km and native horizontal resolution increased 2.5 km with topography included.

| **Topography Not Included** | | | | | **Topography Included** | | | |
|---|---|---|---|---|---|---|---|---|
| 0.01 | 0.00 | 0.01 | -0.01 | | 0.01 | 0.00 | 0.01 | 0.00 |
| 0.01 | -0.04 | -0.28 | -0.96 | | 0.01 | -0.03 | -0.23 | -0.80 |
| -0.04 | -2.65 | -3.44 | -2.08 | | -0.03 | -2.37 | -3.23 | -0.71 |
| -2.14 | -7.24 | 1.86 | -5.57 | | -1.80 | -4.81 | 1.01 | -4.51 |
| -0.81 | -1.30 | 1.65 | 0.64 | | -1.53 | -1.48 | 2.62 | 0.17 |
| 0.54 | -1.20 | -4.60 | 1.83 | | 0.20 | -0.48 | -4.28 | 1.98 |
| 1.59 | 0.19 | -0.39 | -1.82 | | 0.63 | 0.87 | -0.57 | -1.45 |
| -2.06 | -4.06 | -2.59 | -2.61 | | -2.26 | -2.63 | -1.73 | -2.48 |
| -0.33 | -0.30 | -1.33 | -3.80 | | 0.05 | -0.43 | -0.51 | -2.84 |

**Table 4.1.4:** Comparison of accumulation errors (in mm) after 3 h for grids on the extreme western side of the domain covering cells (1,25) to (4,33) from 3 November 2000 for the case without topography included (right) and the case with topography included (left). The scheme used for comparison was the drop-sorting scheme at the native horizontal resolution of 2.5 km.

elevation. The errors are of greater magnitude in the previous case because the 1500 m fall distance allows for more wind-drift effect.

### 4.1.5 Schemes with Topography and 0.5-km resolution

The rainfall total comparison for the case where the horizontal resolution is increased to 0.5 km and topography is included is shown by the next set of images (Fig. 4.1.10). Again, there are very subtle differences between the cases where topography is not included at this resolution (Fig. 4.1.4). The comparison between the original rainfall derived from the "raw" reflectivity and the wind-drift adjustments reveals a much smoother (not as pixelated) rainfall pattern in the adjusted cases. The magnitude of the rainfall totals is much smaller in the wind-drift adjusted scheme in the extreme western regions of the images.

The estimated accumulation error images (Fig. 4.1.11) from the program run with topography included at the increased horizontal resolution of 0.5 km show similar results for both the bulk-advection and drop-sorting schemes. Again, there is also a similarity to the case where topography is not included except in the extreme western portion of the image where there are slight differences (Fig. 4.1.5). The maximum magnitude of the errors reaches near 50 mm in some locations as was the case where topography was not included because most of the heavier precipitation was concentrated over lower elevations for most of the 3 h period. The differences in the errors for a sample area near the western portions of the domain are better displayed in a table format (Table 4.1.5). Again, the errors are of greater magnitude in the no-topography case as the effect of wind-drift is greater because the precipitation falls the entire CAPPI height of 1500 m.

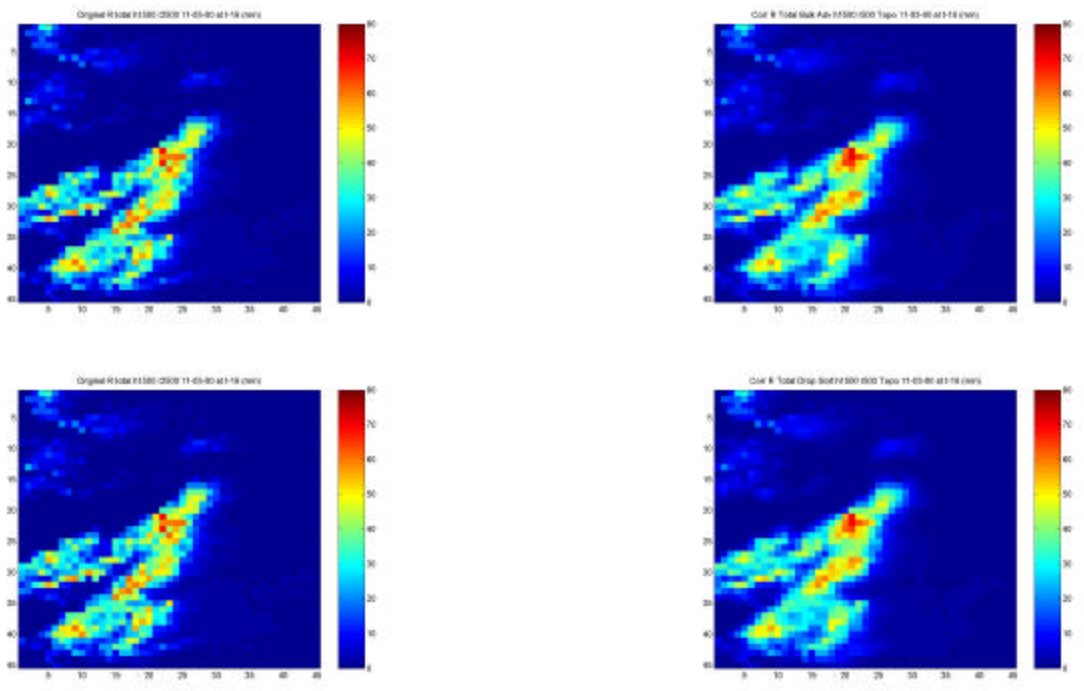

**Figure 4.1.10:** Original rainfall total after 3 h for the 3 November 2000 case (upper and lower left) with the bulk-advection scheme (upper right) and drop-sorting scheme (lower right) rainfall total after 3 h at the native CAPPI height of 1.5 km and the horizontal resolution increased to 0.5 km with topography included. The scale used is 0-80 mm.

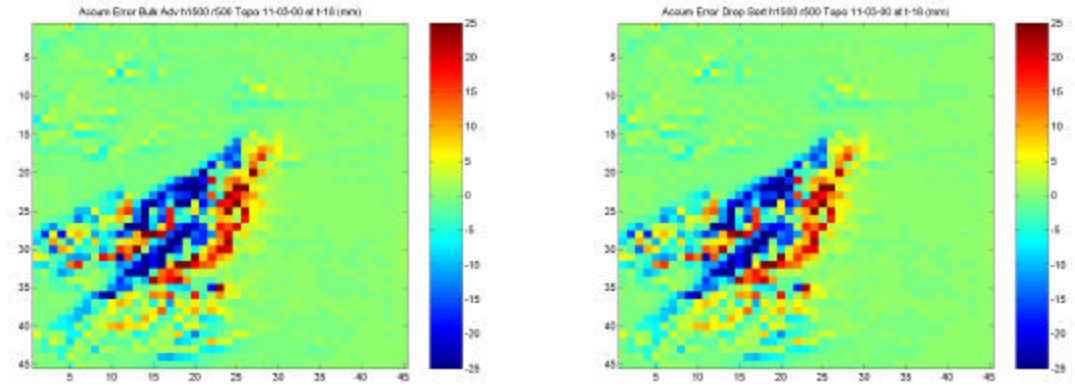

**Figure 4.1.11:** Estimated accumulation error (in mm) after 3 h for the 3 November 2000 case for the bulk-advection scheme (left) and drop-sorting scheme (right) at the native CAPPI height of 1.5 km and the horizontal resolution increased to 0.5 km with topography included.

| Topography Not Included | | | | | Topography Included | | | |
|---|---|---|---|---|---|---|---|---|
| 0.01 | 0.00 | 0.01 | -0.12 | | 0.01 | 0.00 | 0.01 | -0.11 |
| -0.03 | -0.41 | -2.13 | -3.96 | | -0.01 | -0.33 | -1.85 | -2.79 |
| -1.10 | -7.64 | -11.79 | -7.75 | | -0.60 | -6.89 | -11.14 | -3.08 |
| -7.69 | -21.78 | 8.17 | -20.59 | | -6.12 | -16.18 | 4.21 | -17.34 |
| -4.43 | -2.10 | 6.43 | 2.14 | | -7.99 | -2.32 | 9.77 | 0.350 |
| 1.23 | -4.23 | -16.28 | 11.81 | | 0.319 | -3.03 | -14.52 | 10.08 |
| 7.69 | 2.39 | -2.58 | -4.04 | | 5.14 | 3.81 | -2.57 | -3.65 |
| -7.45 | -11.54 | -1.59 | -4.60 | | -6.78 | -8.05 | -1.90 | -7.01 |
| -2.23 | 0.95 | -9.61 | -12.81 | | -0.84 | 0.99 | -4.38 | -10.84 |

**Table 4.1.5:** Comparison of accumulation errors (in mm) after 3 h for grids on the extreme western side of the domain from 3 November 2000 for the case without topography included (right) and the case with topography included (left). The scheme used for comparison was the drop-sorting scheme at the native horizontal resolution of 2.5 km.

### 4.1.6 Summary of 3 November 2000 Runs

The case on 3 November 2000 is unique because the storm caused flash flooding and high rainfall totals, along with other types of severe weather. The results of the experiments run for this date contain high magnitudes of possible errors when wind-drift adjustments are applied. Some of the results from different horizontal resolutions were also run, but not displayed or discussed. The results from all the runs accomplished for this case are summarized in Table 4.1.6. The first statistics listed 'Accum Sum' and 'Error Per Grid,' show the error resulting when the estimated accumulation error is summed for the entire domain. It is important to note that when dealing with wind-drift some of the precipitation is advected out of the domain, therefore; the sum of the accumulation errors in the domain do not equal zero as might be expected. There is also possible loss or gain of power when breaking droplets into size bins as done in the drop-sorting scheme. These errors can be particularly high for

convective cases because more precipitation is present and rainfall gradients are much stronger in convective than stratiform cases. The additional statistics listed are the maximum under- and overestimations found, along with the absolute value of these estimations. These estimations of accumulation errors increase as the horizontal resolution increases and decrease when reducing the CAPPI. The standard deviation of the possible accumulation errors is also listed and it also increases as horizontal resolution increases. Finally, the maximum rainfall total after the time period for the original, versus the adjustments, is listed to reveal the presence of a net convergence or divergence effect. As horizontal resolution increases to 0.5 km for the 3 November 2000 case, the statistics reveal some implicit convergence occurring as a result of the wind-drift scheme being applied to the original data.

| Case | Scheme | Height | Resolution | Accum Sum | Error Per Grid | Max Over | Max Under | Max Abs Val | St Dev | Max R | Max R Adjust | Difference | Div/Conv |
|---|---|---|---|---|---|---|---|---|---|---|---|---|---|
| 20001103 | BA | 1.5km | 2.5km | -685.557 | -0.339 | 8.480 | -17.026 | 17.026 | 1.939 | 69.371 | 65.334 | 4.037 | net div |
| 20001103 | BA | 1.5km | 1.5km | -867.039 | -0.428 | 14.102 | -24.349 | 24.349 | 2.917 | 69.371 | 65.700 | 3.671 | net div |
| 20001103 | BA | 1.5km | 0.5km | -904.374 | -0.447 | 41.001 | -51.996 | 51.996 | 6.865 | 69.371 | 71.736 | -2.365 | net conv |
| 20001103 | BA | 0.75km | 2.5km | -450.651 | -0.223 | 4.246 | -10.260 | 10.260 | 1.109 | 69.371 | 67.443 | 1.928 | net div |
| 20001103 | BA | 0.75km | 1.5km | -619.147 | -0.306 | 7.066 | -14.929 | 14.929 | 1.675 | 69.371 | 66.052 | 3.319 | net div |
| 20001103 | BA | 0.75km | 0.5km | -949.529 | -0.469 | 21.066 | -31.922 | 31.922 | 4.037 | 69.371 | 67.091 | 2.280 | net div |
| 20001103 | DS | 1.5km | 2.5km | -475.494 | -0.235 | 8.517 | -16.012 | 16.012 | 1.829 | 69.371 | 64.418 | 4.953 | net div |
| 20001103 | DS | 1.5km | 1.5km | -659.493 | -0.326 | 13.707 | -22.953 | 22.953 | 2.751 | 69.371 | 64.532 | 4.839 | net div |
| 20001103 | DS | 1.5km | 0.5km | -844.908 | -0.417 | 37.219 | -47.078 | 47.078 | 6.436 | 69.371 | 69.823 | -0.452 | net conv |
| 20001103 | DS | 0.75km | 2.5km | -246.780 | -0.122 | 4.600 | -9.621 | 9.621 | 1.050 | 69.371 | 66.360 | 3.011 | net div |
| 20001103 | DS | 0.75km | 1.5km | -410.384 | -0.203 | 7.209 | -14.030 | 14.030 | 1.581 | 69.371 | 65.079 | 4.292 | net div |
| 20001103 | DS | 0.75km | 0.5km | -770.810 | -0.381 | 20.096 | -30.110 | 30.110 | 3.805 | 69.371 | 65.263 | 4.108 | net div |
| 20001103 | BA-topo | 1.5km | 2.5km | -638.726 | -0.315 | 7.898 | -16.348 | 16.348 | 1.834 | 69.371 | 65.426 | 3.945 | net div |
| 20001103 | BA-topo | 1.5km | 1.5km | -816.270 | -0.403 | 13.108 | -23.410 | 23.410 | 2.758 | 69.371 | 65.454 | 3.917 | net div |
| 20001103 | BA-topo | 1.5km | 0.5km | -914.730 | -0.452 | 38.578 | -48.916 | 48.916 | 6.507 | 69.371 | 70.952 | -1.581 | net conv |
| 20001103 | DS-topo | 1.5km | 2.5km | -430.297 | -0.212 | 7.980 | -15.371 | 15.371 | 1.729 | 69.371 | 64.503 | 4.868 | net div |
| 20001103 | DS-topo | 1.5km | 1.5km | -609.047 | -0.301 | 12.793 | -22.066 | 22.066 | 2.600 | 69.371 | 64.303 | 5.068 | net div |
| 20001103 | DS-topo | 1.5km | 0.5km | -830.938 | -0.410 | 34.936 | -44.616 | 44.616 | 6.107 | 69.371 | 69.197 | 0.174 | net div |

**Table 4.1.6:** Summary of the statistics generated when applying the wind-drift schemes for multiple resolutions to the original data for the 3 November 2000 case. The units are in mm for the data displayed.

## 4.2 18 November 2000 Case

The stratiform case on 18 November 2000 (Fig. 4.2.1) was a typical light rain event over eastern New South Wales. Although the atmosphere was stable in the lowest levels, there was a warm and moist northeasterly flow in the region. The precipitation came in bands of light showers that had a fairly long duration, near 11 h overall (Sleigh, 2002). The loop of reflectivity shows little change over the 3-h period of interest. The rainfall did not appear to move toward other regions in the area given by the Cartesian grid. Accumulation amounts after the 3-h period were on the order of 20 mm. The maximum return during this time period was near 40 dBZ, which suggests there may have been areas of embedded convection (Sleigh, 2002).

When examining the images in this case, some rings of rainfall and reflectivity appear, especially in the central and eastern portions of the domain. These are a result of constructing a CAPPI height from multiple beam elevations in a light precipitation event. Each ring represents a slice of a different beam used in the construction. The beams may be undergoing sub-refraction or super-refraction and not cutting though the same elevation as determined by the beam height equation used to generate a CAPPI. The difference in intensities results as changes occur in the returns when varying the elevation.

### 4.2.1 Schemes at 1.5-km height and 2.5-km resolution

The first set of images is results from the 18 November 2000 stratiform event. They show the comparison between the original rainfall totals derived

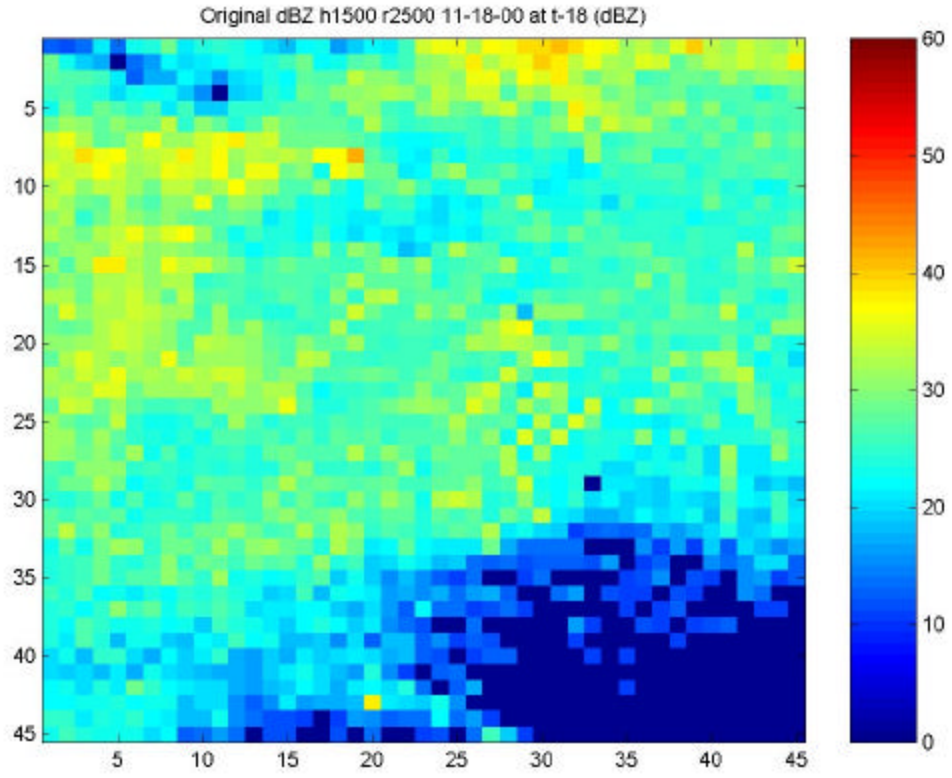


**Figure 4.2.1:** Reflectivity (in dBZ) from the stratiform case on 18 November 2000 at the final time step. The grid resolution is 2.5 km and the CAPPI height is 1.5 km. The returns do not get much over 40 dBZ in this case.

from the raw reflectivity values using the stratiform Z-R relationship given by equation 3.3.3 (Fig. 4.2.2). The accumulations are relatively low in this case with a 3-h total of only around 20 mm. The western portions of the images contain the heaviest precipitation amounts for the time period. It is in this region where the estimated error shows up the best for this typical stratiform case.

The drop-sorting scheme and bulk-advection images on the right show there is still some slight dispersion in the rainfall amounts, as evident by the western side of the region where heavier precipitation amounts are found. There

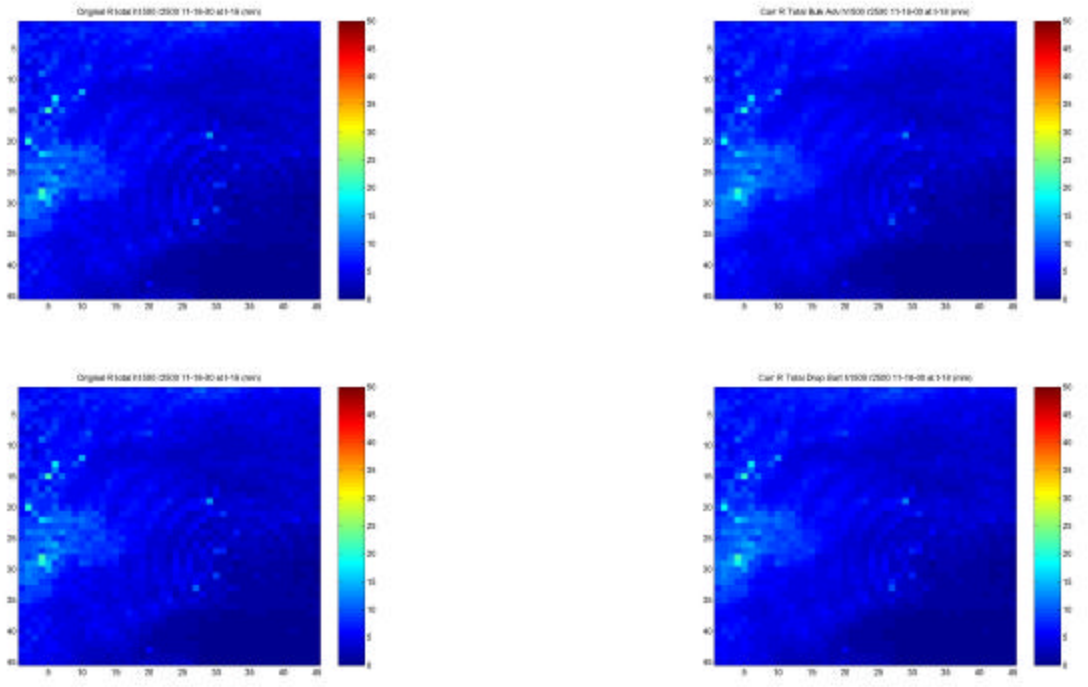

**Figure 4.2.2:** Original rainfall total after 3 h for the 18 November 2000 case (upper and lower left) with the bulk-advection scheme (upper right) and drop-sorting scheme (lower right) rainfall totals after 3 h at the native CAPPI height of 1.5 km and the native horizontal resolution of 2.5 km. The scale used is 0-50 mm.

| **Original Rainfall Total** | | | | | **BA Rainfall Total** | | | | | **DS Rainfall Total** | | | |
|---|---|---|---|---|---|---|---|---|---|---|---|---|---|
| 10.25 | 7.95 | 10.84 | 11.63 | | 10.48 | 10.18 | 11.57 | 12.14 | | 10.55 | 10.12 | 11.61 | 12.22 |
| 10.73 | 21.64 | 13.18 | 13.29 | | 13.05 | 21.06 | 13.82 | 12.53 | | 13.01 | 21.20 | 13.91 | 12.69 |
| 12.76 | 19.98 | 14.85 | 8.38 | | 13.99 | 18.68 | 14.40 | 8.65 | | 14.04 | 18.91 | 14.49 | 8.70 |
| 11.49 | 9.68 | 14.10 | 9.41 | | 11.26 | 10.62 | 13.35 | 9.08 | | 11.35 | 10.64 | 13.43 | 9.18 |
| 10.33 | 10.43 | 8.70 | 8.62 | | 10.59 | 10.21 | 8.71 | 8.11 | | 10.66 | 10.26 | 8.78 | 8.21 |
| 10.98 | 8.17 | 8.30 | 6.17 | | 10.54 | 8.44 | 8.22 | 6.20 | | 10.65 | 8.48 | 8.28 | 6.23 |
| 9.20 | 8.94 | 8.77 | 6.98 | | 9.26 | 9.11 | 8.59 | 6.79 | | 9.33 | 9.16 | 8.65 | 6.85 |

**Table 4.2.1:** Comparison of total rainfall (in mm) after 3 h for the 18 November 2000 case from a selected area that covers the grid from cell (3,27) to (6,33) for the bulk-advection (BA) scheme and drop-sorting (DS) scheme at the native CAPPI height of 1.5 km and horizontal resolution of 2.5 km.

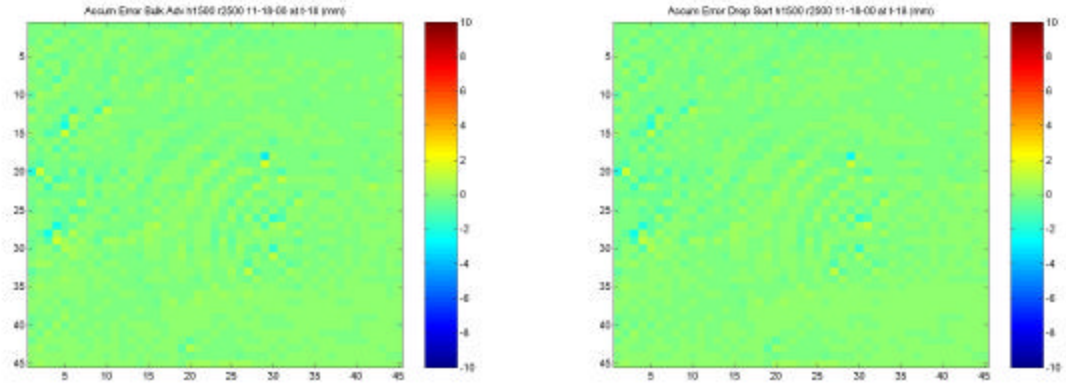

**Figure 4.2.3:** The estimated accumulation error (in mm) after 3 h for the 18 November 2000 case for the bulk-advection scheme (left) and the drop-sorting scheme (right) at the native CAPPI height of 1.5 km and the native horizontal resolution of 2.5 km.

is also a slight decrease in the rainfall amount after both schemes are applied. The drop-sorting scheme shows slightly more dispersion of the rainfall totals than the bulk-advection scheme and appears to smooth out the rainfall totals more efficiently than is given by the original rainfall totals after 3 h. A numerical comparison of the area near the heaviest precipitation amounts shows some cells contain noticeable differences between the original rainfall totals and the adjustments in the domain (Table 4.2.1).

The estimated accumulation errors for the native horizontal resolution of 2.5 km and CAPPI height of 1.5 km are compared for both schemes (Fig. 4.2.3). The errors are barely visible in the image, but the coupling of areas of underestimation and overestimation, which was evident in the convective case, also appear in both schemes for the stratiform case. There is no "storm edge" effect because the precipitation is widespread, unlike the case of convective cell patterns. There is very little difference in the accumulation of the two schemes because the rainfall amounts are just not significant over the 3-h period. The

drop-sorting scheme has a slight increase in spatial coverage of errors because of wind-drift having a larger effect on smaller droplets.

### 4.2.2 Schemes at 1.5-km height and 0.5-km resolution

The next experiment is the rainfall total comparisons between the original and the correction schemes using a hypothetical increase of horizontal resolution of 0.5 km and the native CAPPI height of 1.5 km (Fig. 4.2.4). The precipitation patterns in both schemes are less pixelated than the original rainfall total field derived from the radar's original reflectivity field. The major difference is that the drop-sorting scheme disperses the rainfall more efficiently than the bulk-advection scheme. This is evident in the northern portions of the image where the gap in rainfall is filled more in the drop-sorting scheme than in the bulk-advection scheme. The heavier rainfall amounts (near 20 mm) to the west are also dispersed more in the drop-sorting scheme than in the bulk-advection because more small drops are present in stratiform rain (Table 4.2.2).

The estimated accumulation error from the stratiform bulk-advection case at the increased horizontal resolution shows the standard coupling of over- and underestimations (Fig. 4.2.5). The scale used is still relatively low, ±10 mm over 3 h, and the errors approach the maximum error on this scale with the increased horizontal resolution in some locations. The largest areas of errors for the stratiform case are found on the western side of the image where the heaviest precipitation fell. There are regions on this figure that seem to form circular patterns of error. This ring pattern of over- and underestimation is a result of using a CAPPI. The CAPPI rings show up significantly in these images. The estimated errors on this image are under 1 cm and not as significant as the convective case on similar spatial and temporal scales.

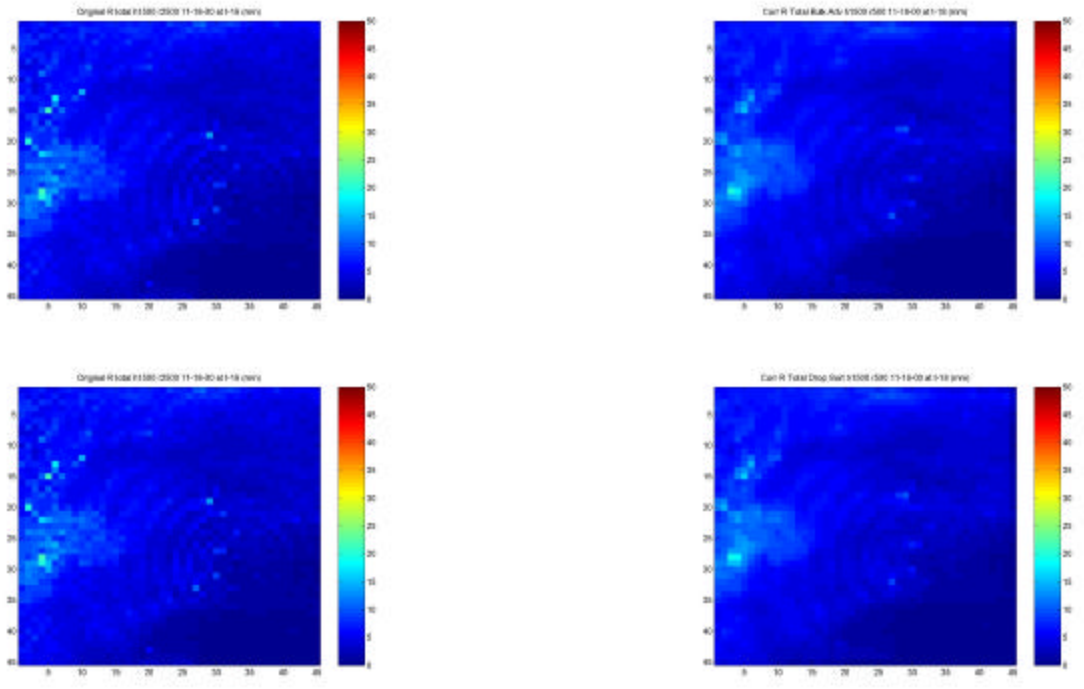

**Figure 4.2.4:** Original rainfall total after 3 h for the 18 November 2000 case (upper and lower left) with the bulk-advection scheme (upper right) and the drop-sorting scheme (lower right) rainfall totals after 3 h at the native CAPPI height of 1.5 km and the horizontal resolution increased to 0.5 km. The scale used is 0-50 mm.

| **Original Rainfall Total** | | | | | **BA Rainfall Total** | | | | | **DS Rainfall Total** | | | |
|---|---|---|---|---|---|---|---|---|---|---|---|---|---|
| 10.25 | 7.95 | 10.84 | 11.63 | | 14.25 | 13.62 | 13.29 | 11.80 | | 13.94 | 13.59 | 13.29 | 12.01 |
| 10.73 | 21.64 | 13.18 | 13.29 | | 19.61 | 17.49 | 12.74 | 10.08 | | 19.12 | 18.06 | 13.02 | 10.43 |
| 12.76 | 19.98 | 14.85 | 8.39 | | 14.84 | 15.09 | 11.45 | 8.47 | | 14.95 | 15.53 | 11.80 | 8.63 |
| 11.49 | 9.68 | 14.10 | 9.41 | | 10.38 | 11.47 | 10.24 | 7.39 | | 10.59 | 11.49 | 10.58 | 7.65 |
| 10.33 | 10.43 | 8.70 | 8.62 | | 9.94 | 8.88 | 7.77 | 5.95 | | 10.17 | 9.07 | 7.95 | 6.29 |
| 10.98 | 8.17 | 8.30 | 6.17 | | 8.78 | 8.75 | 7.27 | 5.78 | | 9.08 | 8.81 | 7.45 | 5.92 |
| 9.20 | 8.94 | 8.77 | 6.98 | | 8.42 | 8.49 | 7.24 | 5.75 | | 8.61 | 8.67 | 7.44 | 5.92 |

**Table 4.2.2:** Comparison of total rainfall (in mm) after 3 h for the 18 November 2000 case from a selected area that covers the grid from cell (3,27) to (6,33) for the bulk-advection (BA) scheme and drop-sorting (DS) scheme at the native CAPPI height of 1.5 km and increased horizontal resolution of 0.5 km.

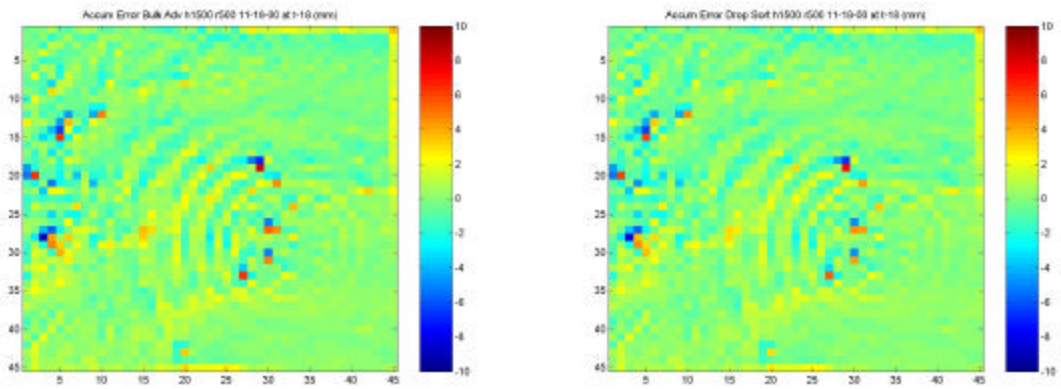

**Figure 4.2.5:** Estimated accumulation error (in mm) after 3 h for the 18 November 2000 case for the bulk-advection scheme (left) and the drop-sorting scheme (right) at the native CAPPI height of 1.5 km and the horizontal resolution increased to 0.5 km.

### 4.2.3 Schemes at 0.75-km height and 0.5-km resolution

The next set of images is from the stratiform case at the reduced CAPPI height of 0.75 km and the increased horizontal resolution of 0.5 km (Fig. 4.2.6). The comparison of original accumulated rainfall to bulk-advection scheme accumulated rainfall is similar, again, to the case in which the CAPPI height was not reduced at the higher horizontal resolution. The field of rainfall is generally less pixelated in the adjusted case than in the original. This is especially evident in the western side of the image where the more intense stratiform precipitation fell (~20 mm in 3 h). The CAPPI rings are also less evident in the adjusted image because the field is more dispersed. The intensity is approximately constant between the images.

The estimated accumulation error for the stratiform bulk-advection case at the decreased CAPPI height and increased horizontal resolution is shown in Fig. 4.2.7. The magnitude of the errors is near 5 mm after the 3-h period of interest. The

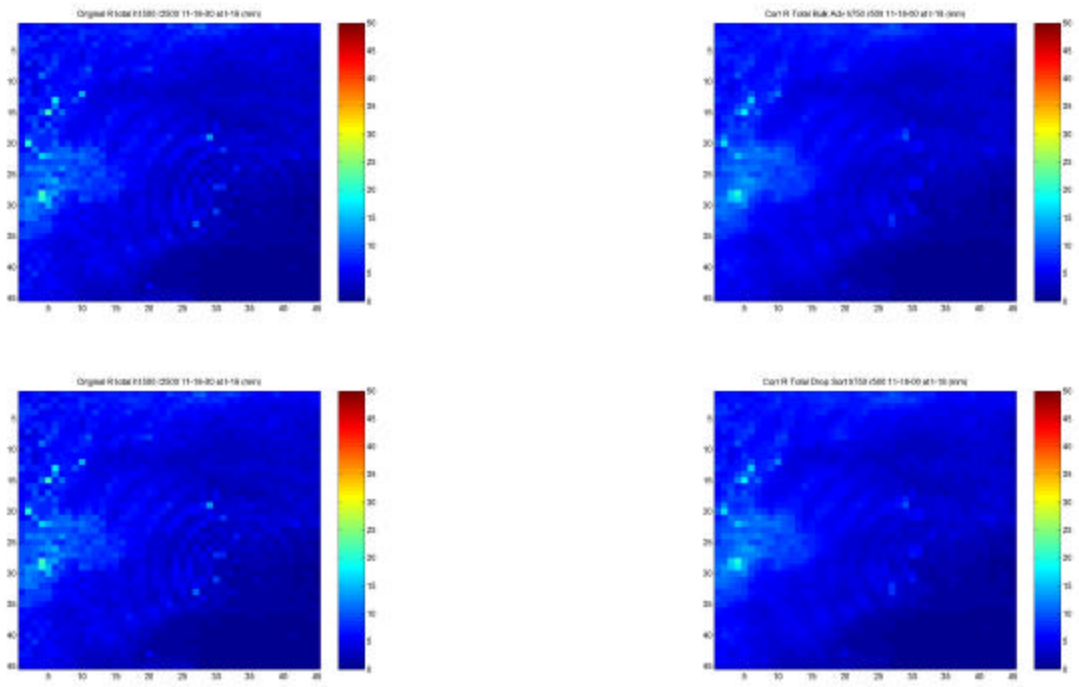

**Figure 4.2.6:** Original rainfall total after 3 h for the 18 November 2000 case (upper and lower left) with the bulk-advection scheme (upper right) and the drop-sorting scheme (lower right) rainfall totals after 3 h at the CAPPI height set to 0.75 km and the horizontal resolution increased to 0.5 km. The scale used is 0-50 mm.

| **Original Rainfall Total** | | | | | **BA Rainfall Total** | | | | | **DS Rainfall Total** | | | |
|---|---|---|---|---|---|---|---|---|---|---|---|---|---|
| 10.25 | 7.95 | 10.84 | 11.63 | | 11.41 | 12.24 | 12.42 | 12.35 | | 11.41 | 12.10 | 12.42 | 12.44 |
| 10.73 | 21.64 | 13.18 | 13.29 | | 15.81 | 19.94 | 13.95 | 11.47 | | 15.63 | 20.17 | 14.06 | 11.70 |
| 12.76 | 19.98 | 14.85 | 8.39 | | 14.94 | 16.98 | 13.43 | 8.81 | | 14.97 | 17.32 | 13.60 | 8.86 |
| 11.49 | 9.68 | 14.10 | 9.41 | | 10.92 | 11.32 | 12.17 | 8.51 | | 11.04 | 11.32 | 12.34 | 8.66 |
| 10.33 | 10.43 | 8.70 | 8.62 | | 10.63 | 9.76 | 8.54 | 7.31 | | 10.71 | 9.85 | 8.63 | 7.47 |
| 10.98 | 8.17 | 8.30 | 6.17 | | 9.86 | 8.67 | 7.97 | 6.11 | | 10.01 | 8.71 | 8.06 | 6.16 |
| 9.20 | 8.94 | 8.77 | 6.98 | | 9.05 | 9.01 | 8.20 | 6.44 | | 9.15 | 9.08 | 8.29 | 6.53 |

**Table 4.2.3:** Comparison of total rainfall (in mm) after 3 h for the 18 November 2000 case from a selected area that covers the grid from cell (3,27) to (6,33) for the bulk-advection (BA) scheme and drop-sorting (DS) scheme at the reduced CAPPI height of 0.75 km and increased horizontal resolution of 0.5 km.

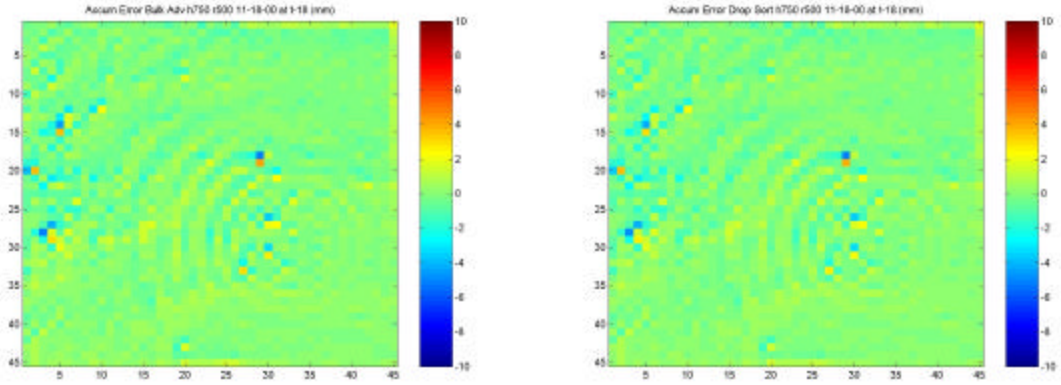

**Figure 4.2.7:** Estimated accumulation error (in mm) after 3 h for the 18 November 2000 case for the bulk-advection scheme (left) and the drop-sorting scheme (right) at the CAPPI height set to 0.75 km and the horizontal resolution increased to 0.5 km.

highest errors result from the highest returns in the image and are fairly isolated. The CAPPI rings are evident in the image below and are artificial error sources. Again, the western portions of the image are the most important to this study, as they show the higher precipitation values and greater errors (Table 4.2.3). A slight edge effect is present because some of the precipitation is being advected toward and off the edge of the domain used. This is an additional source of artificial error.

### 4.2.4 Schemes with Topography and 2.5-km resolution

The following cases are runs from the bulk-advection and drop-sorting schemes with the inclusion of topography for the stratiform case 18 November 2000. The height of the terrain is shown by Fig. 3.3.1. The results are displayed similarly to the previous cases without topography. The horizontal resolutions displayed are the native 2.5 km with an increased resolution of 0.5 km. The

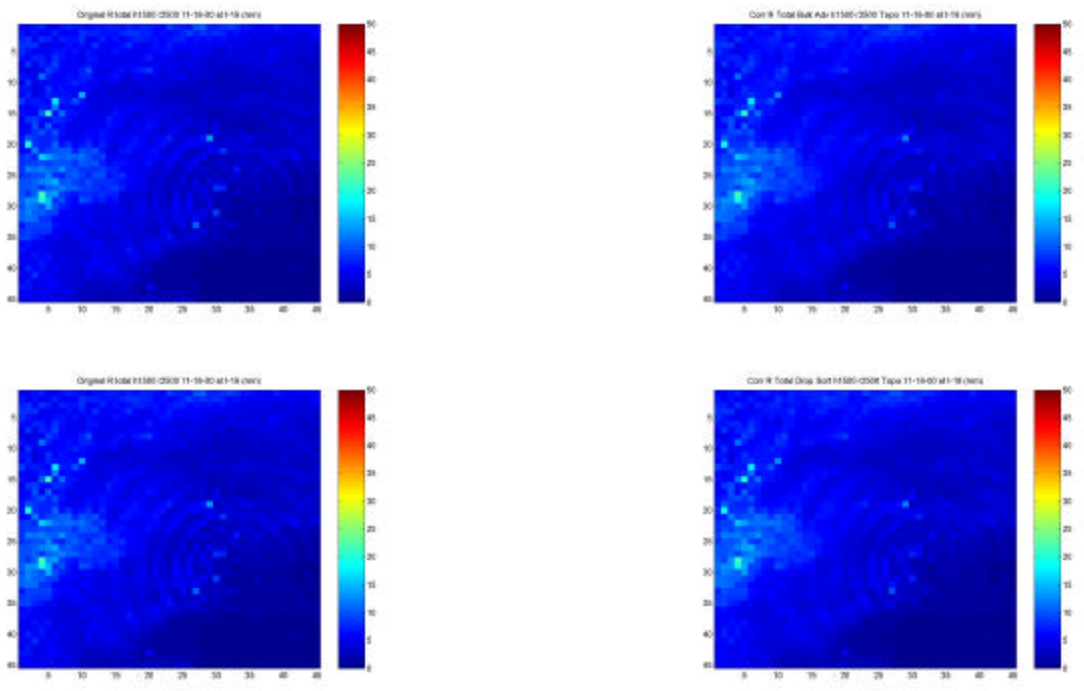

**Figure 4.2.8:** Original rainfall total after 3 h for the 18 November 2000 case (upper and lower left) with the bulk-advection scheme (upper right) and the drop-sorting scheme (lower right) rainfall totals after 3 h at the native CAPPI height of 1.5 km and the native horizontal resolution 2.5 km with topography included. The scale used is 0-50 mm.

CAPPI height remains unchanged at 1.5 km because the terrain in the west approaches or exceeds 800 m.

The first set of images (Fig. 4.2.8), shows similar results to the native resolution and CAPPI height runs for both schemes without the inclusion of topography (Fig 4.2.2). It is interesting to note that for the stratiform case, the heavier precipitation is to the west of the image. Including topography in this case should cause less of a wind-drift effect and less error. This is evident especially at the native horizontal resolution. Both schemes show similar rainfall total patterns to the original radar derived rainfall totals after 3 h. Subtle differences are only noticeable when looking at numerical results (Table 4.2.4).

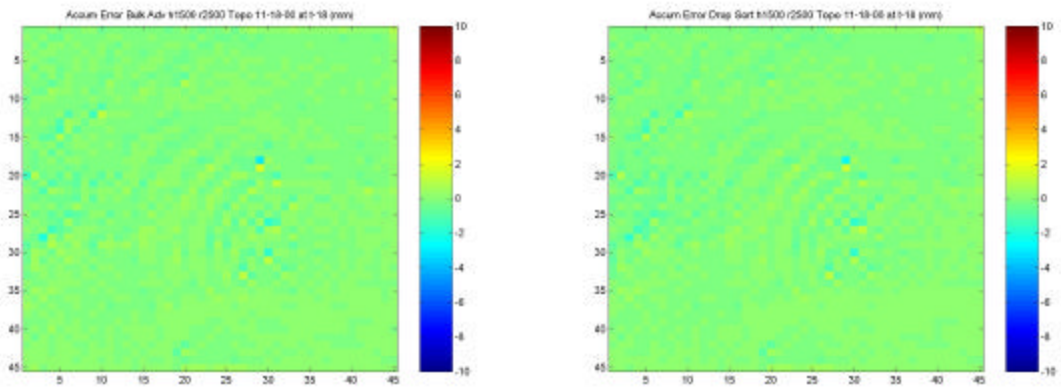

**Figure 4.2.9:** Estimated accumulation error (in mm) after 3 h for the 18 November 2000 case for the bulk-advection scheme (left) and the drop-sorting scheme (right) with topography included at the native CAPPI height of 1.5 km and the native horizontal resolution of 2.5 km.

| **Topography Not Included** | | | | | **Topography Included** | | | |
|---|---|---|---|---|---|---|---|---|
| 0.13 | -0.23 | -1.13 | -0.88 | | 0.03 | -0.12 | -0.70 | -0.67 |
| -0.38 | -0.04 | -0.20 | -0.02 | | -0.25 | -0.02 | -0.23 | -0.01 |
| -0.02 | -0.58 | 0.11 | -0.94 | | -0.06 | -0.38 | -0.01 | -0.71 |
| -0.16 | -0.51 | -0.29 | 0.02 | | -0.18 | -0.39 | -0.22 | -0.03 |
| -0.59 | -1.10 | -0.19 | -0.25 | | -0.28 | -0.64 | -0.21 | -0.10 |
| -1.94 | 1.50 | -0.55 | -0.18 | | -1.22 | 0.81 | -0.40 | -0.25 |
| -0.26 | -0.87 | 0.26 | -1.41 | | -0.06 | -0.59 | -0.01 | -1.17 |
| -0.07 | -0.01 | -1.29 | 0.14 | | 0.13 | -0.14 | -1.11 | 0.32 |

**Table 4.2.4:** Comparison of accumulation errors (in mm) after 3 h for grids on the extreme western side of the domain from 18 November 2000 for the case without topography included (right) and the case with topography included (left). The scheme used for comparison was the drop-sorting scheme at the native horizontal resolution of 2.5 km.

The estimated accumulation error (Fig. 4.2.9) between the two schemes is almost identical. The artificial error by the CAPPI rings is of similar magnitude to the actual errors found on the western side of the image (~3 mm). Overall, error is quite small because terrain is included. The error is also small because the heaviest precipitation is falling over the areas of higher terrain and this heaviest precipitation is still fairly light, yielding approximately 20 mm over the 3-h period. These errors are better examined in the western portion of the image

by looking at individual accumulation errors within adjacent grid squares for both the inclusion and exclusion of topography cases (Table 4.2.4). There is a slight reduction in accumulation error for the topography case because the wind-drift effect is less, but since the precipitation is so light the change is insignificant.

### 4.2.5 Schemes with Topography and 0.5-km resolution

The next set of images (Fig. 4.2.10) is the comparison of the original rainfall field after 3 h to the bulk-advection and drop-sorting schemes including topography at the increased horizontal resolution of 0.5 km and the CAPPI height set to 1.5 km. As shown in the case where topography is not accounted for, the precipitation pattern is less pixelated after the adjustment schemes are applied. This is more noticeable in the drop-sorting scheme, again, because the gaps of low precipitation values are decreased in the area as precipitation is advected more efficiently when compared to the bulk-advection scheme. The differences in the adjustments from the original field of precipitation occur for the most part because of the change in resolution and not because of the inclusion of topography.

The estimated accumulation errors for both schemes for the stratiform case (Fig. 4.2.11), are nearly identical to the case where topography is not included at the similar resolution (Fig. 4.2.5). The CAPPI rings show up in great detail as areas of under- and overestimation, but again this is artificial error. The actual error is primarily focused on the western portions of the image and approach values near 1 cm, which is becoming significant on the time scale given (3 h). The actual numbers for this case can be examined in Table 4.2.5.

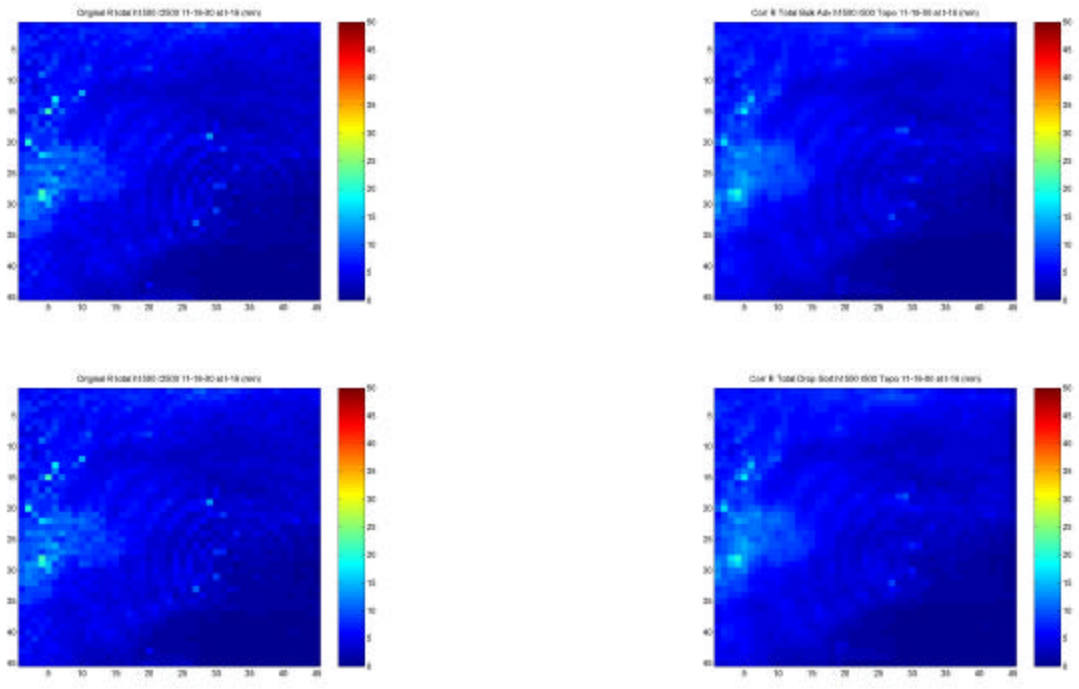

**Figure 4.2.10:** Original rainfall total after 3 h for the 18 November 2000 case (upper and lower left) with the bulk-advection scheme (upper right) and the drop-sorting scheme (lower right) rainfall totals after 3 h at the native CAPPI height of 1.5 km and the horizontal resolution increased to 0.5 km with topography included. The scale used is 0-50 mm.

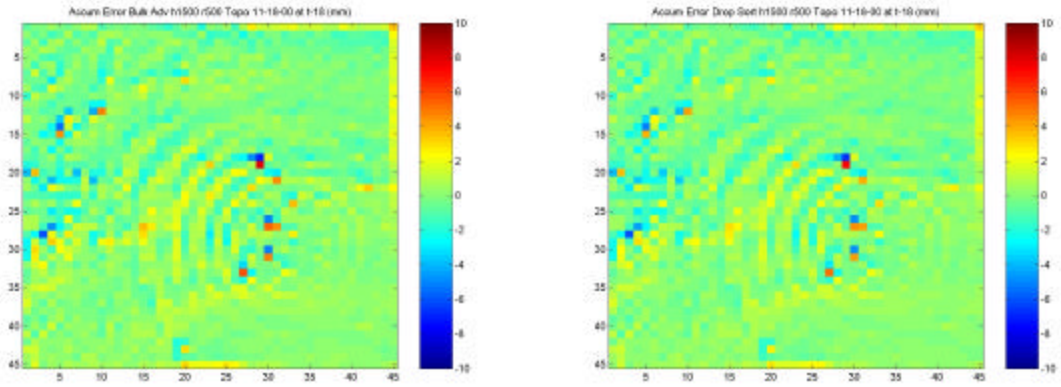

**Figure 4.2.11:** Estimated accumulation error (in mm) after 3 h for the 18 November 2000 case for the bulk-advection scheme (left) and the drop-sorting scheme (right) with topography included at the native CAPPI height of 1.5 km and the horizontal resolution increased to 0.5 km.

| Topography Not Included | | | | | Topography Included | | | |
|---|---|---|---|---|---|---|---|---|
| 0.29 | -0.95 | -3.26 | -1.67 | | 0.17 | -0.43 | -2.45 | -1.83 |
| -0.99 | 0.16 | 0.33 | -0.58 | | -0.88 | 0.18 | -0.32 | -0.24 |
| 0.02 | -1.73 | 0.43 | -2.99 | | -0.18 | -1.37 | 0.03 | -2.55 |
| -0.84 | -1.40 | -0.51 | 0.50 | | -0.73 | -1.20 | -0.62 | 0.33 |
| -4.41 | -2.07 | -0.15 | -0.81 | | -1.83 | -1.79 | -0.38 | -0.51 |
| -5.07 | 6.02 | -1.14 | -0.75 | | -3.79 | 3.47 | -1.35 | -0.82 |
| -0.94 | -2.22 | 0.02 | -4.97 | | 0.00 | -2.13 | -0.69 | -3.74 |
| -0.18 | 0.29 | -3.63 | 1.97 | | 0.49 | -0.37 | -3.04 | 1.78 |

**Table 4.2.5:** Comparison of accumulation errors (in mm) after 3 h for grids on the extreme western side of the domain from 18 November 2000 for the case without topography included (right) and the case with topography included (left). The scheme used for comparison was the drop-sorting scheme at the native horizontal resolution of 2.5 km.

### 4.2.6 Summary of 18 November 2000 Runs

The case on 18 November 2000 was a typical light rain event over NSW that lasted nearly 11 h. Most of the results from the 3-h time frame selected show that the differences between the schemes and the original rainfall amounts derived from the radar are quite small, given the light nature of the precipitation. Some of the results from different horizontal resolutions were also run, but not displayed or discussed. The results from all the runs accomplished for this case are summarized in Table 4.1.6. These 'Accum Sum' errors are smaller because the precipitation was mostly light throughout the domain. The magnitude of the estimations of accumulation error increases as the horizontal resolution increases and decreases when reducing the CAPPI. The standard deviation of the possible accumulation errors is also listed, which also increases as horizontal resolution increases, in a similar fashion as the 3 November 2000 case. There seems to be no net convergence at any resolution for this stratiform case.

| Case | Scheme | Height | Resolution | Accum Sum | Error per grid | Max Over | Max Under | Max Abs Val | St Dev | Max R | Max R Corr | Difference | Div/Conv |
|---|---|---|---|---|---|---|---|---|---|---|---|---|---|
| 20001118 | BA | 1.5km | 2.5km | -106.327 | -0.053 | 1.752 | -2.885 | 2.885 | 0.302 | 21.672 | 21.063 | 0.609 | net div |
| 20001118 | BA | 1.5km | 1.5km | -128.151 | -0.063 | 2.894 | -4.117 | 4.117 | 0.468 | 21.672 | 20.594 | 1.078 | net div |
| 20001118 | BA | 1.5km | 0.5km | 65.998 | 0.033 | 8.198 | -8.888 | 8.888 | 1.132 | 21.672 | 19.613 | 2.059 | net div |
| 20001118 | BA | 0.75km | 2.5km | -69.551 | -0.034 | 0.882 | -1.687 | 1.687 | 0.162 | 21.672 | 21.374 | 0.298 | net div |
| 20001118 | BA | 0.75km | 1.5km | -95.973 | -0.047 | 1.463 | -2.519 | 2.519 | 0.257 | 21.672 | 21.171 | 0.501 | net div |
| 20001118 | BA | 0.75km | 0.5km | -120.421 | -0.059 | 4.291 | -5.275 | 5.275 | 0.655 | 21.672 | 19.937 | 1.735 | net div |
| 20001118 | DS | 1.5km | 2.5km | -125.921 | -0.062 | 1.498 | -2.741 | 2.741 | 0.285 | 21.672 | 21.195 | 0.477 | net div |
| 20001118 | DS | 1.5km | 1.5km | -151.271 | -0.075 | 2.553 | -3.928 | 3.928 | 0.440 | 21.672 | 20.765 | 0.907 | net div |
| 20001118 | DS | 1.5km | 0.5km | -16.911 | -0.008 | 7.334 | -8.396 | 8.396 | 1.048 | 21.672 | 19.121 | 2.551 | net div |
| 20001118 | DS | 0.75km | 2.5km | -88.405 | -0.044 | 0.784 | -1.594 | 1.594 | 0.155 | 21.672 | 21.482 | 0.190 | net div |
| 20001118 | DS | 0.75km | 1.5km | -115.518 | -0.057 | 1.263 | -2.390 | 2.390 | 0.243 | 21.672 | 21.294 | 0.378 | net div |
| 20001118 | DS | 0.75km | 0.5km | -151.606 | -0.075 | 3.844 | -5.051 | 5.051 | 0.614 | 21.672 | 20.166 | 1.506 | net div |
| 20001118 | BA-topo | 1.5km | 2.5km | -101.872 | -0.050 | 1.708 | -2.844 | 2.844 | 0.268 | 21.672 | 21.313 | 0.359 | net div |
| 20001118 | BA-topo | 1.5km | 1.5km | -129.246 | -0.064 | 2.825 | -4.066 | 4.066 | 0.418 | 21.672 | 21.066 | 0.606 | net div |
| 20001118 | BA-topo | 1.5km | 0.5km | -2.063 | -0.001 | 8.093 | -7.061 | 8.093 | 1.034 | 21.672 | 19.638 | 2.034 | net div |
| 20001118 | DS-topo | 1.5km | 2.5km | -120.935 | -0.060 | 1.452 | -2.701 | 2.701 | 0.253 | 21.672 | 21.426 | 0.246 | net div |
| 20001118 | DS-topo | 1.5km | 1.5km | -150.743 | -0.074 | 2.489 | -3.877 | 3.877 | 0.392 | 21.672 | 21.199 | 0.473 | net div |
| 20001118 | DS-topo | 1.5km | 0.5km | -73.723 | -0.036 | 7.226 | -6.747 | 7.226 | 0.954 | 21.672 | 19.895 | 1.777 | net div |

**Table 4.2.6:** Summary of the statistics generated when applying the wind-drift schemes for multiple resolutions to the original data for the 18 November 2000 case. The units are in mm for the data displayed.

## 4.3 26 September 2000 Case

An additional case used in this study was another convective event from 26 September 2000. This case study was run only with the bulk-advection scheme to briefly look at the associated errors. The differences in error between the bulk-advection and drop-sorting schemes were generally insignificant, so the bulk-advection scheme was used in the interest of computational efficiency. The errors were compiled similarly to the primary cases and the images are displayed in this section in a similar fashion. The major difference in this case was the time duration used. It was 20 min shorter than the primary events used.

The synoptic environment over the region was characterized by a relatively stable atmosphere as a trough approached the region from central Australia. In the beginning stages of the images, a sea breeze front can be located by weak returns near the coast. This most likely added to the enhancement of convection over the domain although the atmosphere was relatively stable. The first storm cells approached the region rather rapidly from what appeared to be two distinct linear echoes from both the northwest and the southwest. Towards the end of the time period examined in this case, the storm cells seemed to begin to merge near the area where the CPOL was located (Fig. 4.3.1) and eventually resulted in an intense bow echo until the southern flank of the storm dissipated.

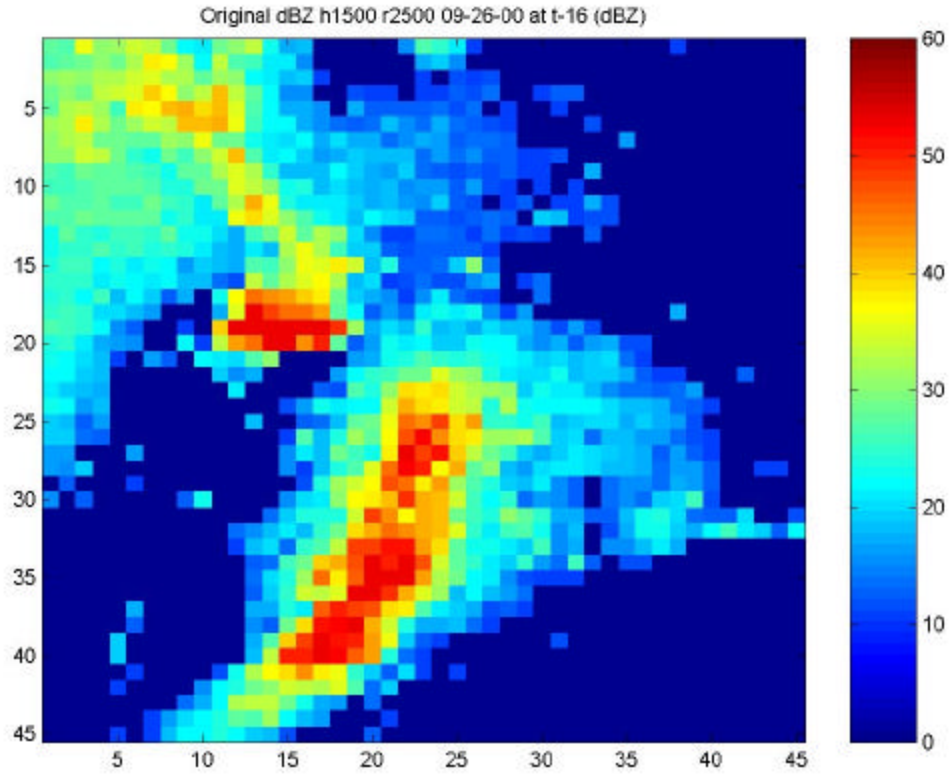


**Figure 4.3.1:** Reflectivity (in dBZ) at the final time step used for an additional convective case on 26 September 2000. The grid resolution is 2.5 km and the CAPPI height is 1.5 km.

### 4.3.1 Bulk-advection at 1.5-km height and 2.5-km resolution

The first set of images is the comparison of the rainfall fields after 160 min for the 26 September 2000 convective case. The bulk-advection scheme with the convective Z-R relationship was used with the native CAPPI height of 1.5 km and the native horizontal resolution of 2.5 km (Fig. 4.3.2). Since the storms appeared relatively late in the time period used and they moved rather quickly, the precipitation amounts are relatively low for the time frame. The most intense precipitation given by the original reflectivity field and the convective Z-R relationship is approximately 33 mm for the 160 min loop. After the bulk

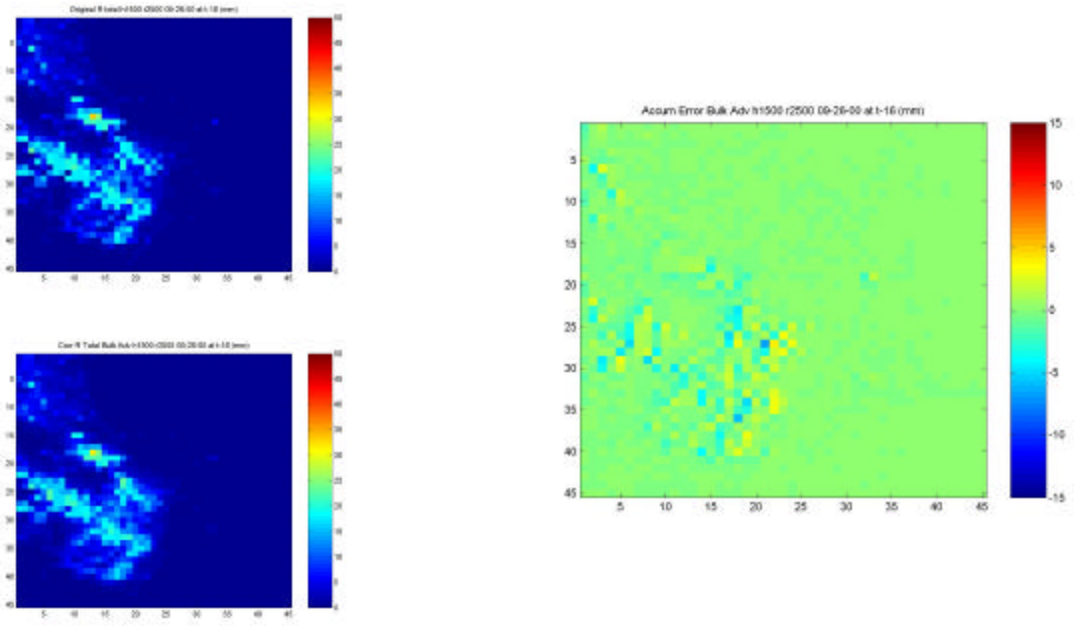

**Figure 4.3.2:** Original rainfall total after 160 min for the September 26th, 2000 case (upper left) with the bulk-advection scheme (lower left) rainfall total after 160 min at the native CAPPI height of 1.5 km and the native horizontal resolution of 2.5 km, along with the estimated accumulation error (right). The scale used for the rainfall totals is 0-50 mm, while the estimated accumulation error is ±15 mm.

| **Original Rainfall Total** | | | | | **BA Rainfall Total** | | | |
|---|---|---|---|---|---|---|---|---|
| 3.22 | 1.91 | 1.26 | 1.29 | | 3.25 | 1.94 | 1.22 | 1.24 |
| 13.56 | 14.93 | 15.08 | 4.06 | | 13.00 | 14.28 | 14.16 | 5.54 |
| 18.95 | 33.15 | 25.55 | 6.33 | | 18.19 | 31.93 | 24.51 | 9.66 |
| 20.71 | 21.45 | 20.51 | 19.53 | | 21.52 | 22.59 | 22.09 | 19.32 |
| 6.92 | 6.05 | 18.29 | 20.40 | | 7.50 | 6.57 | 17.61 | 19.78 |
| 1.61 | 0.88 | 6.78 | 0.29 | | 1.94 | 1.72 | 8.05 | 1.65 |
| 0.70 | 0.70 | 0.90 | 0.23 | | 0.65 | 0.71 | 0.94 | 0.29 |

**Table 4.3.1:** Comparison of total rainfall (in mm) after 160 min for the September 26th, 2000 case from a selected area that covers the grid from cell (12,16) to (15,22) for the bulk-advection (BA) scheme at the native CAPPI height of 1.5 km and horizontal resolution of 2.5 km.

advection scheme was applied some regions, especially to the south of the CPOL location, are less pixelated when compared to the original field. The estimated accumulation errors show less of a coupling pattern than the primary cases used, but there are some existing regions where the coupling of over- and

underestimation is found. The maximum magnitude of error is approximately 7 mm and occurs near the center of the image. Some of the numerical differences in rainfall totals over the time frame near the center of the domain are also shown (Table 4.3.1).

### 4.3.2 Bulk-advection at 1.5-km height and 0.5-km resolution

The images in this section are the results for the increase of horizontal resolution to 0.5 km, while keeping the CAPPI height at the native 1.5 km (Fig. 4.3.3). As was seen in the primary cases, increasing the horizontal resolution while using a constant altitude plot increases the estimated accumulation error significantly. The estimated accumulation error in this case reaches a magnitude of 16 mm over the 160 min duration. Although the system is rapidly pushing though the domain, these possible errors become quite significant. The rainfall total image after the correction is applied has a lot less pixelation than the previous wind-drift adjustment and the rainfall totals derived from the original reflectivity field smoothed to eliminate possible hail contamination. Again, some of the differences in rainfall total are shown numerically for an area near the center of the domain (Table. 4.3.2).

### 4.3.3 Bulk-advection at 0.75-km height and 2.5-km resolution

The next set of results deals with the native horizontal resolution of 2.5 km, but a decrease in the CAPPI height to 0.75 km (Fig. 4.3.4). As with previous trials, reducing the CAPPI height reduces the effect of wind-drift because the

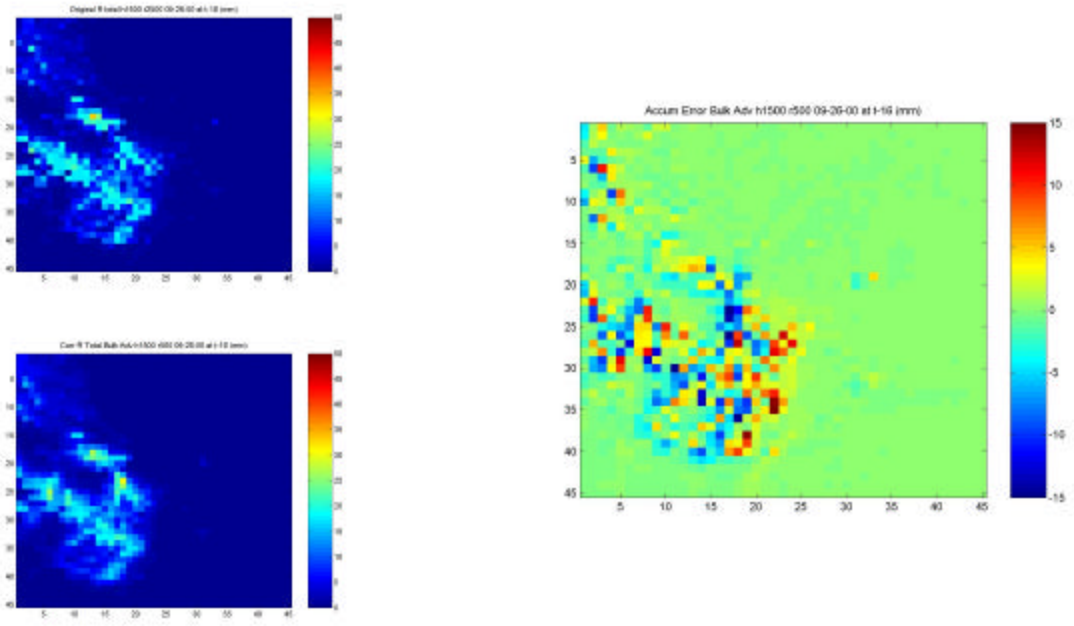

**Figure 4.3.3:** Original rainfall total after 160 min for the 26 September 2000 case (upper left) with the bulk-advection scheme (lower left) rainfall total after 160 min at the native CAPPI height of 1.5 km and the horizontal resolution increased to 0.5 km, along with the estimated accumulation error (right). The scale used for the rainfall totals is 0-50 mm, while the estimated accumulation error is ±15 mm.

| **Original Rainfall Total** | | | | | **BA Rainfall Total** | | | |
|---|---|---|---|---|---|---|---|---|
| 3.22 | 1.91 | 1.26 | 1.29 | | 3.15 | 1.99 | 1.11 | 1.04 |
| 13.56 | 14.93 | 15.08 | 4.06 | | 11.06 | 11.88 | 10.88 | 7.82 |
| 18.95 | 33.15 | 25.55 | 6.33 | | 15.14 | 27.27 | 20.83 | 15.67 |
| 20.71 | 21.45 | 20.51 | 19.53 | | 21.06 | 23.65 | 22.58 | 21.22 |
| 6.92 | 6.05 | 18.29 | 20.40 | | 8.99 | 8.18 | 14.80 | 17.18 |
| 1.61 | 0.88 | 6.78 | 0.29 | | 2.31 | 3.91 | 10.05 | 4.63 |
| 0.70 | 0.70 | 0.90 | 0.23 | | 0.48 | 0.73 | 0.96 | 0.50 |

**Table 4.3.2:** Comparison of total rainfall (in mm) after 160 min for the 26 September 2000 case from a selected area that covers the grid from cell (12,16) to (15,22) for the bulk-advection (BA) scheme at the native CAPPI height of 1.5 km and increased horizontal resolution of 0.5 km.

precipitation has a smaller vertical distance to fall. It is interesting to note that in this convective case the error and rainfall fields resemble that of the case where both the native CAPPI height and horizontal resolution were used. This is noticeable by comparing the images of the accumulation error and the corrected

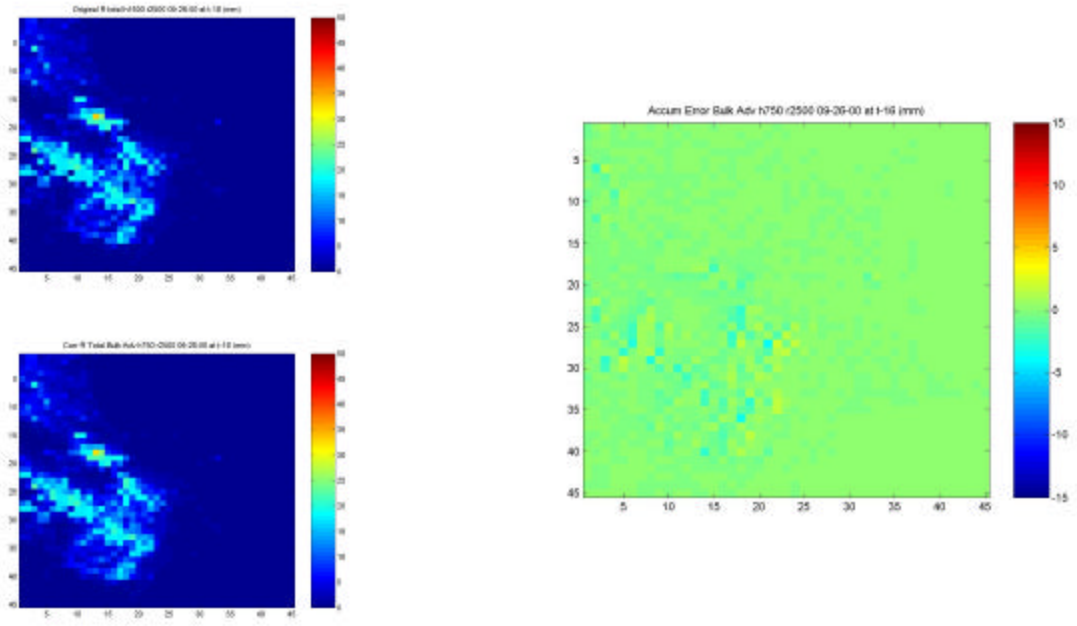

**Figure 4.3.4:** Original rainfall total after 160 min for the 26 September 2000 case (upper left) with the bulk-advection scheme (lower left) rainfall total after 160 min at the reduced CAPPI height of 0.75 km and the native horizontal resolution of 2.5 km, along with the estimated accumulation error (right). The scale used for the rainfall totals is 0-50 mm, while the estimated accumulation error is ±15 mm.

| **Original Rainfall Total** | | | | | **BA Rainfall Total** | | | |
|---|---|---|---|---|---|---|---|---|
| 3.22 | 1.91 | 1.26 | 1.29 | | 3.24 | 1.92 | 1.24 | 1.27 |
| 13.56 | 14.93 | 15.08 | 4.06 | | 13.30 | 14.60 | 14.62 | 4.93 |
| 18.95 | 33.15 | 25.55 | 6.33 | | 18.57 | 32.54 | 25.02 | 8.31 |
| 20.71 | 21.45 | 20.51 | 19.53 | | 21.31 | 22.18 | 21.57 | 19.36 |
| 6.92 | 6.05 | 18.29 | 20.40 | | 7.22 | 6.32 | 17.96 | 20.09 |
| 1.61 | 0.88 | 6.78 | 0.29 | | 1.80 | 1.34 | 7.54 | 1.11 |
| 0.70 | 0.70 | 0.90 | 0.23 | | 0.68 | 0.70 | 0.93 | 0.26 |

**Table 4.3.3:** Comparison of total rainfall (in mm) after 160 min for the 26 September 2000 case from a selected area that covers the grid from cell (12,16) to (15,22) for the bulk-advection (BA) scheme at the reduced CAPPI height of 0.75 km and native horizontal resolution of 2.5 km.

rainfall fields for both cases at the last time step. The maximum magnitude of the accumulation error in this case was approximately 4 mm, which is somewhat smaller than the native CAPPI height and horizontal resolution case. The effect

of lowering the CAPPI height therefore effectively reduces the wind-drift effect for most regions. Some of the numerical comparisons near the center of the domain for this case are also shown (Table 4.3.3).

### 4.3.4 Bulk-advection at 1.5-km height and 0.5-km resolution

The CAPPI height remains at the lowered 0.75 km while the horizontal resolution is once again increased to 0.5 km for the next set of images (Fig. 4.3.5). Once again the trends hold true from the primary cases, where the magnitude of the errors falls between the native resolution and CAPPI height error and the increased horizontal resolution with the native CAPPI. The images of the rainfall totals for the last time step are smoothed once again in the bulk-advection adjustments. The maximum magnitude of accumulation error was near the CPOL and had a value of approximately 13 mm at the last time step. A numerical comparison from a selected area near the center of the domain is also available (Table 4.3.4).

### 4.3.5 Bulk-advection with Topography

The final two sets of images (Fig. 4.3.6 and Fig. 4.3.7) are the cases that include topography while applying the bulk-advection scheme at different horizontal resolutions and the native CAPPI height of 1.5 km. When examining the wind-drift adjusted rainfall totals at the last time step to the original rainfall fields, similarities can be seen in the western regions where the height the precipitation has to fall is decreased. However, as the echoes approach the radar

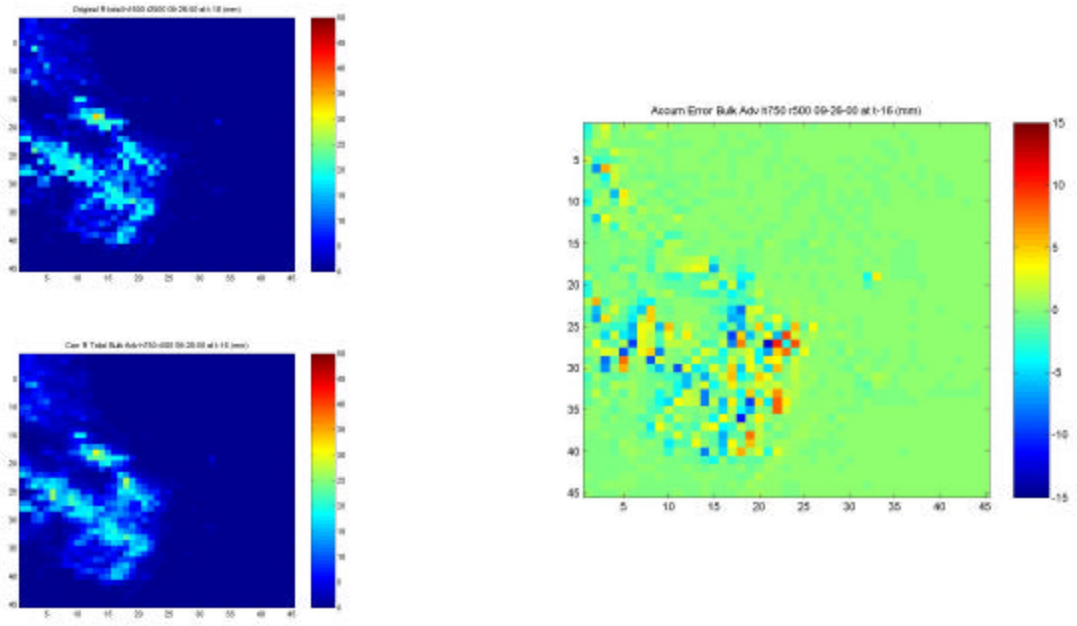

**Figure 4.3.5:** Original rainfall total after 160 min for the 26 September 2000 case (upper left) with the bulk-advection scheme (lower left) rainfall total after 160 min at the reduced CAPPI height of 0.75 km and the horizontal resolution increased to 0.5 km, along with the accumulation error (right). The scale used for the rainfall totals is 0-50 mm, while the estimated accumulation error is ±15 mm.

| **Original Rainfall Total** | | | | | **BA Rainfall Total** | | | |
|---|---|---|---|---|---|---|---|---|
| 3.22 | 1.91 | 1.26 | 1.29 | | 3.24 | 1.97 | 1.18 | 1.16 |
| 13.56 | 14.93 | 15.08 | 4.06 | | 12.26 | 13.34 | 12.85 | 6.78 |
| 18.95 | 33.15 | 25.55 | 6.33 | | 17.04 | 30.13 | 23.04 | 12.60 |
| 20.71 | 21.45 | 20.51 | 19.53 | | 21.64 | 23.31 | 22.79 | 19.64 |
| 6.92 | 6.05 | 18.29 | 20.40 | | 8.18 | 7.25 | 16.56 | 18.86 |
| 1.61 | 0.88 | 6.78 | 0.29 | | 2.17 | 2.67 | 9.11 | 2.92 |
| 0.70 | 0.70 | 0.90 | 0.23 | | 0.59 | 0.72 | 0.94 | 0.38 |

**Table 4.3.4:** Comparison of total rainfall (in mm) after 160 min for the 26 September 2000 case from a selected area that covers the grid from cell (12,16) to (15,22) for the bulk-advection (BA) scheme at the reduced CAPPI height of 0.75 km and increased horizontal resolution of 0.5 km.

and intensify, the errors resemble the respective horizontal resolution adjustments that appeared previously. The maximum magnitude of the accumulation error for the native and increased horizontal resolution with

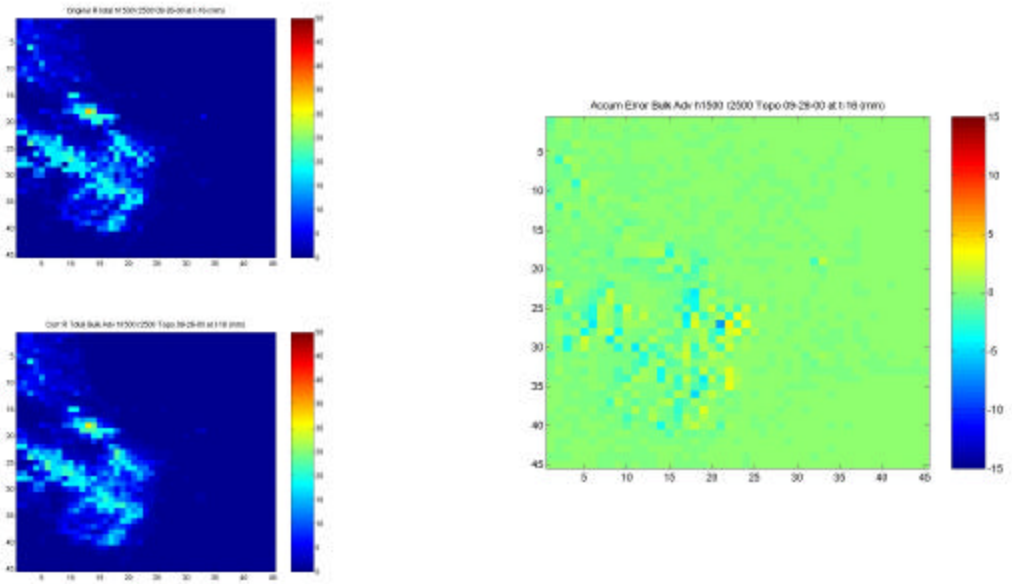

**Figure 4.3.6:** Original rainfall total after 160 min for the 26 September 2000 case (upper left) with the bulk-advection scheme (lower left) rainfall total at the native CAPPI height of 1.5 km and the native horizontal resolution of 2.5 km with topography included, along with the estimated accumulation error (right). The scale used for the rainfall totals is 0-50 mm, while the estimated accumulation error is ±15 mm.

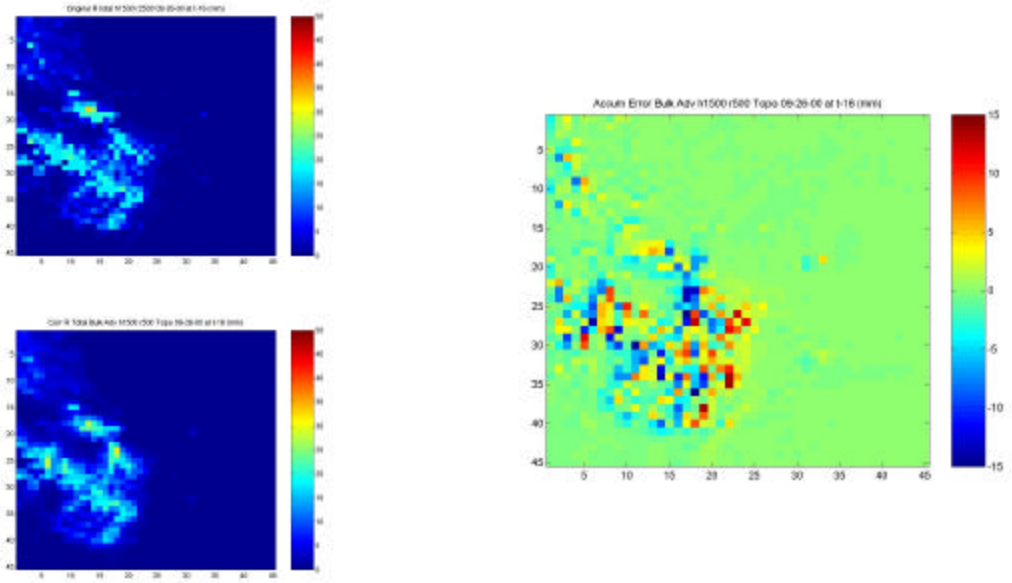

**Figure 4.3.7:** Original rainfall total after 160 min for the 26 September 2000 case (upper left) with the bulk-advection scheme (lower left) rainfall total at the native CAPPI height of 1.5 km and the horizontal resolution increased to 0.5 km with topography included, along with the estimated accumulation error (right). The scale used for the rainfall totals is 0-50 mm, while the estimated accumulation error is ±15 mm.

topography is approximately 7 mm and 16 mm, respectively, which is nearly the same as the cases not including topography, this implies the highest error is occurring away from the mountainous western region where elevations reach near or exceed 800 meters.

### 4.3.6 Summary of 26 September 2000 Runs

The 26 September 2000 case is an additional case to further illustrate the effects of wind-drift. This case offers a look at the resulting differences from applying the wind-drift scheme on ordinary convective cells of a non-supercellular nature. This implies that the environmental shear is most likely weaker in the directional sense, allowing for precipitation to be advected along the storm track, thus reducing the estimated accumulation error. A summary of selected statistics is shown in Table 4.3.5. It is interesting to note that the 'Accum Sum' for this event is a lot lower than the severe convective case from 3 November 2000. This is due to the bulk of precipitation occurring near the center of the domain for the time period selected in this experiment, thus; there is less advection of rain out of the domain. The largest difference occurs when using the hypothetical increase of horizontal resolution to 0.5 km and including topography, which is around 16 mm. It is also interesting to note that the maximum estimated error does not coincide with the maximum adjusted rainfall total over the 160 min time frame. Unlike the severe convective case, there is no net convergence in the maximum rainfall total when increasing the horizontal resolution.

| Case | Scheme | Height | Resolution | Accum Sum | Error per grid | Max Over | Max Under | Max Abs Val | St Dev | Max R | Max R Corr | Difference | Div/Conv |
|---|---|---|---|---|---|---|---|---|---|---|---|---|---|
| 20000926 | BA | 1.5km | 2.5km | -156.770 | -0.077 | 3.878 | -6.690 | 6.690 | 0.749 | 33.153 | 31.927 | 1.226 | net div |
| 20000926 | BA | 1.5km | 0.5km | -143.136 | -0.071 | 14.818 | -15.745 | 15.745 | 2.505 | 33.153 | 30.233 | 2.920 | net div |
| 20000926 | BA | 0.75km | 2.5km | -102.547 | -0.051 | 1.933 | -3.937 | 3.937 | 0.414 | 33.153 | 32.537 | 0.616 | net div |
| 20000926 | BA | 0.75km | 0.5km | -190.698 | -0.094 | 10.045 | -12.703 | 12.703 | 1.611 | 33.153 | 30.132 | 3.021 | net div |
| 20000926 | BA-topo | 1.5km | 2.5km | -146.474 | -0.072 | 3.875 | -6.677 | 6.677 | 0.678 | 33.153 | 31.979 | 1.174 | net div |
| 20000926 | BA-topo | 1.5km | 0.5km | -164.488 | -0.081 | 13.930 | -16.039 | 16.039 | 2.358 | 33.153 | 31.315 | 1.838 | net div |

**Table 4.3.5:** Summary of the statistics generated when applying the wind-drift schemes for multiple resolutions to the original data for the 26 September 2000 case. The units are in mm for the data displayed.

## 4.4 Beam Elevation Option

Inside the architecture of both the bulk-advection and drop-sorting schemes resides an option to use beam elevation on a Cartesian grid of reflectivity instead of constant altitude plots. When using the schemes to simulate beam elevation it is important to note that the data used comes from Cartesian grids at constant elevations of both wind and reflectivity. To accurately use the wind-drift schemes, the wind components would have to be at the same altitude along the beam. This is not the case, but running the cases with beam elevation schemes illustrates the importance of range (away) from the radar regardless of the accuracy of the measured wind field. It is also important to note that the refractive index of the atmosphere depends on pressure, temperature, and vapor pressure. Changes in the refractive index due to changes in atmospheric conditions can cause the beam to bend toward the ground or more toward space.

The equation used to find the beam height in the scheme, assuming standard refraction, is given by 4.4.1, where $r$ is the range of the radar to the center of a grid square, $f$ is the beam elevation angle, $H_0$ is the height of the radar above the ground, and $R' = \frac{4}{3}R$ (where $R$ is the radius of the earth approximated by 6374 km) (Rinehart, 1997).

$$H = \sqrt{r^2 + R'^2 + 2rR'\sin f} - R' + H_0 \qquad (4.4.1)$$

For each case examined the height of the beam is shown as part of each figure for a quick reference on the effect of beam elevation with range. As noted by Rinehart (1997), the actual radius of the earth depends upon latitude as the earth

is not a perfect sphere, but the equation above is sufficient for most radar applications.

The following results are from the convective case on 3 November 2000 using the drop-sorting scheme with different beam elevations; the stratiform case was ignored since the rainfall accumulation and associated error were small in previous experiments. Only two low beam elevations, 0.5° and 1.5°, are considered since most rainfall estimations are derived from the lowest beam elevations. The lowest beam elevation in other locations is a function of the nearby topography, however. Two horizontal resolutions were also used, including the native resolution of 2.5 km and an increased resolution of 0.5 km. In the final case, topography was also included with the beam elevation solution for completeness.

### 4.4.1 Beam Elevation of 0.5° and 2.5-km resolution

The first set of images is the convective case at the standard horizontal resolution of 2.5 km and the beam elevation of 0.5° (Fig. 4.4.1). Since the domain is only a 45x45x2.5 km Cartesian grid, the maximum range from the radar given by the horizontal resolution used is approximately 80 km. This yields a maximum beam height of less than 1 km on even the most extreme edges of the image. Between the original rainfall total and the drop-sorting scheme adjusted rainfall total there is very little difference. These small differences are evident on the accumulation error images where the maximum magnitude error is approximately 4 mm over the 3-h period. It is also interesting to note that as the rainfall approaches the radar the error falls off because the effect of wind-drift is reduced due to the lower beam height.

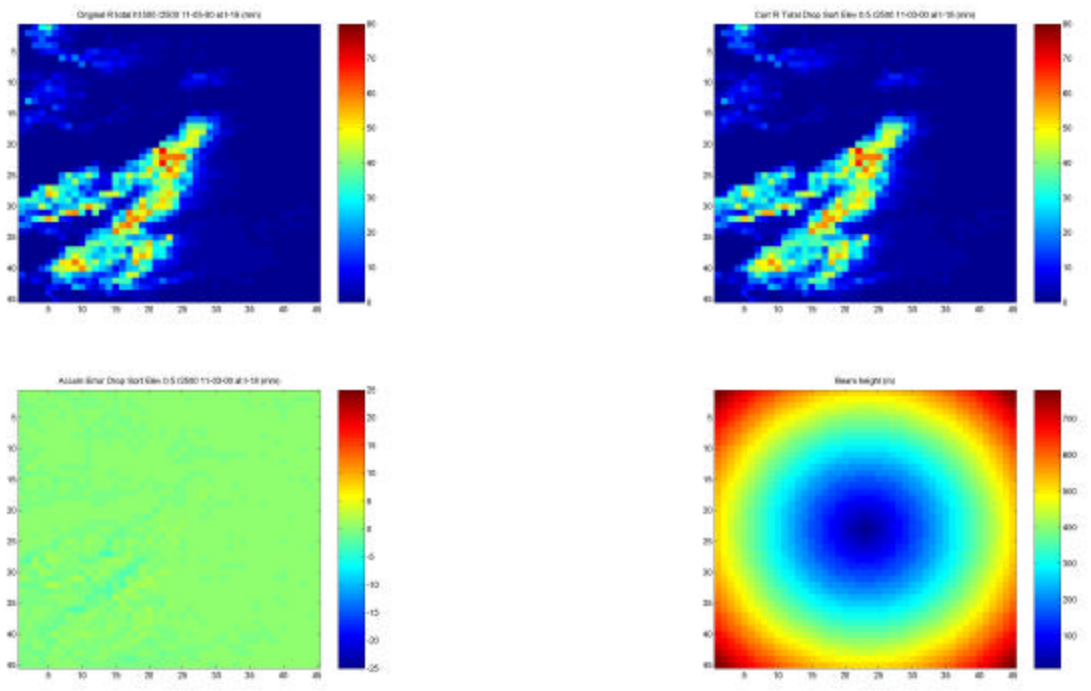

**Figure 4.4.1:** Original rainfall total after 3 h for the 3 November 2000 case (upper left (0-80 mm)) with the drop-sorting scheme (upper right) rainfall total after 3 h using a beam elevation of 0.5° (beam height lower right (0-800 m)) and the native horizontal resolution of 2.5 km. The estimated accumulation error over this period for these options is also shown using a scale of ±25 mm (lower left).

### 4.4.2 Beam Elevation of 0.5° and 0.5-km resolution

The second set of images improves the horizontal resolution to 0.5 km while still using the 0.5° beam elevation (Fig. 4.4.2). The increase of the horizontal resolution decreases the maximum range in the given domain. This reduction in range leads to the reduction of the maximum beam elevation in the corners and the edges of the image. In the cases where beam elevations were not used, increasing the horizontal resolution caused the errors to increase. In this case, using a low beam elevation and an increased horizontal resolution keeps the error about the same (~4 mm over 3 h) as in the case of the native horizontal

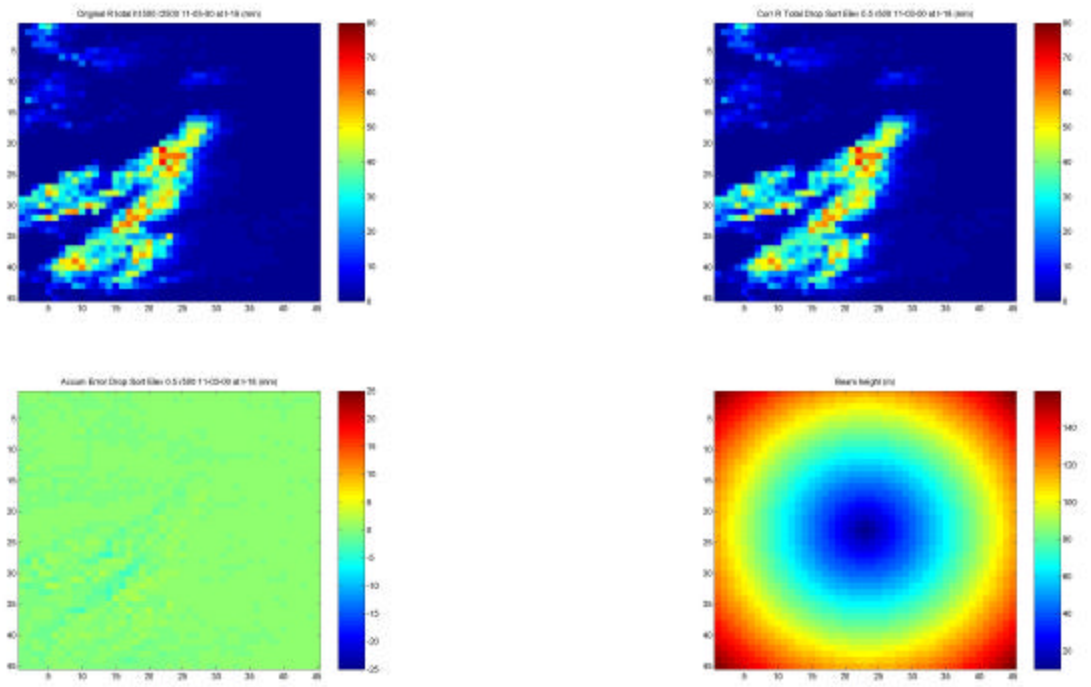

**Figure 4.4.2:** Original rainfall total after 3 h for the 3 November 2000 case (upper left (0-80 mm)) with the drop-sorting scheme (upper right) rainfall total after 3 h using a beam elevation of 0.5° (beam height lower right (0-160 m)) and the horizontal resolution increased to 0.5 km. The accumulation error over this period for these options is also shown using a scale of ±25 mm (lower left).

resolution of 2.5 km. Again, it shows that the errors diminish near the location of the radar near the center of the image.

### 4.4.3 Beam Elevation of 1.5° and 2.5-km resolution

The next set of images increases the beam elevation to 1.5° while keeping the native horizontal resolution of 2.5 km (Fig. 4.4.3). Raising the beam elevation does two things in this case; it shows what happens when the topography forces the raising of the lowest beam elevation and it simulates what happens at longer

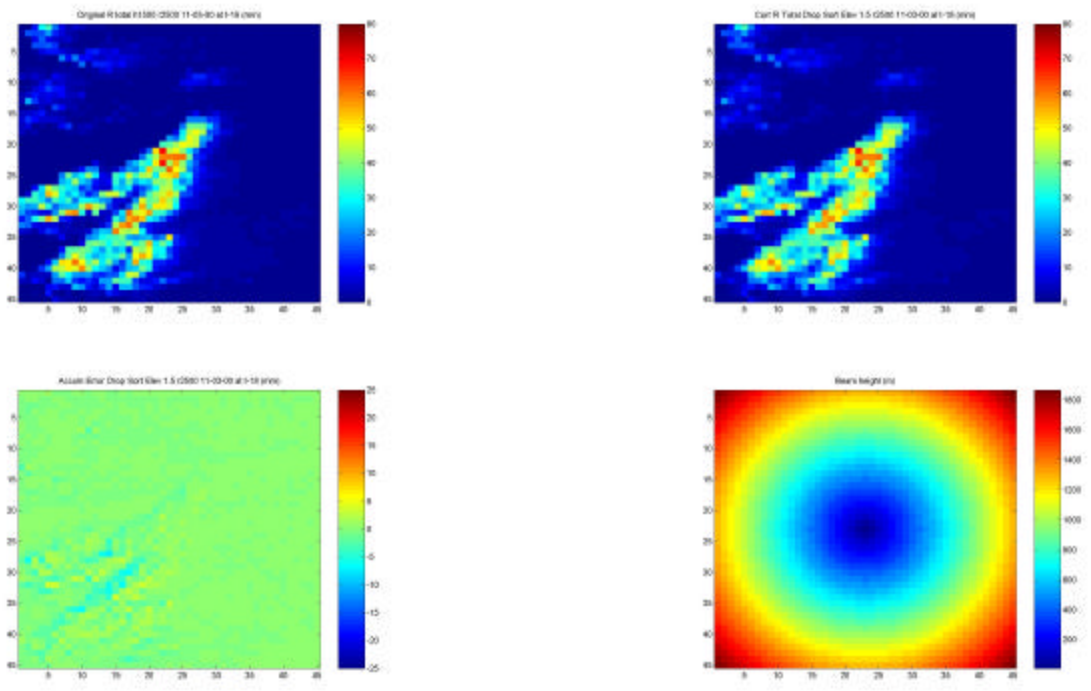

**Figure 4.4.3:** Original rainfall total after 3 h for the 3 November 2000 case (upper left (0-80 mm)) with the drop-sorting scheme (upper right) rainfall total after 3 h using a beam elevation of 1.5° (beam height lower right (0-1800 m)) and the native horizontal resolution of 2.5 km. The accumulation error over this period for these options is also shown using a scale of ±25 mm (lower left).

| **Original Rainfall Total** | | | | | **0.5° Rainfall Total** | | | | | **1.5° Rainfall Total** | | | |
|---|---|---|---|---|---|---|---|---|---|---|---|---|---|
| 41.27 | 25.35 | 21.57 | 10.05 | | 40.53 | 25.22 | 21.23 | 9.95 | | 40.16 | 25.26 | 20.80 | 9.80 |
| 25.76 | 13.53 | 17.86 | 8.23 | | 25.81 | 13.88 | 17.74 | 9.09 | | 25.82 | 14.39 | 17.67 | 10.14 |
| 29.64 | 20.77 | 10.88 | 16.49 | | 29.40 | 21.78 | 12.37 | 17.74 | | 29.61 | 22.90 | 14.23 | 19.60 |
| 18.37 | 29.67 | 29.90 | 26.92 | | 18.82 | 29.56 | 30.22 | 26.85 | | 19.41 | 29.67 | 30.54 | 26.65 |
| 25.76 | 42.01 | 56.36 | 44.85 | | 26.34 | 42.83 | 55.37 | 44.98 | | 27.34 | 44.08 | 54.30 | 45.05 |
| 57.78 | 31.94 | 6.12 | 37.30 | | 56.24 | 30.86 | 7.94 | 35.93 | | 54.77 | 29.72 | 10.44 | 34.73 |
| 3.41 | 3.39 | 2.43 | 2.81 | | 4.25 | 3.93 | 2.53 | 3.93 | | 5.10 | 4.49 | 2.84 | 5.18 |

**Table 4.4.1:** Comparison of total rainfall (in mm) after 3 h for the 3 November 2000 case from a selected area that covers the grid from cell (9,26) to (12,32) for drop-sorting scheme using both a 0.5° and 1.5° beam elevation and native horizontal resolution of 2.5 km.

ranges for beam elevations lower than 1.5°. The edge of the image approach values near 2 km in height; thus, wind-drift will have a greater effect. The rainfall comparisons in this case are very similar toward the most intense rainfall

amounts near the center of the image; however, there is some dispersion of the rainfall patterns and decrease in intensity in the western and southwestern areas. The estimated accumulation errors are still not very significant, but the near 8 mm magnitude of error is more intense than the lower beam elevations for both horizontal resolutions. A comparison of the rainfall totals from a west central region in the domain using the different beam elevations and native horizontal resolution is shown in Table 4.4.1.

### 4.4.4 Beam Elevation of 1.5° with Topography

The final set of images in the beam elevation experiments involves using the higher beam elevation of 1.5°, the standard horizontal resolution of 2.5 km, and topography (Fig. 4.4.4). This case is unique to most rainfall estimating techniques because it accounts for topography with beam elevation. The areas of the highest beam altitude to the west of the image are decreased by subtracting the height of topography, thus keeping the effect of wind-drift, whereas, the areas to the east over the water have a great wind-drift effect because the precipitation falls the entire beam height to the water. The maximum magnitude of estimated error is reduced slightly with the inclusion of topography (~7 mm) due to the heights being lower where significant convection is occurring. The estimated accumulation error image resembles the similar case without topography, but if the convection was hypothetically concentrated over the mountains for a significant period of time the errors would show up to a greater extent. An area selected over higher terrain elevation was selected for a numerical comparison to illustrate the reduced effect of wind-drift in this region (Table 4.4.2).

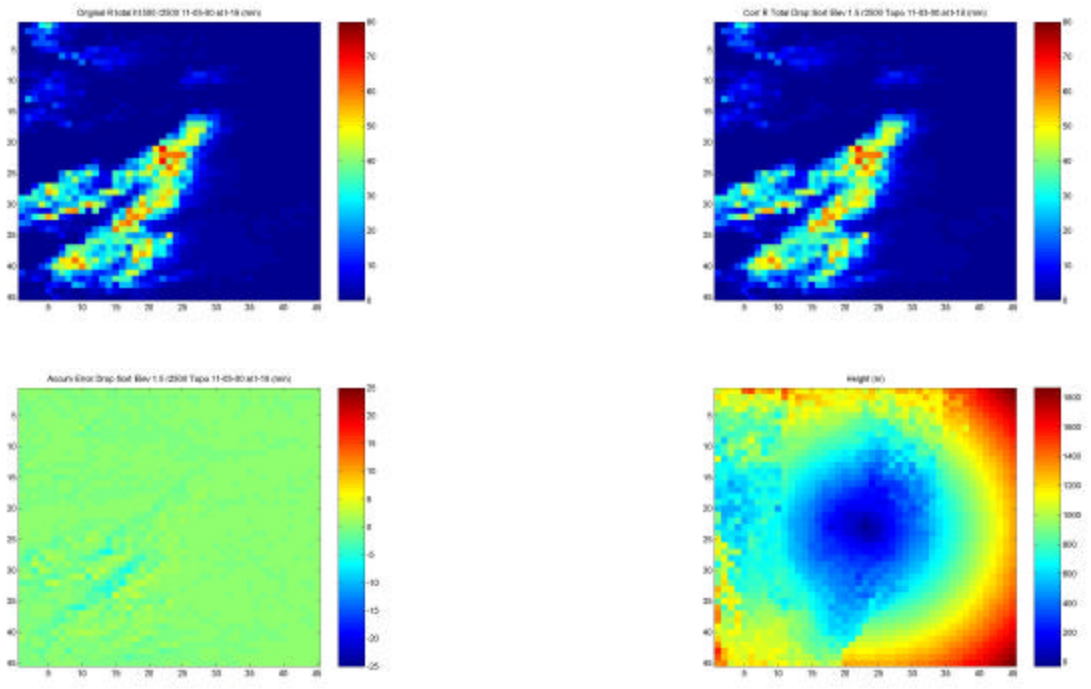

**Figure 4.4.4:** Original rainfall total after 3 h for the 3 November 2000 case (upper left (0-80 mm)) with the drop-sorting scheme (upper right) rainfall total after 3 h using a beam elevation of 1.5° with topography (beam height lower right (0-1800 m)) and the native horizontal resolution of 2.5 km. The accumulation error over this period for these options is also shown using a scale of ±25 mm (lower left).

| **Original Rainfall Total** | | | | | **1.5° Rainfall Total with Topography** | | | |
|---|---|---|---|---|---|---|---|---|
| 0.96 | 1.58 | 5.34 | 10.19 | | 1.06 | 1.97 | 5.66 | 9.85 |
| 1.80 | 6.01 | 9.15 | 14.05 | | 2.37 | 6.26 | 9.12 | 13.92 |
| 5.09 | 10.98 | 6.99 | 7.83 | | 5.52 | 10.65 | 7.02 | 7.67 |
| 22.78 | 13.61 | 5.65 | 6.33 | | 21.98 | 13.28 | 5.69 | 6.26 |
| 0.18 | 2.05 | 3.96 | 2.04 | | 1.33 | 2.46 | 4.11 | 2.39 |
| 5.15 | 6.39 | 10.27 | 3.19 | | 4.99 | 6.24 | 10.04 | 3.18 |
| 12.76 | 9.38 | 5.43 | 5.53 | | 12.44 | 9.29 | 5.64 | 5.52 |

**Table 4.4.2:** Comparison of total rainfall after 3 h for the 3 November 2000 case from a selected area that covers the grid from cell (2,10) to (5,16) for the drop-sorting scheme using the 1.5° beam elevation, native horizontal resolution of 2.5 km, including topography.

### 4.4.5 Summary of Beam Elevation Runs

The hypothetical use of beam elevation angles is an attempt to illustrate the effect of wind-drift using typical radar modes of operation. Precipitation estimates from operational radars are usually derived by using the lowest beam elevation available and extrapolating the precipitation downward to the surface, or by using maximum reflectivity in a column. Some of the differences in the experiments performed in the previous section are shown in Table 4.4.3. When examining 'Accum Sum' in this table, it is interesting to note the difference between using the lowest beam elevation angle and using the standard 1.5 km CAPPI height for the 3 November 2000 case. Out of all the experiments and case studies the 'Accum Sum' is lowest for the lowest beam elevation angle. Also, using the 1.5° beam elevation angle yields the highest possible difference in rainfall totals. For the first time in all experiments, increasing the horizontal resolution is not the source of the maximum error; it is increasing the beam elevation. Although the estimated accumulation error only approaches 8 mm in this case, other possible differences could be significant, especially at a longer range outside the domain used in this study.

| Case | Scheme | Height | Resolution | Accum Sum | Error per grid | Max Over | Max Under | Max Abs Val | St Dev | Max R | Max R Corr | Difference | Div/Conv |
|---|---|---|---|---|---|---|---|---|---|---|---|---|---|
| 20001103 | DS | 0.5 deg | 2.5km | -15.185 | -0.007 | 1.954 | -3.508 | 3.508 | 0.422 | 69.371 | 68.005 | 1.366 | net div |
| 20001103 | DS | 1.5 deg | 2.5km | -215.885 | -0.107 | 3.852 | -7.477 | 7.477 | 0.876 | 69.371 | 67.770 | 1.601 | net div |
| 20001103 | DS | 0.5 deg | 0.5km | -55.050 | -0.027 | 2.243 | -4.389 | 4.389 | 0.500 | 69.371 | 67.893 | 1.478 | net div |
| 20001103 | DS-topo | 1.5 deg | 2.5km | -153.775 | -0.076 | 3.581 | -6.603 | 6.603 | 0.736 | 69.371 | 67.844 | 1.527 | net div |

**Table 4.4.3:** Summary of the statistics generated when applying the wind-drift schemes for multiple resolutions to the original data for the 3 November 2000 case using beam elevation angles. The units are in mm for the data displayed.

# Chapter 5 Discussion

## 5.1 Comparison of Schemes

The experiments, within the scope of this research, attempt to show that the effect of wind-drift on falling precipitation is significant and needs to be quantified. This is especially necessary for hydrological applications where precipitation estimates need to be of high spatial accuracy in order to accurately predict streamflow and other hydrometeorological variables. The effect of wind-drift is unique depending on the case analyzed, the resolution used, and other various assumptions are changed within the bulk-advection and drop-sorting schemes. Error in the experiments presented is defined as the difference between the original field of reflectivity and the field of reflectivity after the wind-drift scheme is applied. The errors between the rainfall total derived from the original reflectivity, highest values smoothed to 53 dBZ in the case of severe convection, range from negligible to intense as different assumptions are used.

This approach by no means is a perfect adjustment for handling the effect of wind-drift. There experiments use only one level of radar reflectivity and one level of u, v, and w wind fields. The schemes still illustrate the need for the inclusion of wind-drift despite the simplicity. The horizontal winds are assumed to decrease linearly with height (constant shear profile) from the level of origin to the surface yielding a parabolic droplet trajectory. The wind-drift schemes

implicitly handle convergence and divergence of rainfall as it falls to the surface by allowing the possibility of neighboring grids to contribute to the same grid square at the surface. The schemes, in their current states, do not handle droplet growth or decay (loss) due to evaporation.

Since the schemes do not explicitly handle complex shear profiles because it only incorporates winds from one level, it is interesting to compare the two convective cases in this study. The wind level used is well below the steering level wind so directional shear is implicitly accounted for in the difference between storm motion and rain motion. The 3 November 2000 case is a supercellular case, which by definition contains a significant amount of directional shear (turning of the winds with height). The 26 September 2000 case most likely has a fair amount of speed shear (increase of wind speed with height), but low directional shear as the storm pattern is more linear in nature. In the supercellular case, the flow used in the calculation of wind-drift is nearly perpendicular to the northeasterly storm track resulting in a coupling of over- and underestimation along the axis of the track. For the 26 September 2000 case, the flow aloft is nearly parallel to the steering flow of the storm, resulting in less of a coupling effect. Therefore, in convection associated with strong directional shear, the wind-drift effect accounts for a larger difference in accumulation than storms that advect precipitation along the storm track due to weak, or no, directional shear.

One of the uncorrectable errors involves an "edging" effect, which evolves when rain is advected out of the any finite grid of data. In these experiments, the domain is unrealistically small for most operational uses. These errors are listed in each appendix as "Accum Sum." Although the error from the edging effect is not uniform throughout all grid squares, the edging effect error per grid square is listed in each appendix as "Error per grid." The overall maximum error per

grid square is for the 3 November 2000 event at the higher horizontal resolution and is near 0.5 mm. The majority of the more intense edging effect errors are a result of increasing the resolution in the convective cases due to heavy precipitation being advected more efficiently out of the dimensions of the domain. The errors are smallest in the stratiform cases where the precipitation is weaker, but in these cases the rain is advected further. Using the lowest beam elevation of 0.5° also reduced the edging effect by reducing the effect of wind-drift on falling precipitation overall.

The highest, most significant errors when comparing the rainfall accumulation from the original reflectivity and the rainfall accumulation after the wind-drift schemes are applied to the original reflectivity are found in the convective cases at the increased resolution. For example, some of the maximum differences in rainfall totals come from 3 November 2000 at the highest horizontal resolution of 0.5 km and the highest CAPPI height of 1.5 km and are on the order of 50 mm. The smallest errors are found in the stratiform case on 18 November 2000 where the rainfall amounts are generally smaller. The smallest errors in all the cases occur on the native horizontal resolution as it is a larger area for the precipitation to advect out of an individual grid square. The combination of using the highest altitude reflectivity fields, highest horizontal resolution, and the heaviest precipitation yields the highest error due to wind-drift; the reverse is true for the lowest accumulation errors after the time period for the event.

When comparing the standard deviation of all the events used, some interesting results appear. The percentage increase in the error of the standard deviation when changing the horizontal resolution is nearly the same for each event. For example, the percent increase of the standard deviation from the native horizontal resolution to 1.5 km from 3 November 2000 for both schemes is

about 51% and from 1.5 km to 0.5 km is on the order of 150%; for the stratiform case the percent increase is around 55% and again on the order of 150%, respectively. Comparing the severe convective case and stratiform case to the 26 September 2000 case reveals an approximate increase in the standard deviation on the order of 275% for each event from the native horizontal resolution to 0.5 km. This shows that the effect of wind-drift is approximately the same for any situation given the same horizontal resolution is applied, although the magnitude is governed by actual precipitation amounts.

The accumulation error statistics do not matter much unless the spatial coverage of these errors is discussed. As shown above, the convective cases contain the largest spatial coverage of accumulation error. The width of the area of under and overestimation coupling using the native resolution is approximately 20 km for the case on 3 November 2000. This magnitude of error over this spatial coverage can have severe implications in hydrometeorological applications. Although 20 km seems like a small area, terrain can change vastly, causing different responses to streamflow from different catchments into which the rain could be falling. Errors become significant in streamflow, especially if a change in watershed or sub-watershed occurs over the 20 km. Land improvements and boundaries between rural and urban areas can also cause changes in streamflow over smaller domains on smaller spatial scales. When running the wind-drift schemes at 0.5 km and having spatial error on the order of 10 km with intense magnitude of error (~50 mm over 3 h) streamflow can be significantly changed, especially in regions separated by different river basins or urban and rural boundaries. Changes in topography and/or changes in soil type can also occur over such a small spatial scale and will also have a great impact on the predicted streamflow from radar derived surface rainfall estimations.

For the stratiform case and the schemes in which lower accumulation errors are found, the duration of the event governs the amount of accumulation error. For example, since the time frame used in the stratiform case is only 3 h and the accumulation errors range from 2 mm to 9 mm, if the event lasted all day these errors could reach to 8 times this amount for a given location. Convective events are usually of shorter duration than stratiform events, but training convective systems can be of significant duration and lead to enormous accumulation errors. Overall, if the events are longer lived, the accumulation error after the wind-drift schemes are applied become even more significant.

Changing the Z-R relationship causes changes in the error created when examining the rainfall totals and the errors associated with the output from the wind-drift schemes. The problem exists outside the realm of the wind-drift research presented here. A standard Z-R relationship is selected based on the situation in question from those given in Table 2.2.1. It is well known that for a typical precipitation event different genres of precipitation exist, for example, a single event could have areas of stratiform and convective precipitation under the same radar umbrella. If the areas are easily distinguished a Z-R relationship can be assigned in different regions of the radar scan for increased accuracy (Biggerstaff and Listemaa, 2000). However, the situation becomes even more complex if an area of stratiform precipitation is present behind a line of convective precipitation. It becomes harder to adjust Z-R relationships in patterns of precipitation with large areas of stratiform precipitation with embedded convective cells. The choice of Z-R relationships causes differences in rainfall totals, which causes differences in the accumulation errors existing from applying the wind-drift schemes. For example, the rainfall rate at 45 dBZ using the convective relationship in the wind-drift schemes is approximately 28 mm $h^{-1}$ and the stratiform is approximately 24 mm $h^{-1}$. If a more intense tropical

convection scheme, from Table 2.2.1, is used, the rainfall rate becomes approximately 56 mm $h^{-1}$. Using advanced radar technology with three variable rainfall relationship equations, the problem of Z-R relationships may be reduced further in the future and these techniques will be used solely in future wind-drift schemes.

In most radar applications, rainfall estimates are calibrated using rain gauge measurements underneath the radar umbrella. There are many methods currently used to relate the point measurement of rainfall to the areal measurement given by the radar. However, especially in the case of wind-drift, relating the rainfall estimations from radar to a point measurement by a gauge is a poor idea. First, the error associated with gauge measurements can be extreme. In addition to the inherent error of the gauge, taking many point observations even on a small spatial scale can vary intensely from point to point, which begs the issue of which observation is the most representative to correlate to the radar, or should an average over the radar domain be taken. In the case of the research presented, correlating rain gauge data to radar data at high ranges without correcting for wind-drift could cause major differences in the data that might be used in hydrometeorological applications. Therefore, it is unhelpful to compare rainfall estimates from radar to point measurements after correcting for wind-drift unless there is an analysis of the uncertainty for all variables included in the correlation (Tustison *et al*., 2001). Overall, there are many uncertainties inherent in radar data and rain gauge networks and all possible sources of error, including wind-drift, need to be accounted for and quantified. The best case for comparison would be to take a point measurement to determine if it is raining in an area where the "raw" radar is not detecting rainfall over the point, but the wind-drift correction reveals precipitation over the gauge. The experiments

within the scope of this research are to demonstrate that errors in surface rainfall estimations from radar exist and can be significant.

## 5.2 Miscellaneous Results

The miscellaneous runs used in this research were selected for completeness of experiments that are possible with the different wind-drift schemes presented here. Additional assumptions can be adapted and changes in the code can be easily made. Some of the most important issues that need to be addressed such as beam elevations, calculations of mean drop-size diameters, and an additional case study are presented as miscellaneous runs. The implications of these miscellaneous runs will be discussed in this section.

Some interesting results are shown when examining the cases that incorporate a hypothetical beam elevation instead of the native CAPPI images that the data sets contain. Beam elevations are typically used in most radar applications; however, in order to assess wind-drift in the case of a beam elevation, the wind speeds derived from Doppler radar and assimilated into an adjoint model must match the height of the beam at a given range from the radar. One problem with using this simplified beam elevation approach is there is no account for changes in refractive index in the atmosphere. This results in a source of error by misrepresenting the beam height at certain locations, which can vary along different radials during the scan. The bright band, in cases of cooler rain events, must also be carefully corrected for before a rainfall relationship is applied, as the given elevation angle might cross a melting level.

In most radar rainfall estimation processes, the lowest beam elevation angle is used to estimate the surface rainfall field. Also used is the 'maximum reflectivity' volume scan, where the maximum reflectivity over a given pixel from any elevation is used. However, more sophisticated data, which have been properly corrected, also result in a potential lack of knowledge as to the representative height of the volume the radar is sampling. Complex scan patterns can exist so that changes in the beam angle occur during a single scan strategy in cases of topography in certain quadrants under the radar umbrella. In the case of the CPOL radar at Badgerys Creek, the 0.5° beam elevation angle could be used as the topography to the west would still fall below the radar beam. It is interesting to note that if topography is incorporated within the wind-drift scheme, the wind-drift effect would be decreased over the mountains to the west of the domain since the difference between the radar beam and the topography is small. Even at increased ranges, as long as the difference between the topography and the height of the radar beam given by the beam elevation is small, the errors associated with wind-drift are small.

Examining the differences between the schemes using a CAPPI and a low beam elevation reveals that overall the wind-drift errors are reduced when using the lowest beam elevation available. The reduction in wind-drift at small ranges from the radar is most notable. However, with increased range comes a greater error when the wind-drift schemes are applied. This is most recognized in a location like Columbia, MO where the average beam height is over 1 km. This also illustrates the error associated with poor radar coverage caused by large gaps between operational radars. To accurately use radar estimates of precipitation it is best to have a radar at a short range to the point of interest. It is also interesting to note that in the 26 September 2000 case when the wind-drift scheme was applied to a CAPPI the highest errors exist near the CPOL. If a

lower beam elevation angle was used instead of a CAPPI, the errors nearest to the radar would be reduced to the point of being negligible. As a side note, using the lowest beam elevation may introduce additional clutter near the radar, due to side lobes picking up surface targets, and a clutter filter would need to be applied for accurate rainfall estimates.

An additional option in the programming involved changing the architecture of the drop-sorting scheme. Using a weighted mean droplet diameter examined the possible error involved in the assumption that the arithmetic mean given by the range of droplet sizes for a bin is a good approximation. Although using the arithmetic mean is not as physically accurate, the difference between the two calculations of the mean drop-size within a bin is negligible since the bins use such small ranges. Using a weighted mean would explain differences if a consistent systematic power gain when the schemes were applied was found. However, as shown in previous tables, there is a net loss of power due to the "edging effect," precipitation being advected out of the given domain. This masks any possible artificial gain from using the arithmetic mean; therefore, it is unnecessary to use the weighted mean scheme in this situation. In addition, using the arithmetic mean reduces computational time slightly.

## 5.3 Implications of Frozen Precipitation

Although it is well known in the field of radar meteorology that, given current operational technology, radar estimates of snow accumulation should not be attempted, the effect of wind-drift on frozen precipitation can still be addressed. Given a reflectivity image, it may be possible to determine heavier

areas of snowfall, although not necessarily quantifiably. These embedded snow bands might be advected by the wind a considerable distance in the horizontal. Predicting the location of heavy snowfall bands is of primary importance in the issue of public safety.

If the wind-drift scheme was hypothetically applied to cases of snow, the errors with respect to the wind-drift schemes would most likely be greater than that of cases of pure rainfall due to much lower fall speeds of the hydrometeors. There are many problems when dealing with estimates of wind-drift in cases of snow fall. First, fall speeds are on the order of 1 m $s^{-1}$. Therefore, some snow may be in the atmosphere for long durations of time depending upon the locations of the updrafts and downdrafts that exist. Second, the radar must actually pick up the snow. In cases where the beam elevation or CAPPI is too high, the radar might actually miss entire regions of low-elevation precipitation, which is common for snow events. Although there are more assumptions to be made when dealing with snow, the slower fall speed alone would cause intense errors of wind-drift to exist. Ignoring vertical velocity and assuming a fall speed of 1 m $s^{-1}$, a height of 1000 m, and a horizontal wind speed of 10 m $s^{-1}$, the lateral advection of snowfall would be approximately 10 km.

The above illustrates the complications of dealing with snowfall alone. The situation of applying the wind-drift schemes to mixed precipitation becomes even more complicated. Although polarimetric radars can discriminate between precipitation types fairly accurately, this is done aloft using radar data and surface observations are still necessary to truly determine precipitation type at the ground. This fact alone leads to the conclusion that the wind-drift schemes should only be applied to cases of pure warm season-type rainfall for an accurate representation of rainfall estimation at the surface.

# Chapter 6 Conclusions and Future Directions

## 6.1 Conclusions

Although the majority of the schemes were simplified explorations of methods to correct for wind-drift on falling precipitation the quantification of errors reveals that the errors would be significant even after fine-tuning the programming. Of the errors that are primarily examined, most meaningful are the accumulation errors (defined as the difference between the original reflectivity and wind-drift adjusted reflectivity) after a given duration given by the difference in the rainfall estimations given by the original radar reflectivity and the wind-drift surface rainfall estimation fields. Many different experiments were run on three different case studies, including hypothetically increasing the horizontal resolution, reducing the CAPPI height, using different beam elevations instead of constant altitude plots, and slightly adjusting the equations used in the programs.

This research illustrates the need for correcting for wind-drift on any horizontal resolution scale with any height scheme. At higher resolutions, the errors due to wind-drift are increased in all cases as most of the precipitation from one grid square is almost entirely advected into another nearby grid square over a different location on the surface. Decreasing the height of the CAPPI or, at short ranges, using beam elevations causes a decrease in the wind-drift effect as

the precipitation fall time to the surface is reduced. Incorporating topography can also decrease the error in the case of elevated terrain, or increase error in the presence of valleys. This is due to the decrease (increase) of fall time due to the difference between beam height and terrain decreasing (increasing). The lowest wind-drift errors are found using a low beam elevation at close ranges to the radar. Also, when using beam elevations, the increase in horizontal resolution has less of an effect on accumulation errors than when using a CAPPI. The standard deviation of the accumulation errors over the domain increases as the horizontal resolution increases, regardless of what scheme and case is used. The percentage of increase in the standard deviations as the horizontal resolution is increased between the stratiform and convective cases is nearly identical. This shows that in all cases the effect of wind-drift is approximately the same; the magnitude of the accumulation error is the only difference and that is a function of the intensity of the rainfall event. The comparison of errors between the bulk-advection and drop-sorting schemes reveals the two are similar for all cases and resolutions; however, the drop-sorting scheme may be physically more realistic than the simplified bulk-advection scheme.

In summary, it was demonstrated that

- the two wind-drift schemes were successfully run with different horizontal resolutions and CAPPI heights (or beam elevations) with and without topography included, and possible error statistics were compiled,
- the estimated errors were significant, especially at higher horizontal resolutions and higher beam elevations (CAPPIs) and when topography was not included, and

- the percent increase of standard deviation of possible errors as horizontal resolution was increased remained relatively constant for each of the three events examined.

## 6.2 Future Directions

The future of the wind-drift schemes is dependent on advances in technology and data that are available to input into the different schemes. Depending on the technology used and the available data, different assumptions can be applied within the architecture of both the bulk-advection and drop-sorting schemes. Some changes that could take place immediately include using the weighted mean drop-size formulation while changing the calculations for $N_0$ and $N_d$ depending on how one should choose to represent drop-size distributions. Also, multiple-level wind-field data from the adjoint model could be incorporated to give a more meaningful and physically accurate representation of speed and directional shear for the advection of precipitation in a layer; this includes use of the surface wind field. Since multiple wind field data exists, beam elevations could probably be incorporated successfully. New calculations of droplet fall speeds and vertical velocities can also be incorporated in the future. Rainfall estimation relationships can be changed as the full capability of polarimetric radars is used to more accurately represent precipitation amounts aloft. Other future work in the area of enhancing the corrections to surface rainfall fields derived from radar reflectivity will involve the addition of an evaporation scheme to the wind-drift scheme. To be successful the scheme will have to incorporate below cloud relative humidity information and apply it to the falling drop-sizes, resulting in a loss or gain of

droplet size. This would further increase the spatial accuracy on surface rainfall estimates from radar. In addition, future case studies using NEXRAD data to examine errors at full range would be useful. Overall, the program is robust and can handle a change in many assumptions easily.

# Appendix A: Bulk-advection Code

```
%Convective Bulk-advection Scheme Version 5
%Written by Steve Lack, December 2003

for a=1:45
   for b=1:45
      AccumulationError(a,b)=0;
      Rtotal(a,b)=0;
      CorrRtotal(a,b)=0;
   end
end

%Matrix of characters so that files will be loaded though use of a loop
fileDBZ =
char('DBZ20001103030500.txt','DBZ20001103031500.txt','DBZ20001103032500.txt','DBZ200011030335
00.txt','DBZ20001103034500.txt','DBZ20001103035500.txt','DBZ20001103040500.txt','DBZ20001103041
500.txt','DBZ20001103042500.txt','DBZ20001103043500.txt','DBZ20001103044500.txt','DBZ2000110304
5500.txt','DBZ20001103050500.txt','DBZ20001103051500.txt','DBZ20001103052500.txt','DBZ200011030
53500.txt','DBZ20001103054500.txt','DBZ20001103055500.txt');
fileU =
char('U20001103030500.txt','U20001103031500.txt','U20001103032500.txt','U20001103033500.txt','U200
01103034500.txt','U20001103035500.txt','U20001103040500.txt','U20001103041500.txt','U200011030425
00.txt','U20001103043500.txt','U20001103044500.txt','U20001103045500.txt','U20001103050500.txt','U20
001103051500.txt','U20001103052500.txt','U20001103053500.txt','U20001103054500.txt','U20001103055
500.txt');
fileV =
char('V20001103030500.txt','V20001103031500.txt','V20001103032500.txt','V20001103033500.txt','V200
01103034500.txt','V20001103035500.txt','V20001103040500.txt','V20001103041500.txt','V200011030425
00.txt','V20001103043500.txt','V20001103044500.txt','V20001103045500.txt','V20001103050500.txt','V20
001103051500.txt','V20001103052500.txt','V20001103053500.txt','V20001103054500.txt','V20001103055
500.txt');
fileW =
char('W20001103030500.txt','W20001103031500.txt','W20001103032500.txt','W20001103033500.txt','W2
0001103034500.txt','W20001103035500.txt','W20001103040500.txt','W20001103041500.txt','W20001103
042500.txt','W20001103043500.txt','W20001103044500.txt','W20001103045500.txt','W20001103050500.t
```

```
xt','W20001103051500.txt','W20001103052500.txt','W20001103053500.txt','W20001103054500.txt','W20
001103055500.txt');

%get the beam height at all grid locations can adjust for different beam
%elevations et cetera
for i=1:45
   for j=1:45
      range(i,j)=sqrt(((2.5*(i-23))^2)+((2.5*(j-23))^2));
   end
end
Ho=.01; %height of the radar in kilometers
Re=6374; %radius of the earth in kilometers, can be site specific if lat and lon is used
Rprime=4/3*Re; %effective radius for curvature of the earth
phi=0.5*pi/180;  %beam elevation in radians
%loop for height of beam at center of a given pixel
for a=1:45
   for b=1:45
      height1(a,b)=(sqrt((range(a,b)^2)+(Rprime^2)+(2*range(a,b)*Rprime*sin(phi)))-Rprime+Ho)*1000;
   end
end

load cpoltopography.mat %remove this and set height to CAPPI if terrain is not used
height=height1-newtopo;
%height=1500;  %Set to CAPPI
resolution=2500;

%filer out weak returns and load files to be run in main program loops
%initial loop to go though files that contain the different time steps
for c=1:18
   load (fileDBZ(c,:));
   load (fileU(c,:));
   load (fileV(c,:));
   load (fileW(c,:));

for g=1:45,
   for h=1:45,
      Controllo(g,h)=10;
```

```
        Controlhi(g,h)=53;
    end
end
dBZ=load (fileDBZ(c,:))>Controllo;
dBZ= dBZ .*load (fileDBZ(c,:));
for i=1:45
    for j=1:45
        if (dBZ(i,j)>=Controlhi)
            dBZ(i,j)=53;
        end
    end
end

U=load (fileU(c,:));
V=load (fileV(c,:));
W=load (fileW(c,:));

%Initial Calculations
for i=1:45
    for j=1:45
        Zunit(i,j)= 10^(dBZ(i,j)/10);
    end
end
for i=1:45
    for j=1:45
        if(Zunit(i,j)<=1)
            Zunit(i,j)=0;
        end
    end
end
R = (Zunit ./300) .^(1/1.4); %convective rain Z-R can change to anything
VfOld=4.5 .*(R .^(1/9)); %estimated avg fall speed in pixel based on R and the assumed DSD from the Z-
R relationship
VfNew=(VfOld-(W)); %incorporates local updrafts and downdrafts
for i=1:45
    for j=1:45
        if (VfNew(i,j)<0)
```

```
        VfNew(i,j)=0;
      end
    end
end
DriftX= (U .*height) ./(2 .*VfNew); %using parabolic trajectory drift distance in x-dir
DriftY= (V .*height) ./(2 .*VfNew); %using parabolic trajectory drift distance in y-dir
DriftXYtemp= (DriftX .^2) + (DriftY .^2); %temp calc holder
DriftXY= sqrt(DriftXYtemp); %total dist travel away from center of pixel

%Next calculates the cell contribution to itself, *no longer needed just in
%case one is curious about cell contributions to itself
i=1;
j=1;
for i=1:45
    for j=1:45
      if (DriftXY(i,j)<=resolution)
        SelfCont=(((resolution-abs(DriftX(i,j)))*(resolution-abs(DriftY(i,j))))/(resolution^2))*Zunit(i,j);
      else
        SelfCont(i,j)=0;
      end
    end
end

%Outer loop calculates the new matrix of corrected dBZ from wind-drift
%Inner loop calculates a matrix for cell contributions to a single pixel
%Last step sums up the cell contributions to be placed in the outer loop
%corrected dBZ matrix
g=1;
h=1;
for g=1:45,
    for h=1:45,
      CorrZunit(g,h)=0;
    end
end
i=1;
j=1;
for i=1:45
```

```
  for j=1:45
      a=1;
      b=1;
      for a=1:45
         for b=1:45
            if(((DriftY(a,b)<=((a-i)-1)*resolution)|(DriftY(a,b)>=((a-i)+1)*resolution))|((DriftX(a,b)<=((j-b)-
1)*resolution)|(DriftX(a,b)>=-((b-j)-1)*resolution)))
               Contrib(a,b)=0;
            else
               Contrib(a,b)=((abs(resolution-abs(((b-j)*-resolution)-DriftX(a,b)))*abs(resolution-abs(((a-
i)*resolution)-DriftY(a,b))))/resolution^2)*Zunit(a,b);
            end
         end
      end
      x=1;
      y=1;
      for x=1:45
         for y=1:45
            CorrZunit(i,j)=CorrZunit(i,j)+Contrib(x,y);
         end
      end
   end
end

%displays for comparison the rainfall rates and the rounded dBZ values for
%the corrected and original data set
i=1;
j=1;
for i=1:45
   for j=1:45
      if(CorrZunit(i,j)<=10)
         CorrZunit(i,j)=0;
      end
   end
end
for i=1:45
   for j=1:45
```

```
      if(CorrZunit(i,j)>0)
         CorrdBZ(i,j)=(10*(log10(CorrZunit(i,j))));
      else
         CorrdBZ(i,j)=0;
      end
   end
end
for i=1:45
   for j=1:45
      CorrR(i,j)=(CorrZunit(i,j)/300)^(1/1.4);
   end
end
Error=(CorrR-R);
CorrRtotal=CorrRtotal+(CorrR .*(10/60));
Rtotal=Rtotal+(R .*(10/60));
AccumulationError=(Rtotal-CorrRtotal);

%figures
figure;
imagesc(dBZ);
caxis([0 60]);
colorbar;
title('Original dBZ h1500 r2500 11-03-00 at t-18 (dBZ)')
OriginaldBZconv(c)=getframe;

figure;
imagesc(Rtotal);
caxis([0 80]);
colorbar;
title('Original R total h1500 r2500 11-03-00 at t-18 (mm)')
OriginalRtotalconv(c)=getframe;

figure;
imagesc(CorrdBZ);
caxis([0 60]);
colorbar;
title('Corr dBZ Bulk Adv h1500 r2500 Beam Ele 11-03-00 at t-18 (dBZ)')
```

```
CorrdBZbaconvh1500r2500beamele(c)=getframe;

figure;
imagesc(CorrRtotal);
caxis([0 80]);
colorbar;
title('Corr R Total Bulk Adv h1500 r2500 Beam Ele 11-03-00 at t-18 (mm)')
CorrRtotalbaconvh1500r2500beamele(c)=getframe;

figure;
imagesc(AccumulationError);
caxis([-25 25]);
colorbar;
title('Accum Error Bulk Adv h1500 r2500 Beam Ele 11-03-00 at t-18 (mm)')
accumerrorbaconvh1500r2500beamele(c)=getframe;
end

%movies

movie(OriginaldBZconv);
movie2avi(OriginaldBZconv,'OriginaldBZconv.avi','fps',5,'quality',100);

movie(OriginalRtotalconv);
movie2avi(OriginalRtotalconv,'OriginalRtotalconv.avi','fps',5,'quality',100);

movie(CorrdBZbaconvh1500r2500beamele);
movie2avi(CorrdBZbaconvh1500r2500beamele,'CorrdBZbaconvh1500r2500beamele.avi','fps',5,'quality',10
0);

movie(CorrRtotalbaconvh1500r2500beamele);
movie2avi(CorrRtotalbaconvh1500r2500beamele,'CorrRtotalbaconvh1500r2500beamele.avi','fps',5,'quality
',100);

movie(accumerrorbaconvh1500r2500beamele);
movie2avi(accumerrorbaconvh1500r2500beamele,'accumerrorbaconvh1500r2500beamele.avi','fps',5,'qualit
y',100);
```

# Appendix B: Drop-sorting Code

```
%Drop-sorting Scheme Convective Version 4
%Written by Steve Lack, December 2003

%Set initial accumulation matrices to 0
for a=1:45
   for b=1:45
      AccumulationError(a,b)=0;
      Rtotal(a,b)=0;
      CorrRtotal(a,b)=0;
   end
end

%Matrix of characters so that files will be loaded though use of a loop
fileDBZ =
char('DBZ20001103030500.txt','DBZ20001103031500.txt','DBZ20001103032500.txt','DBZ200011030335
00.txt','DBZ20001103034500.txt','DBZ20001103035500.txt','DBZ20001103040500.txt','DBZ20001103041
500.txt','DBZ20001103042500.txt','DBZ20001103043500.txt','DBZ20001103044500.txt','DBZ2000110304
5500.txt','DBZ20001103050500.txt','DBZ20001103051500.txt','DBZ20001103052500.txt','DBZ200011030
53500.txt','DBZ20001103054500.txt','DBZ20001103055500.txt');
fileU =
char('U20001103030500.txt','U20001103031500.txt','U20001103032500.txt','U20001103033500.txt','U200
01103034500.txt','U20001103035500.txt','U20001103040500.txt','U20001103041500.txt','U200011030425
00.txt','U20001103043500.txt','U20001103044500.txt','U20001103045500.txt','U20001103050500.txt','U20
001103051500.txt','U20001103052500.txt','U20001103053500.txt','U20001103054500.txt','U20001103055
500.txt');
fileV =
char('V20001103030500.txt','V20001103031500.txt','V20001103032500.txt','V20001103033500.txt','V200
01103034500.txt','V20001103035500.txt','V20001103040500.txt','V20001103041500.txt','V200011030425
00.txt','V20001103043500.txt','V20001103044500.txt','V20001103045500.txt','V20001103050500.txt','V20
001103051500.txt','V20001103052500.txt','V20001103053500.txt','V20001103054500.txt','V20001103055
500.txt');
fileW =
char('W20001103030500.txt','W20001103031500.txt','W20001103032500.txt','W20001103033500.txt','W2
```

```
0001103034500.txt','W20001103035500.txt','W20001103040500.txt ','W20001103041500.txt','W20001103
042500.txt','W20001103043500.txt','W20001103044500.txt','W20001103045500.txt','W20001103050500.t
xt','W20001103051500.txt','W20001103052500.txt','W20001103053500.txt','W20001103054500.txt','W20
001103055500.txt');

%get the beam height at all grid locations can adjust for different beam
%elevations et cetera
for i=1:45
   for j=1:45
      range(i,j)=sqrt(((2.5*(i-23))^2)+((2.5*(j-23))^2));
   end
end
Ho=.01; %height of the radar in kilometers
Re=6374; %radius of the earth in kilometers, can be site specific if lat and lon is used
Rprime=4/3*Re; %effective radius for curvature of the earth
phi=1.5*pi/180;  %beam elevation in radians
%loop for height of beam at center of a given pixel
for a=1:45
   for b=1:45
      height1(a,b)=(sqrt((range(a,b)^2)+(Rprime^2)+(2*range(a,b)*Rprime*sin(phi)))-Rprime+Ho)*1000;
   end
end
load cpoltopography.mat %remove this and set height to CAPPI if terrain is not used
%height=1500-newtopo;
height=height1-newtopo; %If beam elevation is used
%height=1500; %if CAPPI height is used
resolution=2500;

%filer out weak returns and load files to be run in main program loops
%initial loop to go though files that contain the different time steps
for c=1:18 %change to make animation
   load (fileDBZ(c,:));
   load (fileU(c,:));
   load (fileV(c,:));
   load (fileW(c,:));

for g=1:45,
```

```
   for h=1:45,
      Controllo(g,h)=0;
      Controlhi(g,h)=53;
   end
end
dBZ=load (fileDBZ(c,:))>Controllo;
dBZ= dBZ .*load (fileDBZ(c,:));
for i=1:45
   for j=1:45
      if (dBZ(i,j)>=Controlhi)
         dBZ(i,j)=53;
      end
   end
end

U=load (fileU(c,:));
V=load (fileV(c,:));
W=load (fileW(c,:));

%Initial Calculations
for i=1:45
   for j=1:45
      OriginalZunit(i,j)= 10^(dBZ(i,j)/10);
   end
end
for i=1:45
   for j=1:45
      if(OriginalZunit(i,j)<=1)
         OriginalZunit(i,j)=0;
      end
   end
end
OriginalR = (OriginalZunit ./300) .^(1/1.4); %convective rain Z-R can change to anything
Lambda= 4.1 .*(OriginalR .^(-.2095)); %lambda calculation to get to Nd
for i=1:45
   for j=1:45
      if(Lambda(i,j)>9999)
```

```
        Lambda(i,j)=9999;
      end
    end
end
for i=1:45
    for j=1:45
      if(Lambda(i,j)<9999)
        No(i,j)=(99.869*exp(0.0617*dBZ(i,j))); %exponential fit of No for convective events
      else
        No(i,j)=0;
      end
    end
end

%Fill the z's,Vf's, DriftX, DriftY for bin layer 1
for i=1:45
    for j=1:45
      Zbinlayer1(i,j)=(((-No(i,j))*(Lambda(i,j))*exp((-Lambda(i,j))*7.5))-((-No(i,j))*(Lambda(i,j))*exp((-
Lambda(i,j))*7.2)))*(7.35^6);
    end
end
for i=1:45
    for j=1:45
      Vfbinlayer1(i,j)=(10.97553-W(i,j));
    end
end
for i=1:45
    for j=1:45
      DriftXbinlayer1(i,j)=(U(i,j)*height(i,j))/(2*Vfbinlayer1(i,j));
    end
end
for i=1:45
    for j=1:45
      DriftYbinlayer1(i,j)=(V(i,j)*height(i,j))/(2*Vfbinlayer1(i,j));
    end
end
```

```
%Outer loop calculates the new matrix of corrected dBZ from wind-drift
%Inner loop calculates a matrix for cell contributions to a single pixel
%Last step sums up the cell contributions to be placed in the outer loop
%corrected dBZ matrix (see notes for questions on geometry)
g=1;
h=1;
for g=1:45,
   for h=1:45,
      CorrZunitbinlayer1(g,h)=0;
   end
end
i=1;
j=1;
for i=1:45
  for j=1:45
      a=1;
      b=1;
      for a=1:45
         for b=1:45
            if(((DriftYbinlayer1(a,b)<=((a-i)-1)*resolution)|(DriftYbinlayer1(a,b)>=((a-
i)+1)*resolution))|((DriftXbinlayer1(a,b)<=((j-b)-1)*resolution)|(DriftXbinlayer1(a,b)>=-((b-j)-
1)*resolution)))
               Contribbinlayer1(a,b)=0;
            else
               Contribbinlayer1(a,b)=((abs(resolution-abs(((b-j)*-resolution)-
DriftXbinlayer1(a,b)))*abs(resolution-abs(((a-i)*resolution)-
DriftYbinlayer1(a,b))))/resolution^2)*Zbinlayer1(a,b);
            end
         end
      end
      x=1;
      y=1;
      for x=1:45
         for y=1:45
            CorrZunitbinlayer1(i,j)=CorrZunitbinlayer1(i,j)+Contribbinlayer1(x,y);
         end
      end
```

```
   end
end

%Fill the z's,Vf's, DriftX, DriftY for bin layer 2
for i=1:45
   for j=1:45
      Zbinlayer2(i,j)=(((-No(i,j))*(Lambda(i,j))*exp((-Lambda(i,j))*7.199))-((-
No(i,j))*(Lambda(i,j))*exp((-Lambda(i,j))*6.9)))*(7.0495^6);
   end
end
for i=1:45
   for j=1:45
      Vfbinlayer2(i,j)=(10.74539-W(i,j));
   end
end
for i=1:45
   for j=1:45
      DriftXbinlayer2(i,j)=(U(i,j)*height(i,j))/(2*Vfbinlayer2(i,j));
   end
end
for i=1:45
   for j=1:45
      DriftYbinlayer2(i,j)=(V(i,j)*height(i,j))/(2*Vfbinlayer2(i,j));
   end
end

%Outer loop calculates the new matrix of corrected dBZ from wind-drift
%Inner loop calculates a matrix for cell contributions to a single pixel
%Last step sums up the cell contributions to be placed in the outer loop
%corrected dBZ matrix (see notes for questions on geometry)
g=1;
h=1;
for g=1:45,
   for h=1:45,
      CorrZunitbinlayer2(g,h)=0;
   end
end
```

```
i=1;
j=1;
for i=1:45
  for j=1:45
      a=1;
      b=1;
      for a=1:45
         for b=1:45
            if(((DriftYbinlayer2(a,b)<=((a-i)-1)*resolution)|(DriftYbinlayer2(a,b)>=((a-
i)+1)*resolution))|((DriftXbinlayer2(a,b)<=((j-b)-1)*resolution)|(DriftXbinlayer2(a,b)>=-((b-j)-
1)*resolution)))
               Contribbinlayer2(a,b)=0;
            else
               Contribbinlayer2(a,b)=((abs(resolution-abs(((b-j)*-resolution)-
DriftXbinlayer2(a,b)))*abs(resolution-abs(((a-i)*resolution)-
DriftYbinlayer2(a,b))))/resolution^2)*Zbinlayer2(a,b);
            end
         end
      end
      x=1;
      y=1;
      for x=1:45
         for y=1:45
            CorrZunitbinlayer2(i,j)=CorrZunitbinlayer2(i,j)+Contribbinlayer2(x,y);
         end
      end
  end
end

%Fill the z's,Vf's, DriftX, DriftY for bin layer 3
for i=1:45
   for j=1:45
      Zbinlayer3(i,j)=(((-No(i,j))*(Lambda(i,j))*exp((-Lambda(i,j))*6.899))-((-
No(i,j))*(Lambda(i,j))*exp((-Lambda(i,j))*6.6)))*(6.7495^6);
   end
end
for i=1:45
```

```
    for j=1:45
        Vfbinlayer3(i,j)=(10.51411-W(i,j));
    end
end
for i=1:45
    for j=1:45
        DriftXbinlayer3(i,j)=(U(i,j)*height(i,j))/(2*Vfbinlayer3(i,j));
    end
end
for i=1:45
    for j=1:45
        DriftYbinlayer3(i,j)=(V(i,j)*height(i,j))/(2*Vfbinlayer3(i,j));
    end
end

%Outer loop calculates the new matrix of corrected dBZ from wind-drift
%Inner loop calculates a matrix for cell contributions to a single pixel
%Last step sums up the cell contributions to be placed in the outer loop
%corrected dBZ matrix (see notes for questions on geometry)
g=1;
h=1;
for g=1:45,
    for h=1:45,
        CorrZunitbinlayer3(g,h)=0;
    end
end
i=1;
j=1;
for i=1:45
   for j=1:45
        a=1;
        b=1;
        for a=1:45
            for b=1:45
                if(((DriftYbinlayer3(a,b)<=((a-i)-1)*resolution)|(DriftYbinlayer3(a,b)>=((a-
i)+1)*resolution))|((DriftXbinlayer3(a,b)<=((j-b)-1)*resolution)|(DriftXbinlayer3(a,b)>=-((b-j)-
1)*resolution)))
```

```
            Contribbinlayer3(a,b)=0;
        else
            Contribbinlayer3(a,b)=((abs(resolution-abs(((b-j)*-resolution)-
DriftXbinlayer3(a,b)))*abs(resolution-abs(((a-i)*resolution)-
DriftYbinlayer3(a,b))))/resolution^2)*Zbinlayer3(a,b);
        end
      end
    end
    x=1;
    y=1;
    for x=1:45
      for y=1:45
        CorrZunitbinlayer3(i,j)=CorrZunitbinlayer3(i,j)+Contribbinlayer3(x,y);
      end
    end
  end
end

%Fill the z's,Vf's, DriftX, DriftY for bin layer 4
for i=1:45
  for j=1:45
    Zbinlayer4(i,j)=(((-No(i,j))*(Lambda(i,j))*exp((-Lambda(i,j))*6.599))-((-
No(i,j))*(Lambda(i,j))*exp((-Lambda(i,j))*6.3)))*(6.4495^6);
  end
end
for i=1:45
  for j=1:45
    Vfbinlayer4(i,j)=(10.27763-W(i,j));
  end
end
for i=1:45
  for j=1:45
    DriftXbinlayer4(i,j)=(U(i,j)*height(i,j))/(2*Vfbinlayer4(i,j));
  end
end
for i=1:45
  for j=1:45
```

```
    DriftYbinlayer4(i,j)=(V(i,j)*height(i,j))/(2*Vfbinlayer4(i,j));
  end
end

%Outer loop calculates the new matrix of corrected dBZ from wind-drift
%Inner loop calculates a matrix for cell contributions to a single pixel
%Last step sums up the cell contributions to be placed in the outer loop
%corrected dBZ matrix (see notes for questions on geometry)
g=1;
h=1;
for g=1:45,
   for h=1:45,
      CorrZunitbinlayer4(g,h)=0;
   end
end
i=1;
j=1;
for i=1:45
  for j=1:45
      a=1;
      b=1;
      for a=1:45
         for b=1:45
            if(((DriftYbinlayer4(a,b)<=((a-i)-1)*resolution)|(DriftYbinlayer4(a,b)>=((a-
i)+1)*resolution))|((DriftXbinlayer4(a,b)<=((j-b)-1)*resolution)|(DriftXbinlayer4(a,b)>=-((b-j)-
1)*resolution)))
               Contribbinlayer4(a,b)=0;
            else
               Contribbinlayer4(a,b)=((abs(resolution-abs(((b-j)*-resolution)-
DriftXbinlayer4(a,b)))*abs(resolution-abs(((a-i)*resolution)-
DriftYbinlayer4(a,b))))/resolution^2)*Zbinlayer4(a,b);
            end
         end
      end
      x=1;
      y=1;
      for x=1:45
```

```
        for y=1:45
            CorrZunitbinlayer4(i,j)=CorrZunitbinlayer4(i,j)+Contribbinlayer4(x,y);
        end
      end
   end
end

%Fill the z's,Vf's, DriftX, DriftY for bin layer 5
for i=1:45
   for j=1:45
      Zbinlayer5(i,j)=(((-No(i,j))*(Lambda(i,j))*exp((-Lambda(i,j))*6.299))-((-
No(i,j))*(Lambda(i,j))*exp((-Lambda(i,j))*6.0)))*(6.1495^6);
   end
end
for i=1:45
   for j=1:45
      Vfbinlayer5(i,j)=(10.03558-W(i,j));
   end
end
for i=1:45
   for j=1:45
      DriftXbinlayer5(i,j)=(U(i,j)*height(i,j))/(2*Vfbinlayer5(i,j));
   end
end
for i=1:45
   for j=1:45
      DriftYbinlayer5(i,j)=(V(i,j)*height(i,j))/(2*Vfbinlayer5(i,j));
   end
end

%Outer loop calculates the new matrix of corrected dBZ from wind-drift
%Inner loop calculates a matrix for cell contributions to a single pixel
%Last step sums up the cell contributions to be placed in the outer loop
%corrected dBZ matrix (see notes for questions on geometry)
g=1;
h=1;
for g=1:45,
```

```
   for h=1:45,
      CorrZunitbinlayer5(g,h)=0;
   end
end
i=1;
j=1;
for i=1:45
  for j=1:45
      a=1;
      b=1;
      for a=1:45
         for b=1:45
            if(((DriftYbinlayer5(a,b)<=((a-i)-1)*resolution)|(DriftYbinlayer5(a,b)>=((a-
i)+1)*resolution))|((DriftXbinlayer5(a,b)<=((j-b)-1)*resolution)|(DriftXbinlayer5(a,b)>=-((b-j)-
1)*resolution)))
               Contribbinlayer5(a,b)=0;
            else
               Contribbinlayer5(a,b)=((abs(resolution-abs(((b-j)*-resolution)-
DriftXbinlayer5(a,b)))*abs(resolution-abs(((a-i)*resolution)-
DriftYbinlayer5(a,b))))/resolution^2)*Zbinlayer5(a,b);
            end
         end
      end
      x=1;
      y=1;
      for x=1:45
         for y=1:45
            CorrZunitbinlayer5(i,j)=CorrZunitbinlayer5(i,j)+Contribbinlayer5(x,y);
         end
      end
   end
end

%Fill the z's,Vf's, DriftX, DriftY for bin layer 6
for i=1:45
   for j=1:45
```

```
      Zbinlayer6(i,j)=(((-No(i,j))*(Lambda(i,j))*exp((-Lambda(i,j))*5.999))-((-
No(i,j))*(Lambda(i,j))*exp((-Lambda(i,j))*5.7)))*(5.8495^6);
   end
end
for i=1:45
   for j=1:45
      Vfbinlayer6(i,j)=(9.787549-W(i,j));
   end
end
for i=1:45
   for j=1:45
      DriftXbinlayer6(i,j)=(U(i,j)*height(i,j))/(2*Vfbinlayer6(i,j));
   end
end
for i=1:45
   for j=1:45
      DriftYbinlayer6(i,j)=(V(i,j)*height(i,j))/(2*Vfbinlayer6(i,j));
   end
end

%Outer loop calculates the new matrix of corrected dBZ from wind-drift
%Inner loop calculates a matrix for cell contributions to a single pixel
%Last step sums up the cell contributions to be placed in the outer loop
%corrected dBZ matrix (see notes for questions on geometry)
g=1;
h=1;
for g=1:45,
   for h=1:45,
      CorrZunitbinlayer6(g,h)=0;
   end
end
i=1;
j=1;
for i=1:45
  for j=1:45
      a=1;
      b=1;
```

```
      for a=1:45
         for b=1:45
            if(((DriftYbinlayer6(a,b)<=((a-i)-1)*resolution)|(DriftYbinlayer6(a,b)>=((a-
i)+1)*resolution))|((DriftXbinlayer6(a,b)<=((j-b)-1)*resolution)|(DriftXbinlayer6(a,b)>=-((b-j)-
1)*resolution)))
               Contribbinlayer6(a,b)=0;
            else
               Contribbinlayer6(a,b)=((abs(resolution-abs(((b-j)*-resolution)-
DriftXbinlayer6(a,b)))*abs(resolution-abs(((a-i)*resolution)-
DriftYbinlayer6(a,b))))/resolution^2)*Zbinlayer6(a,b);
            end
         end
      end
      x=1;
      y=1;
      for x=1:45
         for y=1:45
            CorrZunitbinlayer6(i,j)=CorrZunitbinlayer6(i,j)+Contribbinlayer6(x,y);
         end
      end
   end
end

%Fill the z's,Vf's, DriftX, DriftY for bin layer 7
for i=1:45
   for j=1:45
      Zbinlayer7(i,j)=(((-No(i,j))*(Lambda(i,j))*exp((-Lambda(i,j))*5.699))-((-
No(i,j))*(Lambda(i,j))*exp((-Lambda(i,j))*5.4)))*(5.5495^6);
   end
end
for i=1:45
   for j=1:45
      Vfbinlayer7(i,j)=(9.533064-W(i,j));
   end
end
for i=1:45
   for j=1:45
```

```
      DriftXbinlayer7(i,j)=(U(i,j)*height(i,j))/(2*Vfbinlayer7(i,j));
   end
end
for i=1:45
   for j=1:45
      DriftYbinlayer7(i,j)=(V(i,j)*height(i,j))/(2*Vfbinlayer7(i,j));
   end
end

%Outer loop calculates the new matrix of corrected dBZ from wind-drift
%Inner loop calculates a matrix for cell contributions to a single pixel
%Last step sums up the cell contributions to be placed in the outer loop
%corrected dBZ matrix (see notes for questions on geometry)
g=1;
h=1;
for g=1:45,
   for h=1:45,
      CorrZunitbinlayer7(g,h)=0;
   end
end
i=1;
j=1;
for i=1:45
  for j=1:45
      a=1;
      b=1;
      for a=1:45
         for b=1:45
            if(((DriftYbinlayer7(a,b)<=((a-i)-1)*resolution)|(DriftYbinlayer7(a,b)>=((a-
i)+1)*resolution))|((DriftXbinlayer7(a,b)<=((j-b)-1)*resolution)|(DriftXbinlayer7(a,b)>=-((b-j)-
1)*resolution)))
               Contribbinlayer7(a,b)=0;
            else
               Contribbinlayer7(a,b)=((abs(resolution-abs(((b-j)*-resolution)-
DriftXbinlayer7(a,b)))*abs(resolution-abs(((a-i)*resolution)-
DriftYbinlayer7(a,b))))/resolution^2)*Zbinlayer7(a,b);
            end
```

```
        end
      end
      x=1;
      y=1;
      for x=1:45
        for y=1:45
          CorrZunitbinlayer7(i,j)=CorrZunitbinlayer7(i,j)+Contribbinlayer7(x,y);
        end
      end
  end
end

%Fill the z's,Vf's, DriftX, DriftY for bin layer 8
for i=1:45
  for j=1:45
    Zbinlayer8(i,j)=(((-No(i,j))*(Lambda(i,j))*exp((-Lambda(i,j))*5.399))-((-
No(i,j))*(Lambda(i,j))*exp((-Lambda(i,j))*5.1)))*(5.2495^6);
  end
end
for i=1:45
  for j=1:45
    Vfbinlayer8(i,j)=(9.271595-W(i,j));
  end
end
for i=1:45
  for j=1:45
    DriftXbinlayer8(i,j)=(U(i,j)*height(i,j))/(2*Vfbinlayer8(i,j));
  end
end
for i=1:45
  for j=1:45
    DriftYbinlayer8(i,j)=(V(i,j)*height(i,j))/(2*Vfbinlayer8(i,j));
  end
end

%Outer loop calculates the new matrix of corrected dBZ from wind-drift
%Inner loop calculates a matrix for cell contributions to a single pixel
```

```
%Last step sums up the cell contributions to be placed in the outer loop
%corrected dBZ matrix (see notes for questions on geometry)
g=1;
h=1;
for g=1:45,
   for h=1:45,
      CorrZunitbinlayer8(g,h)=0;
   end
end
i=1;
j=1;
for i=1:45
  for j=1:45
      a=1;
      b=1;
      for a=1:45
         for b=1:45
            if(((DriftYbinlayer8(a,b)<=((a-i)-1)*resolution)|(DriftYbinlayer8(a,b)>=((a-
i)+1)*resolution))|((DriftXbinlayer8(a,b)<=((j-b)-1)*resolution)|(DriftXbinlayer8(a,b)>=-((b-j)-
1)*resolution)))
               Contribbinlayer8(a,b)=0;
            else
               Contribbinlayer8(a,b)=((abs(resolution-abs(((b-j)*-resolution)-
DriftXbinlayer8(a,b)))*abs(resolution-abs(((a-i)*resolution)-
DriftYb inlayer8(a,b))))/resolution^2)*Zbinlayer8(a,b);
            end
         end
      end
      x=1;
      y=1;
      for x=1:45
         for y=1:45
            CorrZunitbinlayer8(i,j)=CorrZunitbinlayer8(i,j)+Contribbinlayer8(x,y);
         end
      end
   end
end
```

```
%Fill the z's,Vf's, DriftX, DriftY for bin layer 9
for i=1:45
   for j=1:45
      Zbinlayer9(i,j)=(((-No(i,j))*(Lambda(i,j))*exp((-Lambda(i,j))*5.099))-((-
No(i,j))*(Lambda(i,j))*exp((-Lambda(i,j))*4.8)))*(4.9495^6);
   end
end
for i=1:45
   for j=1:45
      Vfbinlayer9(i,j)=(9.002536-W(i,j));
   end
end
for i=1:45
   for j=1:45
      DriftXbinlayer9(i,j)=(U(i,j)*height(i,j))/(2*Vfbinlayer9(i,j));
   end
end
for i=1:45
   for j=1:45
      DriftYbinlayer9(i,j)=(V(i,j)*height(i,j))/(2*Vfbinlayer9(i,j));
   end
end

%Outer loop calculates the new matrix of corrected dBZ from wind-drift
%Inner loop calculates a matrix for cell contributions to a single pixel
%Last step sums up the cell contributions to be placed in the outer loop
%corrected dBZ matrix (see notes for questions on geometry)
g=1;
h=1;
for g=1:45,
   for h=1:45,
      CorrZunitbinlayer9(g,h)=0;
   end
end
i=1;
j=1;
```

```
for i=1:45
  for j=1:45
      a=1;
      b=1;
      for a=1:45
         for b=1:45
            if(((DriftYbinlayer9(a,b)<=((a-i)-1)*resolution)|(DriftYbinlayer9(a,b)>=((a-
i)+1)*resolution))|((DriftXbinlayer9(a,b)<=((j-b)-1)*resolution)|(DriftXbinlayer9(a,b)>=-((b-j)-
1)*resolution)))
               Contribbinlayer9(a,b)=0;
            else
               Contribbinlayer9(a,b)=((abs(resolution-abs(((b-j)*-resolution)-
DriftXbinlayer9(a,b)))*abs(resolution-abs(((a-i)*resolution)-
DriftYbinlayer9(a,b))))/resolution^2)*Zbinlayer9(a,b);
            end
         end
      end
      x=1;
      y=1;
      for x=1:45
         for y=1:45
            CorrZunitbinlayer9(i,j)=CorrZunitbinlayer9(i,j)+Contribbinlayer9(x,y);
         end
      end
   end
end

%Fill the z's,Vf's, DriftX, DriftY for bin layer 10
for i=1:45
   for j=1:45
      Zbinlayer10(i,j)=(((-No(i,j))*(Lambda(i,j))*exp((-Lambda(i,j))*4.799))-((-
No(i,j))*(Lambda(i,j))*exp((-Lambda(i,j))*4.5)))*(4.6495^6);
   end
end
for i=1:45
   for j=1:45
      Vfbinlayer10(i,j)=(8.725184-W(i,j));
```

```
   end
end
for i=1:45
   for j=1:45
      DriftXbinlayer10(i,j)=(U(i,j)*height(i,j))/(2*Vfbinlayer10(i,j));
   end
end
for i=1:45
   for j=1:45
      DriftYbinlayer10(i,j)=(V(i,j)*height(i,j))/(2*Vfbinlayer10(i,j));
   end
end

%Outer loop calculates the new matrix of corrected dBZ from wind-drift
%Inner loop calculates a matrix for cell contributions to a single pixel
%Last step sums up the cell contributions to be placed in the outer loop
%corrected dBZ matrix (see notes for questions on geometry)
g=1;
h=1;
for g=1:45,
   for h=1:45,
      CorrZunitbinlayer10(g,h)=0;
   end
end
i=1;
j=1;
for i=1:45
  for j=1:45
      a=1;
      b=1;
      for a=1:45
         for b=1:45
            if(((DriftYbinlayer10(a,b)<=((a-i)-1)*resolution)|(DriftYbinlayer10(a,b)>=((a-
i)+1)*resolution))|((DriftXbinlayer10(a,b)<=((j-b)-1)*resolution)|(DriftXbinlayer10(a,b)>=-((b-j)-
1)*resolution)))
               Contribbinlayer10(a,b)=0;
            else
```

```
            Contribbinlayer10(a,b)=((abs(resolution-abs(((b-j)*-resolution)-
DriftXbinlayer10(a,b)))*abs(resolution-abs(((a-i)*resolution)-
DriftYbinlayer10(a,b))))/resolution^2)*Zbinlayer10(a,b);
          end
        end
      end
      x=1;
      y=1;
      for x=1:45
        for y=1:45
          CorrZunitbinlayer10(i,j)=CorrZunitbinlayer10(i,j)+Contribbinlayer10(x,y);
        end
      end
  end
end

%Fill the z's,Vf's, DriftX, DriftY for bin layer 11
for i=1:45
  for j=1:45
    Zbinlayer11(i,j)=(((-No(i,j))*(Lambda(i,j))*exp((-Lambda(i,j))*4.499))-((-
No(i,j))*(Lambda(i,j))*exp((-Lambda(i,j))*4.2)))*(4.3495^6);
  end
end
for i=1:45
  for j=1:45
    Vfbinlayer11(i,j)=(8.438721-W(i,j));
  end
end
for i=1:45
  for j=1:45
    DriftXbinlayer11(i,j)=(U(i,j)*height(i,j))/(2*Vfbinlayer11(i,j));
  end
end
for i=1:45
  for j=1:45
    DriftYbinlayer11(i,j)=(V(i,j)*height(i,j))/(2*Vfbinlayer11(i,j));
  end
```

```
end

%Outer loop calculates the new matrix of corrected dBZ from wind-drift
%Inner loop calculates a matrix for cell contributions to a single pixel
%Last step sums up the cell contributions to be placed in the outer loop
%corrected dBZ matrix (see notes for questions on geometry)
g=1;
h=1;
for g=1:45,
   for h=1:45,
      CorrZunitbinlayer11(g,h)=0;
   end
end
i=1;
j=1;
for i=1:45
  for j=1:45
      a=1;
      b=1;
      for a=1:45
         for b=1:45
            if(((DriftYbinlayer11(a,b)<=((a-i)-1)*resolution)|(DriftYbinlayer11(a,b)>=((a-
i)+1)*resolution))|((DriftXbinlayer11(a,b)<=((j-b)-1)*resolution)|(DriftXbinlayer11(a,b)>=-((b-j)-
1)*resolution)))
               Contribbinlayer11(a,b)=0;
            else
               Contribbinlayer11(a,b)=((abs(resolution-abs(((b-j)*-resolution)-
DriftXbinlayer11(a,b)))*abs(resolution-abs(((a-i)*resolution)-
DriftYbinlayer11(a,b))))/resolution^2)*Zbinlayer11(a,b);
            end
         end
      end
      x=1;
      y=1;
      for x=1:45
         for y=1:45
            CorrZunitbinlayer11(i,j)=CorrZunitbinlayer11(i,j)+Contribbinlayer11(x,y);
```

```
        end
      end
   end
end

%Fill the z's,Vf's, DriftX, DriftY for bin layer 12
for i=1:45
   for j=1:45
      Zbinlayer12(i,j)=(((-No(i,j))*(Lambda(i,j))*exp((-Lambda(i,j))*4.199))-((-
No(i,j))*(Lambda(i,j))*exp((-Lambda(i,j))*3.9)))*(4.0495^6);
   end
end
for i=1:45
   for j=1:45
      Vfbinlayer12(i,j)=(8.142185-W(i,j));
   end
end
for i=1:45
   for j=1:45
      DriftXbinlayer12(i,j)=(U(i,j)*height(i,j))/(2*Vfbinlayer12(i,j));
   end
end
for i=1:45
   for j=1:45
      DriftYbinlayer12(i,j)=(V(i,j)*height(i,j))/(2*Vfbinlayer12(i,j));
   end
end

%Outer loop calculates the new matrix of corrected dBZ from wind-drift
%Inner loop calculates a matrix for cell contributions to a single pixel
%Last step sums up the cell contributions to be placed in the outer loop
%corrected dBZ matrix (see notes for questions on geometry)
g=1;
h=1;
for g=1:45,
   for h=1:45,
      CorrZunitbinlayer12(g,h)=0;
```

```
   end
end
i=1;
j=1;
for i=1:45
  for j=1:45
      a=1;
      b=1;
      for a=1:45
         for b=1:45
            if(((DriftYbinlayer12(a,b)<=((a-i)-1)*resolution)|(DriftYbinlayer12(a,b)>=((a-
i)+1)*resolution))|((DriftXbinlayer12(a,b)<=((j-b)-1)*resolution)|(DriftXbinlayer12(a,b)>=-((b-j)-
1)*resolution)))
               Contribbinlayer12(a,b)=0;
            else
               Contribbinlayer12(a,b)=((abs(resolution-abs(((b-j)*-resolution)-
DriftXbinlayer12(a,b)))*abs(resolution-abs(((a-i)*resolution)-
DriftYbinlayer12(a,b))))/resolution^2)*Zbinlayer12(a,b);
            end
         end
      end
      x=1;
      y=1;
      for x=1:45
         for y=1:45
            CorrZunitbinlayer12(i,j)=CorrZunitbinlayer12(i,j)+Contribbinlayer12(x,y);
         end
      end
  end
end

%Fill the z's,Vf's, DriftX, DriftY for bin layer 13
for i=1:45
   for j=1:45
      Zbinlayer13(i,j)=(((-No(i,j))*(Lambda(i,j))*exp((-Lambda(i,j))*3.899))-((-
No(i,j))*(Lambda(i,j))*exp((-Lambda(i,j))*3.6)))*(3.7495^6);
   end
```

```
end
for i=1:45
   for j=1:45
      Vfbinlayer13(i,j)=(7.834434-W(i,j));
   end
end
for i=1:45
   for j=1:45
      DriftXbinlayer13(i,j)=(U(i,j)*height(i,j))/(2*Vfbinlayer13(i,j));
   end
end
for i=1:45
   for j=1:45
      DriftYbinlayer13(i,j)=(V(i,j)*height(i,j))/(2*Vfbinlayer13(i,j));
   end
end

%Outer loop calculates the new matrix of corrected dBZ from wind-drift
%Inner loop calculates a matrix for cell contributions to a single pixel
%Last step sums up the cell contributions to be placed in the outer loop
%corrected dBZ matrix (see notes for questions on geometry)
g=1;
h=1;
for g=1:45,
   for h=1:45,
      CorrZunitbinlayer13(g,h)=0;
   end
end
i=1;
j=1;
for i=1:45
  for j=1:45
      a=1;
      b=1;
      for a=1:45
         for b=1:45
```

```
            if(((DriftYbinlayer13(a,b)<=((a-i)-1)*resolution)|(DriftYbinlayer13(a,b)>=((a-
i)+1)*resolution))|((DriftXbinlayer13(a,b)<=((j-b)-1)*resolution)|(DriftXbinlayer13(a,b)>=-((b-j)-
1)*resolution)))
                Contribbinlayer13(a,b)=0;
            else
                Contribbinlayer13(a,b)=((abs(resolution-abs(((b-j)*-resolution)-
DriftXbinlayer13(a,b)))*abs(resolution-abs(((a-i)*resolution)-
DriftYbinlayer13(a,b))))/resolution^2)*Zbinlayer13(a,b);
            end
          end
       end
       x=1;
       y=1;
       for x=1:45
          for y=1:45
             CorrZunitbinlayer13(i,j)=CorrZunitbinlayer13(i,j)+Contribbinlayer13(x,y);
          end
       end
    end
end

%Fill the z's,Vf's, DriftX, DriftY for bin layer 14
for i=1:45
    for j=1:45
       Zbinlayer14(i,j)=(((-No(i,j))*(Lambda(i,j))*exp((-Lambda(i,j))*3.599))-((-
No(i,j))*(Lambda(i,j))*exp((-Lambda(i,j))*3.3)))*(3.4495^6);
    end
end
for i=1:45
    for j=1:45
       Vfbinlayer14(i,j)=(7.514089-W(i,j));
    end
end
for i=1:45
    for j=1:45
       DriftXbinlayer14(i,j)=(U(i,j)*height(i,j))/(2*Vfbinlayer14(i,j));
    end
```

```
end
for i=1:45
   for j=1:45
      DriftYbinlayer14(i,j)=(V(i,j)*height(i,j))/(2*Vfbinlayer14(i,j));
   end
end

%Outer loop calculates the new matrix of corrected dBZ from wind-drift
%Inner loop calculates a matrix for cell contributions to a single pixel
%Last step sums up the cell contributions to be placed in the outer loop
%corrected dBZ matrix (see notes for questions on geometry)
g=1;
h=1;
for g=1:45,
   for h=1:45,
      CorrZunitbinlayer14(g,h)=0;
   end
end
i=1;
j=1;
for i=1:45
  for j=1:45
      a=1;
      b=1;
      for a=1:45
         for b=1:45
            if(((DriftYbinlayer14(a,b)<=((a-i)-1)*resolution)|(DriftYbinlayer14(a,b)>=((a-
i)+1)*resolution))|((DriftXbinlayer14(a,b)<=((j-b)-1)*resolution)|(DriftXbinlayer14(a,b)>=-((b-j)-
1)*resolution)))
               Contribbinlayer14(a,b)=0;
            else
               Contribbinlayer14(a,b)=((abs(resolution-abs(((b-j)*-resolution)-
DriftXbinlayer14(a,b)))*abs(resolution-abs(((a-i)*resolution)-
DriftYbinlayer14(a,b))))/resolution^2)*Zbinlayer14(a,b);
            end
         end
      end
```

```
      x=1;
      y=1;
      for x=1:45
        for y=1:45
          CorrZunitbinlayer14(i,j)=CorrZunitbinlayer14(i,j)+Contribbinlayer14(x,y);
        end
      end
  end
end

%Fill the z's,Vf's, DriftX, DriftY for bin layer 15
for i=1:45
   for j=1:45
     Zbinlayer15(i,j)=(((-No(i,j))*(Lambda(i,j))*exp((-Lambda(i,j))*3.299))-((-
No(i,j))*(Lambda(i,j))*exp((-Lambda(i,j))*3.00)))*(3.1495^6);
  end
end
for i=1:45
   for j=1:45
     Vfbinlayer15(i,j)=(7.179464-W(i,j));
  end
end
for i=1:45
   for j=1:45
     DriftXbinlayer15(i,j)=(U(i,j)*height(i,j))/(2*Vfbinlayer15(i,j));
  end
end
for i=1:45
   for j=1:45
     DriftYbinlayer15(i,j)=(V(i,j)*height(i,j))/(2*Vfbin layer15(i,j));
  end
end

%Outer loop calculates the new matrix of corrected dBZ from wind-drift
%Inner loop calculates a matrix for cell contributions to a single pixel
%Last step sums up the cell contributions to be placed in the outer loop
%corrected dBZ matrix (see notes for questions on geometry)
```

```
g=1;
h=1;
for g=1:45,
   for h=1:45,
      CorrZunitbinlayer15(g,h)=0;
   end
end
i=1;
j=1;
for i=1:45
  for j=1:45
      a=1;
      b=1;
      for a=1:45
         for b=1:45
            if(((DriftYbinlayer15(a,b)<=((a-i)-1)*resolution)|(DriftYbinlayer15(a,b)>=((a-
i)+1)*resolution))|((DriftXbinlayer15(a,b)<=((j-b)-1)*resolution)|(DriftXbinlayer15(a,b)>=-((b-j)-
1)*resolution)))
               Contribbinlayer15(a,b)=0;
            else
               Contribbinlayer15(a,b)=((abs(resolution-abs(((b-j)*-resolution)-
DriftXbinlayer15(a,b)))*abs(resolution-abs(((a-i)*resolution)-
DriftYbinlayer15(a,b))))/resolution^2)*Zbinlayer15(a,b);
            end
         end
      end
      x=1;
      y=1;
      for x=1:45
         for y=1:45
            CorrZunitbinlayer15(i,j)=CorrZunitbinlayer15(i,j)+Contribbinlayer15(x,y);
         end
      end
   end
end

%Fill the z's,Vf's, DriftX, DriftY for bin layer 16
```

```
for i=1:45
   for j=1:45
      Zbinlayer16(i,j)=(((-No(i,j))*(Lambda(i,j))*exp((-Lambda(i,j))*2.999))-((-
No(i,j))*(Lambda(i,j))*exp((-Lambda(i,j))*2.7)))*(2.8495^6);
   end
end
for i=1:45
   for j=1:45
      Vfbinlayer16(i,j)=(6.828461-W(i,j));
   end
end
for i=1:45
   for j=1:45
      DriftXbinlayer16(i,j)=(U(i,j)*height(i,j))/(2*Vfbinlayer16(i,j));
   end
end
for i=1:45
   for j=1:45
      DriftYbinlayer16(i,j)=(V(i,j)*height(i,j))/(2*Vfbinlayer16(i,j));
   end
end

%Outer loop calculates the new matrix of corrected dBZ from wind-drift
%Inner loop calculates a matrix for cell contributions to a single pixel
%Last step sums up the cell contributions to be placed in the outer loop
%corrected dBZ matrix (see notes for questions on geometry)
g=1;
h=1;
for g=1:45,
   for h=1:45,
      CorrZunitbinlayer16(g,h)=0;
   end
end
i=1;
j=1;
for i=1:45
  for j=1:45
```

```
      a=1;
      b=1;
      for a=1:45
         for b=1:45
            if(((DriftYbinlayer16(a,b)<=((a-i)-1)*resolution)|(DriftYbinlayer16(a,b)>=((a-
i)+1)*resolution))|((DriftXbinlayer16(a,b)<=((j-b)-1)*resolution)|(DriftXbinlayer16(a,b)>=-((b-j)-
1)*resolution)))
               Contribbinlayer16(a,b)=0;
            else
               Contribbinlayer16(a,b)=((abs(resolution-abs(((b-j)*-resolution)-
DriftXbinlayer16(a,b)))*abs(resolution-abs(((a-i)*resolution)-
DriftYbinlayer16(a,b))))/resolution^2)*Zbinlayer16(a,b);
            end
         end
      end
      x=1;
      y=1;
      for x=1:45
         for y=1:45
            CorrZunitbinlayer16(i,j)=CorrZunitbinlayer16(i,j)+Contribbinlayer16(x,y);
         end
      end
   end
end

%Fill the z's,Vf's, DriftX, DriftY for bin layer 17
for i=1:45
   for j=1:45
      Zbinlayer17(i,j)=(((-No(i,j))*(Lambda(i,j))*exp((-Lambda(i,j))*2.699))-((-
No(i,j))*(Lambda(i,j))*exp((-Lambda(i,j))*2.4)))*(2.5495^6);
   end
end
for i=1:45
   for j=1:45
      Vfbinlayer17(i,j)=(6.45841-W(i,j));
   end
end
```

```
for i=1:45
   for j=1:45
      DriftXbinlayer17(i,j)=(U(i,j)*height(i,j))/(2*Vfbinlayer17(i,j));
   end
end
for i=1:45
   for j=1:45
      DriftYbinlayer17(i,j)=(V(i,j)*height(i,j))/(2*Vfbinlayer17(i,j));
   end
end

%Outer loop calculates the new matrix of corrected dBZ from wind-drift
%Inner loop calculates a matrix for cell contributions to a single pixel
%Last step sums up the cell contributions to be placed in the outer loop
%corrected dBZ matrix (see notes for questions on geometry)
g=1;
h=1;
for g=1:45,
   for h=1:45,
      CorrZunitbinlayer17(g,h)=0;
   end
end
i=1;
j=1;
for i=1:45
  for j=1:45
      a=1;
      b=1;
      for a=1:45
         for b=1:45
            if(((DriftYbinlayer17(a,b)<=((a-i)-1)*resolution)|(DriftYbinlayer17(a,b)>=((a-
i)+1)*resolution))|((DriftXbinlayer17(a,b)<=((j-b)-1)*resolution)|(DriftXbinlayer17(a,b)>=-((b-j)-
1)*resolution)))
               Contribbinlayer17(a,b)=0;
            else
```

```
                Contribbinlayer17(a,b)=((abs(resolution-abs(((b-j)*-resolution)-
DriftXbinlayer17(a,b)))*abs(resolution-abs(((a-i)*resolution)-
DriftYbinlayer17(a,b))))/resolution^2)*Zbinlayer17(a,b);
            end
          end
        end
        x=1;
        y=1;
        for x=1:45
          for y=1:45
            CorrZunitbinlayer17(i,j)=CorrZunitbinlayer17(i,j)+Contribbinlayer17(x,y);
          end
        end
    end
end

%Fill the z's,Vf's, DriftX, DriftY for bin layer 18
for i=1:45
    for j=1:45
      Zbinlayer18(i,j)=(((-No(i,j))*(Lambda(i,j))*exp((-Lambda(i,j))*2.399))-((-
No(i,j))*(Lambda(i,j))*exp((-Lambda(i,j))*2.1)))*(2.2495^6);
    end
end
for i=1:45
    for j=1:45
       Vfbinlayer18(i,j)=(6.065825-W(i,j));
    end
end
for i=1:45
    for j=1:45
      DriftXbinlayer18(i,j)=(U(i,j)*height(i,j))/(2*Vfbinlayer18(i,j));
    end
end
for i=1:45
    for j=1:45
      DriftYbinlayer18(i,j)=(V(i,j)*height(i,j))/(2*Vfbinlayer18(i,j));
    end
```

```
end

%Outer loop calculates the new matrix of corrected dBZ from wind-drift
%Inner loop calculates a matrix for cell contributions to a single pixel
%Last step sums up the cell contributions to be placed in the outer loop
%corrected dBZ matrix (see notes for questions on geometry)
g=1;
h=1;
for g=1:45,
   for h=1:45,
      CorrZunitbinlayer18(g,h)=0;
   end
end
i=1;
j=1;
for i=1:45
  for j=1:45
      a=1;
      b=1;
      for a=1:45
         for b=1:45
            if(((DriftYbinlayer18(a,b)<=((a-i)-1)*resolution)|(DriftYbinlayer18(a,b)>=((a-
i)+1)*resolution))|((DriftXbinlayer18(a,b)<=((j-b)-1)*resolution)|(DriftXbinlayer18(a,b)>=-((b-j)-
1)*resolution)))
               Contribbinlayer18(a,b)=0;
            else
               Contribbinlayer18(a,b)=((abs(resolution-abs(((b-j)*-resolution)-
DriftXbinlayer18(a,b)))*abs(resolution-abs(((a-i)*resolution)-
DriftYbinlayer18(a,b))))/resolution^2)*Zbinlayer18(a,b);
            end
         end
      end
      x=1;
      y=1;
      for x=1:45
         for y=1:45
            CorrZunitbinlayer18(i,j)=CorrZunitbinlayer18(i,j)+Contribbinlayer18(x,y);
```

```
        end
      end
   end
end

%Fill the z's,Vf's, DriftX, DriftY for bin layer 19
for i=1:45
   for j=1:45
      Zbinlayer19(i,j)=(((-No(i,j))*(Lambda(i,j))*exp((-Lambda(i,j))*2.099))-((-
No(i,j))*(Lambda(i,j))*exp((-Lambda(i,j))*1.8)))*(1.9495^6);
   end
end
for i=1:45
   for j=1:45
      Vfbinlayer19(i,j)=(5.646008-W(i,j));
   end
end
for i=1:45
   for j=1:45
      DriftXbinlayer19(i,j)=(U(i,j)*height(i,j))/(2*Vfbinlayer19(i,j));
   end
end
for i=1:45
   for j=1:45
      DriftYbinlayer19(i,j)=(V(i,j)*height(i,j))/(2*Vfbinlayer19(i,j));
   end
end

%Outer loop calculates the new matrix of corrected dBZ from wind-drift
%Inner loop calculates a matrix for cell contributions to a single pixel
%Last step sums up the cell contributions to be placed in the outer loop
%corrected dBZ matrix (see notes for questions on geometry)
g=1;
h=1;
for g=1:45,
   for h=1:45,
      CorrZunitbinlayer19(g,h)=0;
```

```
   end
end
i=1;
j=1;
for i=1:45
  for j=1:45
      a=1;
      b=1;
      for a=1:45
         for b=1:45
            if(((DriftYbinlayer19(a,b)<=((a-i)-1)*resolution)|(DriftYbinlayer19(a,b)>=((a-
i)+1)*resolution))|((DriftXbinlayer19(a,b)<=((j-b)-1)*resolution)|(DriftXbinlayer19(a,b)>=-((b-j)-
1)*resolution)))
               Contribbinlayer19(a,b)=0;
            else
               Contribbinlayer19(a,b)=((abs(resolution-abs(((b-j)*-resolution)-
DriftXbinlayer19(a,b)))*abs(resolution-abs(((a-i)*resolution)-
DriftYbinlayer19(a,b))))/resolution^2)*Zbinlayer19(a,b);
            end
         end
      end
      x=1;
      y=1;
      for x=1:45
         for y=1:45
            CorrZunitbinlayer19(i,j)=CorrZunitbinlayer19(i,j)+Contribbinlayer19(x,y);
         end
      end
   end
end

%Fill the z's,Vf's, DriftX, DriftY for bin layer 20
for i=1:45
   for j=1:45
      Zbinlayer20(i,j)=(((-No(i,j))*(Lambda(i,j))*exp((-Lambda(i,j))*1.799))-((-
No(i,j))*(Lambda(i,j))*exp((-Lambda(i,j))*1.50)))*(1.6495^6);
   end
```

```
end
for i=1:45
   for j=1:45
      Vfbinlayer20(i,j)=(5.192358-W(i,j));
   end
end
for i=1:45
   for j=1:45
      DriftXbinlayer20(i,j)=(U(i,j)*height(i,j))/(2*Vfbinlayer20(i,j));
   end
end
for i=1:45
   for j=1:45
      DriftYbinlayer20(i,j)=(V(i,j)*height(i,j))/(2*Vfbinlayer20(i,j));
   end
end

%Outer loop calculates the new matrix of corrected dBZ from wind-drift
%Inner loop calculates a matrix for cell contributions to a single pixel
%Last step sums up the cell contributions to be placed in the outer loop
%corrected dBZ matrix (see notes for questions on geometry)
g=1;
h=1;
for g=1:45,
   for h=1:45,
      CorrZunitbinlayer20(g,h)=0;
   end
end
i=1;
j=1;
for i=1:45
  for j=1:45
      a=1;
      b=1;
      for a=1:45
         for b=1:45
```

```
            if(((DriftYbinlayer20(a,b)<=((a-i)-1)*resolution)|(DriftYbinlayer20(a,b)>=((a-
i)+1)*resolution))|((DriftXbinlayer20(a,b)<=((j-b)-1)*resolution)|(DriftXbinlayer20(a,b)>=-((b-j)-
1)*resolution)))
                Contribbinlayer20(a,b)=0;
            else
                Contribbinlayer20(a,b)=((abs(resolution-abs(((b-j)*-resolution)-
DriftXbinlayer20(a,b)))*abs(resolution-abs(((a-i)*resolution)-
DriftYbinlayer20(a,b))))/resolution^2)*Zbinlayer20(a,b);
            end
          end
       end
       x=1;
       y=1;
       for x=1:45
          for y=1:45
             CorrZunitbinlayer20(i,j)=CorrZunitbinlayer20(i,j)+Contribbinlayer20(x,y);
          end
       end
    end
end

%Fill the z's,Vf's, DriftX, DriftY for bin layer 21
for i=1:45
    for j=1:45
       Zbinlayer21(i,j)=(((-No(i,j))*(Lambda(i,j))*exp((-Lambda(i,j))*1.499))-((-
No(i,j))*(Lambda(i,j))*exp((-Lambda(i,j))*1.2)))*(1.3495^6);
    end
end
for i=1:45
    for j=1:45
       Vfbinlayer21(i,j)=(4.695078-W(i,j));
    end
end
for i=1:45
    for j=1:45
       DriftXbinlayer21(i,j)=(U(i,j)*height(i,j))/(2*Vfbinlayer21(i,j));
    end
```

```
end
for i=1:45
   for j=1:45
      DriftYbinlayer21(i,j)=(V(i,j)*height(i,j))/(2*Vfbinlayer21(i,j));
   end
end

%Outer loop calculates the new matrix of corrected dBZ from wind-drift
%Inner loop calculates a matrix for cell contributions to a single pixel
%Last step sums up the cell contributions to be placed in the outer loop
%corrected dBZ matrix (see notes for questions on geometry)
g=1;
h=1;
for g=1:45,
   for h=1:45,
      CorrZunitbinlayer21(g,h)=0;
   end
end
i=1;
j=1;
for i=1:45
  for j=1:45
      a=1;
      b=1;
      for a=1:45
         for b=1:45
            if(((DriftYbinlayer21(a,b)<=((a-i)-1)*resolution)|(DriftYbinlayer21(a,b)>=((a-
i)+1)*resolution))|((DriftXbinlayer21(a,b)<=((j-b)-1)*resolution)|(DriftXbinlayer21(a,b)>=-((b-j)-
1)*resolution)))
               Contribbinlayer21(a,b)=0;
            else
               Contribbinlayer21(a,b)=((abs(resolution-abs(((b-j)*-resolution)-
DriftXbinlayer21(a,b)))*abs(resolution-abs(((a-i)*resolution)-
DriftYbinlayer21(a,b))))/resolution^2)*Zbinlayer21(a,b);
            end
         end
      end
```

```
      x=1;
      y=1;
      for x=1:45
        for y=1:45
          CorrZunitbinlayer21(i,j)=CorrZunitbinlayer21(i,j)+Contribbinlayer21(x,y);
        end
      end
  end
end

%Fill the z's,Vf's, DriftX, DriftY for bin layer 22
for i=1:45
   for j=1:45
     Zbinlayer22(i,j)=(((-No(i,j))*(Lambda(i,j))*exp((-Lambda(i,j))*1.199))-((-
No(i,j))*(Lambda(i,j))*exp((-Lambda(i,j))*0.9)))*(1.0495^6);
  end
end
for i=1:45
   for j=1:45
     Vfbinlayer22(i,j)=(4.18-W(i,j));
  end
end
for i=1:45
   for j=1:45
     DriftXbinlayer22(i,j)=(U(i,j)*height(i,j))/(2*Vfbinlayer22(i,j));
  end
end
for i=1:45
   for j=1:45
     DriftYbinlayer22(i,j)=(V(i,j)*height(i,j))/(2*Vfbinlayer22(i,j));
  end
end

%Outer loop calculates the new matrix of corrected dBZ from wind-drift
%Inner loop calculates a matrix for cell contributions to a single pixel
%Last step sums up the cell contributions to be placed in the outer loop
%corrected dBZ matrix (see notes for questions on geometry)
```

```
g=1;
h=1;
for g=1:45,
   for h=1:45,
      CorrZunitbinlayer22(g,h)=0;
   end
end
i=1;
j=1;
for i=1:45
  for j=1:45
      a=1;
      b=1;
      for a=1:45
         for b=1:45
            if(((DriftYbinlayer22(a,b)<=((a-i)-1)*resolution)|(DriftYbinlayer22(a,b)>=((a-
i)+1)*resolution))|((DriftXbinlayer22(a,b)<=((j-b)-1)*resolution)|(DriftXbinlayer22(a,b)>=-((b-j)-
1)*resolution)))
               Contribbinlayer22(a,b)=0;
            else
               Contribbinlayer22(a,b)=((abs(resolution-abs(((b-j)*-resolution)-
DriftXbinlayer22(a,b)))*abs(resolution-abs(((a-i)*resolution)-
DriftYbinlayer22(a,b))))/resolution^2)*Zbinlayer22(a,b);
            end
         end
      end
      x=1;
      y=1;
      for x=1:45
         for y=1:45
            CorrZunitbinlayer22(i,j)=CorrZunitbinlayer22(i,j)+Contribbinlayer22(x,y);
         end
      end
   end
end

%Fill the z's,Vf's, DriftX, DriftY for bin layer 23
```

```
for i=1:45
   for j=1:45
      Zbinlayer23(i,j)=(((-No(i,j))*(Lambda(i,j))*exp((-Lambda(i,j))*.899))-((-
No(i,j))*(Lambda(i,j))*exp((-Lambda(i,j))*.6)))*(.7495^6);
   end
end
for i=1:45
   for j=1:45
      Vfbinlayer23(i,j)=(2.98-W(i,j));
   end
end
for i=1:45
   for j=1:45
      DriftXbinlayer23(i,j)=(U(i,j)*height(i,j))/(2*Vfbinlayer23(i,j));
   end
end
for i=1:45
   for j=1:45
      DriftYbinlayer23(i,j)=(V(i,j)*height(i,j))/(2*Vfbinlayer23(i,j));
   end
end

%Outer loop calculates the new matrix of corrected dBZ from wind-drift
%Inner loop calculates a matrix for cell contributions to a single pixel
%Last step sums up the cell contributions to be placed in the outer loop
%corrected dBZ matrix (see notes for questions on geometry)
g=1;
h=1;
for g=1:45,
   for h=1:45,
      CorrZunitbinlayer23(g,h)=0;
   end
end
i=1;
j=1;
for i=1:45
  for j=1:45
```

```
      a=1;
      b=1;
      for a=1:45
        for b=1:45
          if(((DriftYbinlayer23(a,b)<=((a-i)-1)*resolution)|(DriftYbinlayer23(a,b)>=((a-
i)+1)*resolution))|((DriftXbinlayer23(a,b)<=((j-b)-1)*resolution)|(DriftXbinlayer23(a,b)>=-((b-j)-
1)*resolution)))
            Contribbinlayer23(a,b)=0;
          else
            Contribbinlayer23(a,b)=((abs(resolution-abs(((b-j)*-resolution)-
DriftXbinlayer23(a,b)))*abs(resolution-abs(((a-i)*resolution)-
DriftYb inlayer23(a,b))))/resolution^2)*Zbinlayer23(a,b);
          end
        end
      end
      x=1;
      y=1;
      for x=1:45
        for y=1:45
          CorrZunitbinlayer23(i,j)=CorrZunitbinlayer23(i,j)+Contribbinlayer23(x,y);
        end
      end
    end
end

%Fill the z's,Vf's, DriftX, DriftY for bin layer 24
for i=1:45
   for j=1:45
     Zbinlayer24(i,j)=(((-No(i,j))*(Lambda(i,j))*exp((-Lambda(i,j))*.599))-((-
No(i,j))*(Lambda(i,j))*exp((-Lambda(i,j))*.3)))*(.4495^6);
   end
end
for i=1:45
   for j=1:45
     Vfbinlayer24(i,j)=(1.78-W(i,j));
   end
end
```

```
for i=1:45
   for j=1:45
      DriftXbinlayer24(i,j)=(U(i,j)*height(i,j))/(2*Vfbinlayer24(i,j));
   end
end
for i=1:45
   for j=1:45
      DriftYbinlayer24(i,j)=(V(i,j)*height(i,j))/(2*Vfbinlayer24(i,j));
   end
end

%Outer loop calculates the new matrix of corrected dBZ from wind-drift
%Inner loop calculates a matrix for cell contributions to a single pixel
%Last step sums up the cell contributions to be placed in the outer loop
%corrected dBZ matrix (see notes for questions on geometry)
g=1;
h=1;
for g=1:45,
   for h=1:45,
      CorrZunitbinlayer24(g,h)=0;
   end
end
i=1;
j=1;
for i=1:45
  for j=1:45
      a=1;
      b=1;
      for a=1:45
         for b=1:45
            if(((DriftYbinlayer24(a,b)<=((a-i)-1)*resolution)|(DriftYbinlayer24(a,b)>=((a-
i)+1)*resolution))|((DriftXbinlayer24(a,b)<=((j-b)-1)*resolution)|(DriftXbinlayer24(a,b)>=-((b-j)-
1)*resolution)))
               Contribbinlayer24(a,b)=0;
            else
```

```
            Contribbinlayer24(a,b)=((abs(resolution-abs(((b-j)*-resolution)-
DriftXbinlayer24(a,b)))*abs(resolution-abs(((a-i)*resolution)-
DriftYbinlayer24(a,b))))/resolution^2)*Zbinlayer24(a,b);
          end
        end
      end
      x=1;
      y=1;
      for x=1:45
        for y=1:45
          CorrZunitbinlayer24(i,j)=CorrZunitbinlayer24(i,j)+Contribbinlayer24(x,y);
        end
      end
  end
end

%Fill the z's,Vf's, DriftX, DriftY for bin layer 25 (final bin)
for i=1:45
  for j=1:45
    Zbinlayer25(i,j)=(((-No(i,j))*(Lambda(i,j))*exp((-Lambda(i,j))*.299))-((-
No(i,j))*(Lambda(i,j))*exp((-Lambda(i,j))*0)))*(.1495^6);
  end
end
for i=1:45
  for j=1:45
    Vfbinlayer25(i,j)=(.58-W(i,j));
  end
end
for i=1:45
  for j=1:45
    DriftXbinlayer25(i,j)=(U(i,j)*height(i,j))/(2*Vfbinlayer25(i,j));
  end
end
for i=1:45
  for j=1:45
    DriftYbinlayer25(i,j)=(V(i,j)*height(i,j))/(2*Vfbinlayer25(i,j));
  end
```

```
end

%Outer loop calculates the new matrix of corrected dBZ from wind-drift
%Inner loop calculates a matrix for cell contributions to a single pixel
%Last step sums up the cell contributions to be placed in the outer loop
%corrected dBZ matrix (see notes for questions on geometry)
g=1;
h=1;
for g=1:45,
   for h=1:45,
      CorrZunitbinlayer25(g,h)=0;
   end
end
i=1;
j=1;
for i=1:45
  for j=1:45
      a=1;
      b=1;
      for a=1:45
         for b=1:45
            if(((DriftYbinlayer25(a,b)<=((a-i)-1)*resolution)|(DriftYbinlayer25(a,b)>=((a-
i)+1)*resolution))|((DriftXbinlayer25(a,b)<=((j-b)-1)*resolution)|(DriftXbinlayer25(a,b)>=-((b-j)-
1)*resolution)))
               Contribbinlayer25(a,b)=0;
            else
               Contribbinlayer25(a,b)=((abs(resolution-abs(((b-j)*-resolution)-
DriftXbinlayer25(a,b)))*abs(resolution-abs(((a-i)*resolution)-
DriftYbinlayer25(a,b))))/resolution^2)*Zbinlayer25(a,b);
            end
         end
      end
      x=1;
      y=1;
      for x=1:45
         for y=1:45
            CorrZunitbinlayer25(i,j)=CorrZunitbinlayer25(i,j)+Contribbinlayer25(x,y);
```

```
        end
      end
   end
end

%sums up each bins z-units to complete the drop-sorting scheme
for i=1:45
   for j=1:45

CorrZunitTot(i,j)=CorrZunitbinlayer1(i,j)+CorrZunitbinlayer2(i,j)+CorrZunitbinlayer3(i,j)+CorrZunitbinla
yer4(i,j)+CorrZunitbinlayer5(i,j)+CorrZunitbinlayer6(i,j)+CorrZunitbinlayer7(i,j)+CorrZunitbinlayer8(i,j)+
CorrZunitbinlayer9(i,j)+CorrZunitbinlayer10(i,j)+CorrZunitbinlayer11(i,j)+CorrZunitbinlayer12(i,j)+CorrZ
unitbinlayer13(i,j)+CorrZunitbinlayer14(i,j)+CorrZunitbinlayer15(i,j)+CorrZunitbinlayer16(i,j)+CorrZunit
binlayer17(i,j)+CorrZunitbinlayer18(i,j)+CorrZunitbinlayer19(i,j)+CorrZunitbinlayer20(i,j)+CorrZunitbinl
ayer21(i,j)+CorrZunitbinlayer22(i,j)+CorrZunitbinlayer23(i,j)+CorrZunitbinlayer24(i,j)+CorrZunitbinlayer
25(i,j);
   end
end

%displays for comparison the rainfall rates and the rounded dBZ values for
%the corrected and original data set
i=1;
j=1;
for i=1:45
   for j=1:45
      if(CorrZunitTot(i,j)<=10)
         CorrZunitTot(i,j)=0;
      end
   end
end
for i=1:45
   for j=1:45
      if(CorrZunitTot(i,j)>0)
         CorrdBZ(i,j)=(10*(log10(CorrZunitTot(i,j))));
      else
         CorrdBZ(i,j)=0;
      end
```

```
   end
end
for i=1:45
   for j=1:45
      CorrR(i,j)=(CorrZunitTot(i,j)/300)^(1/1.4);
   end
end

Error=(CorrR-OriginalR);  %instantaneous error
CorrRtotal=CorrRtotal+(CorrR .*(10/60));
Rtotal=Rtotal+(OriginalR .*(10/60));
AccumulationError=(Rtotal-CorrRtotal);

%figures

figure;
imagesc(dBZ);
caxis([0 60]);
colorbar;
title('Original dBZ h1500 r2500 11-03-00 at t-18 (dBZ)')
OriginaldBZconv(c)=getframe;

figure;
imagesc(Rtotal);
caxis([0 80]);
colorbar;
title('Original R total h1500 r2500 11-03-00 at t-18 (mm)')
OriginalRtotalconv(c)=getframe;

figure;
imagesc(CorrdBZ);
caxis([0 60]);
colorbar;
title('Corr dBZ Drop-sorting Elev 1.5 r2500 Topo 11-03-00 at t-18 (dBZ)')
CorrdBZdsconvelev15r2500topo(c)=getframe;

figure;
```

```
imagesc(CorrRtotal);
caxis([0 80]);
colorbar;
title('Corr R Total Drop-sorting Elev 1.5 r2500 Topo 11-03-00 at t-18 (mm)')
CorrRtotaldsconvelev15r2500topo(c)=getframe;

figure;
imagesc(AccumulationError);
caxis([-25 25]);
colorbar;
title('Accum Error Drop-sorting Elev 1.5 r2500 Topo 11-03-00 at t-18 (mm)')
accumerrordsconvelev15r2500topo(c)=getframe;
end

%generates movie

movie(OriginaldBZconv);
movie2avi(OriginaldBZconv,'OriginaldBZconv.avi','fps',5,'quality',100);

movie(OriginalRtotalconv);
movie2avi(OriginalRtotalconv,'OriginalRtotalconv.avi','fps',5,'quality',100);

movie(CorrdBZdsconvelev15r2500topo);
movie2avi(CorrdBZdsconvelev15r2500topo,'CorrdBZdsconvelev15r2500topo.avi','fps',5,'quality',100);

movie(CorrRtotaldsconvelev15r2500topo);
movie2avi(CorrRtotaldsconvelev15r2500topo,'CorrRtotaldsconvelev15r2500topo.avi','fps',5,'quality',100);

movie(accumerrordsconvelev15r2500topo);
movie2avi(accumerrordsconvelev15r2500topo,'accumerrordsconvelev15r2500topo.avi','fps',5,'quality',100)
;

%Creates figure for beam height
figure;
imagesc(height);
colorbar;
title('Height (m)');
```

# References


Atlas, D. and V.G. Plank, 1953: Drop-size history during a shower. *J. Meteor.,* **10**, 291-295.

Austin, P.M., 1987: Relationship between measured radar reflectivity and surface rainfall. *Mon. Wea. Rev.*, **115**, 1053-1070.

_____and A. Bemis, 1950: A quantitative study of the bright band in radar precipitation echoes. *J. Meteor.,* **7**, 165-171.

Biggerstaff, M.I. and S.A. Listemaa, 2000: An improved scheme for convective/stratiform echo classification using radar reflectivity. *J. Appl. Meteor.*, **39**, 2129–2150.

Collier, C.G., 1985: Remote sensing for hydrological forecasting. *Facets of Hydrology*, vol. II, ed. J.C. Rodda, Wiley, Chichester, 1-24.

_____, 1996: *Applications of Weather Radar Systems: A Guide to Uses of Radar Data in Meteorology and Hydrology*, 2nd ed., John Wiley and Sons, Chichester, 390 pp.

_____, 1999: The impact of wind-drift on the utility of very high spatial resolution radar data over urban areas. *Phys. Chem. Earth(B)*, **24**, 889-893.

Courtier P., J. Derber, R. Errico, J. Louis, and T. Vukicevic, 1993: Important literature on the use of adjoint, variational methods, and the Kalman filter in meteorology. *Tellus*, **45A**, 342-357.

Crook, N.A. and J. Sun, 2004: Analysis and forecasting of the low-level wind during the Sydney 2000 Forecast Demonstration Project. *Wea. Forecasting*, **19**, 151-167.

Etter, D.M. and D.C. Kuncicky, 1999: *Introduction to Matlab*. Prentice-Hall, Inc., Upper Saddle River, 128 pp.

Fabry, F., 2004: Obstacles to the greater use of weather radar information. *Preprints, 6th International Symposium on Hydrological Applications of Weather Radar.* Melbourne, Australia, 2-4 February 2004.

_____and I. Zawadzki, 1995: Long-term radar observations of the melting layer of precipitation and their interpretation. *J. Atmos. Sci.*, **52**, 838-851.

Gorgucci, E., V. Chandrasekar, V. N. Bringi, and G. Scarchilli, 2002: Estimation of raindrop-size distribution parameters from polarimetric radar measurements. *J. Atmos. Sci.*, **59**, 2373–2384.

Gourley, J.J. and C.M. Calvert, 2003: Automated detection of the bright band using WSR-88D data. *Wea. Forecasting*, **18**, 585-599.

Gunn, R.E.S. and J.S. Marshall, 1955: The effect of wind drift on falling precipitation. *J. Atmos. Sci.*, **12**, 339–349.

Haggett, C.M., 1988: Thunderstorms over north-west London—8 May 1988, *Weather*, **43**, 266-267.

Handmer, J.W., 1987: The flood problem in perspective. *Flood Hazard Management, British and International Perspectives*, Ed. J. Handmer, Geo. Books, Norwich, 9-32.

Hubbert, J., V. Chandrasekar, V.N. Bringi, P. Meischner, 1993: Processing and Interpretation of coherent dual-polarized radar measurements. *J. Atmos. Oceanic Technol.*, **10**, 155–164.

Keenan, T., P. Joe, J. Wilson, C. Collier, B. Golding, D. Burgess, P. May, C. Pierce, J. Bally, A. Crook, A. Seed, D. Sills, L. Berry, R. Potts, I. Bell, N. Fox, E. Ebert, M. Eilts, K. O'Loughlin, R. Webb, R. Carbone, K. Browning, R. Roberts, and C. Mueller, 2003: The Sydney 2000 World Weather Research Programme Forecast Demonstration Project: overview and current status. *Bull. Amer. Meteor. Soc.*, **84**, 1041-1054.

Lacy, R., 1977: Climate and Building in Britain, *Building Research Establishment Report*, Department of the Environment, Her Majesty's Stationary Office, London.

Lhermitte, R.M., 1970: Dual-Doppler radar observation of convective storm circulation. *Preprints, 14th Radar Meteorology Conference*, Boston, Amer. Meteor. Soc., 218-223.

Marshall, J. S. and W. McK. Palmer, 1948: The distribution of raindrops with size. *J. Meteor.*, **5**, 165-166.

Matrosov, S.Y., K.A. Clark, B.E. Martner, A. Tokay, 2002: X-band polarimetric radar measurements of rainfall. *J. Appl. Meteor.*, **41**, 941–952.

Matrosov, S.Y., R.A. Kropfli, R.F. Reinking, B.E. Martner, 1999: Prospects for measuring rainfall using propagation differential phase in X- and $K_a$-radar bands. *J. Appl. Meteor.*, **38,** 766–776.

National Weather Service (NWS), 2004: *Turn Around Don't Drown Homepage*. http://www.srh.noaa.gov/tadd.

NWFO WSR-88D Operations Memorandum, 1999: *Recommended Parameter Changes to Improve WSR-88D Rainfall Estimates During Cool Season Stratiform Rain Events*, prepared by WSR-88D OSF Chief James D. Belville, http://www.roc.noaa.gov/ops/z2r_osf5.asp.

Oya, M. and S. Haruyuma, 1987: Flooding and urbanisation in the lowlands of Tokyo and vicinity, *National Disaster Sci.*, **9,** 1-21.

Reed, D.W., 1984: A review of the British flood forecasting practice. Institute of Hydrology Report No. 90, 113 pp.

Rinehart, R.E., 1997: *Radar for Meteorologists*, 3rd ed., Rinehart Publications, Grand Forks, ND, 427 pp.

Rogers and Yau, 1989: *A Short Course in Cloud Physics*, 3rd ed., Butterworth-Heinemann, Woburn, MA, 290 pp.

Rosenfeld, D., D. Atlas, D.B. Wolff, and E. Amitai, 1992: Beamwidth effects on Z-R relationships and area-integrated rainfall, *J. Appl. Meteor.*, **31**, 454-464.

Sills, D.M., J.W. Wilson, P.I. Joe, D.W. Burgess, R.M. Webb, and N.I. Fox, 2004: The 3 November tornadic event during Sydney 2000: Storm evolution and low-level boundaries. *Wea. Forecasting*, **19**, 22-42.

Sleigh, M.W., 2002: Analysis of a conceptual model-based nowcasting system. The performance and improvement of the GANDOLF system based on its performance during the Sydney 2000 Olympic Games. Ph.D. Thesis, Telford Institute of Environmental Systems, University of Salford, UK.

Smith, C.J., 1986: The reduction of errors caused by bright bands in quantitative rainfall measurements made using radar. *J. Atmos. Oceanic Technol.*, **3**, 129-141.

Sun, J. and N.A. Crook, 1994: Wind and thermodynamic retrieval from single Doppler measurements of a gust front observed during PHOENIX II. *Mon. Wea. Rev.,* **122**, 1075-1091.

Tutison, B., D. Harris, and E. Foufoula-Georgiou, 2001: Scale issues in verification of precipitation forecasts. *J. Geophys. Res.*, **106**, 11775-11784.

United States Geological Survey (USGS), 2000: *USGS Fact Sheet 024-00*. http://ks.water.usgs.gov/Kansas/pubs/fact-sheets/fs.024-00.html.

Vieux, B.E. and P.B. Bedient, 1998: Estimation of rainfall or flood prediction from WSR-88D reflectivity: a case study, 17-18 October 1994*, W*ea. Forecasting*, **13**, pp. 407-415.

Zrnic, D.S., 1987: Three-body scattering produces precipitation signature of a special diagnostic value. *Radio Sci.*, **22**, 76-86.

# Vita Auctoris

Steven Andrew Lack was born on 25 February 1979 at Southwest General Hospital in Middleburg Heights, Ohio to Jerry and Jody Lack. Along with an older sister, Nicole (now of Roseville, California), the family lived in North Ridgeville, Ohio where the author's parents still reside.

Unlike most meteorologists, no single moment sparked the idea of studying weather as a career for Steven. It was the collective experiences of watching thunderstorms throughout the summer in the neighborhood or going up to Lake Erie to watch storms move onshore. Following graduation from North Ridgeville High School in June of 1997, the author enrolled in The Pennsylvania State University to study meteorology. In December of 2001, Steven graduated and left Happy Valley with a Bachelor of Science degree.

After taking, what amounted to, a semester off after graduation, a graduate research position at the University of Missouri-Columbia opened up in the summer of 2002. The author began work towards a Master of Science degree within the Radar-Hydrology Group in the Atmospheric Science Program along with Elizabeth (McCoy) Hatter under Dr. Neil Fox in July 2002.

Upon completion of the Master of Science degree, Steven will continue to reside in Columbia, Missouri with his fiancée Lindsay and dog Dessie Belle while continuing to work under Dr. Fox towards his Doctor of Philosophy degree in Atmospheric Science.